January 2009

The Mechanisms And Roles Of Feedback Loops For Visual Processing

Jing Shao
Washington University in St. Louis

WASHINGTON UNIVERSITY
Department of Physics

Dissertation Examination Committee:
Ralf Wessel, Chair
John W. Clark
Anders E. Carlsson
Zohar Nussinov
Paul S.G. Stein
Bruce Carlson

THE MECHANISMS AND ROLES OF FEEDBACK LOOPS FOR VISUAL PROCESSING

by
Jing Shao

A dissertation presented to the
Graduate School of Arts and Sciences
of Washington University in Saint Louis
in partial fulfillment of the
requirements for the degree of
Doctor of Philosophy

December 2009
Saint Louis, Missouri

ACKNOWLEDGEMENTS

I would like to express my gratitude to all those who made it possible for me to complete this thesis.

I am especially thankful to my supervisor Prof. Ralf Wessel, whose kind guidance and advice provided the ground on which I could pursue my studies and research. His scientific passion, broad interdisciplinary knowledge, and truly encouraging personality have been highly inspiring and enjoyable to me.

I thank Prof. Harald Luksch for the long time collaboration and for his hospitality during a stay at the Technical University in Munich during the summer of 2008.

I am also thankful to my colleagues with whom I had extensive scientific exchange, especially to Dr. Reza Khanbabaie, Dr. Sebastian Brandt, Dr. Adam Eggebrecht, Matthew Caudill, Dihui Lai, and Debajit Saha.

I want to express my appreciation to Rainer Bögle for his patience and encouragement during this time.

Finally, I am deeply indebted to my parents. Without their love and caring support, none of these would have been done.

PREFACE

Some chapters of this thesis have been published, or in preparation for publication, as follows:

Chapter 3 **Shao J**, Lai D, Meyer U, Luksch H, Wessel R (2009) Generating Oscillatory bursts from a network of regular spiking neurons without inhibition. J Comput Neurosci 27:591-606.

Chapter 4 Meyer U, **Shao J**, Chakrabarty S, Brandt SF, Luksch H, Wessel R (2008) Distributed delays stabilize neural feedback systems. Biol Cybern 99: 79-87.

Chapter 5 **Shao J**, Wessel R (2009) The regulatory role of GABAergic Imc neurons in the avian isthmotectal system: transition from excitation to suppression (in preparation).

ABSTRACT OF THE DISSERTATION

Mechanisms and roles of feedback loops for visual processing

By

Jing Shao

Doctor of Philosophy in Physics

Washington University in St. Louis

Professor Ralf Wessel, Chairperson

Signal flow in the brain is not unidirectional; feedback represents a key element in neural signal processing. To address the question on how do neural feedback loops work in terms of synapses, microcircuitry, and systems dynamics, we developed a chick midbrain slice preparation to study and characterize one important feedback loop within the avian visual system: isthmotectal feedbackloop. The isthmotectal feedback loop consists of the optic tectum (OT) and three nucleus isthmi: Imc, Ipc and SLu. The tectal layer 10 neurons project to ipsilateral Imc, Ipc and SLu in a topographic way. In turn Ipc and SLu send back topographical (local) cholinergic terminals to the OT, whereas Imc sends non-topographical (global) GABAergic projections to the OT, and also to the Ipc and the SLu. We first study the cellular properties of Ipc neurons and found that almost all Ipc cells exhibited spontaneous activity characterized with a barrage of EPSPs and occasional spikes. Further experiments reveal the involvement of GABA in mediating the spontaneous synaptic inputs to the Ipc neurons. Next we

investigate the mechanisms of oscillatory bursting in Ipc, which is observed *in vivo*, by building a model network based on the in vitro experimental results. Our simulation results conclude that strong feedforward excitation and spike-rate adaptation can generate oscillatory bursting in Ipc neuron in response to a constant input. Then we consider the effect of distributed synaptic delays measured within the isthmotectal feedback loop and elucidate that distributed delays can stabilize the system and lead to an increased range of parameters for which the system converges to a stable fixed point. Next we explore the functional features of GABAergic projection from Imc to Ipc and find that Imc has a regulatory role on actions of Ipc neurons in that stimulating Imc can evoke action potentials in Ipc neurons while it also can suppress the firing in Ipc neurons which is generated by somatic current injection. The mechanism of regulatory action is further studied by a two-compartment neuron model. Last, we lay out several open questions in this area which may worth further investigation.

TABLE OF CONTENTS

LIST OF FIGURES AND TABLES

Chapter 1

Chapter 2

Chapter 3

Chapter 4

Chapter 5

Chapter 6

Chapter 1

GENERAL INTRODUCTION

Our visual system is extraordinary in the quality and quantity of information it perceives about the world. A glance is sufficient to describe the location, size, shape, color and texture of an object and, if the objects are moving, their direction and speed. The architecture of primate visual system is characterized by a succession of processing stages. This pathway proceeds from the retina via the optic nerve to the optic chiasm; then a subset of the fibers branches off and continues on to the lateral geniculate nucleus (LGN) of the thalamus and then LGN projects to the primary visual cortex (also referred to as striate cortex or V1) (Fig 1.1). After the visual cortex, the information continues on to higher brain centers, such as cortical area V2 and V5. However, the signal flow in the brain is not unidirectional. During a particular processing way, feedforward connections bring input from an earlier station to a higher station along a particular processing pathway. Many of those hierarchical pathways are paralleled by descending feedback connections (Van Essen and Maunsell, 1983; Shepherd, 2003). Feedback connections from higher to lower stations have been demonstrated to contribute to sensory processing and cognition (Bullier et al., 2001; Ro et al., 2003; Suga and Ma, 2003). As to the thalamocortical visual pathway, in addition to the feedforward connections, the thalamus receives a projection back from the same cortical section of to which it projects. Further, the number of projections which are fed back typically drastically outnumbers the amount of feedforward

projections (Felleman and Van Essen, 1991; Salin and Bullier, 1995: Sillito et al., 2003). For example, the number of axon terminals targeted in the thalamus which arise from the cortex greatly outnumbers the number of axon terminals which originated from the retina. Similarly, an area like V1 receives a small contingent of feedforward connections from the LGN and most of its external input from feedback connections (mainly from V2).

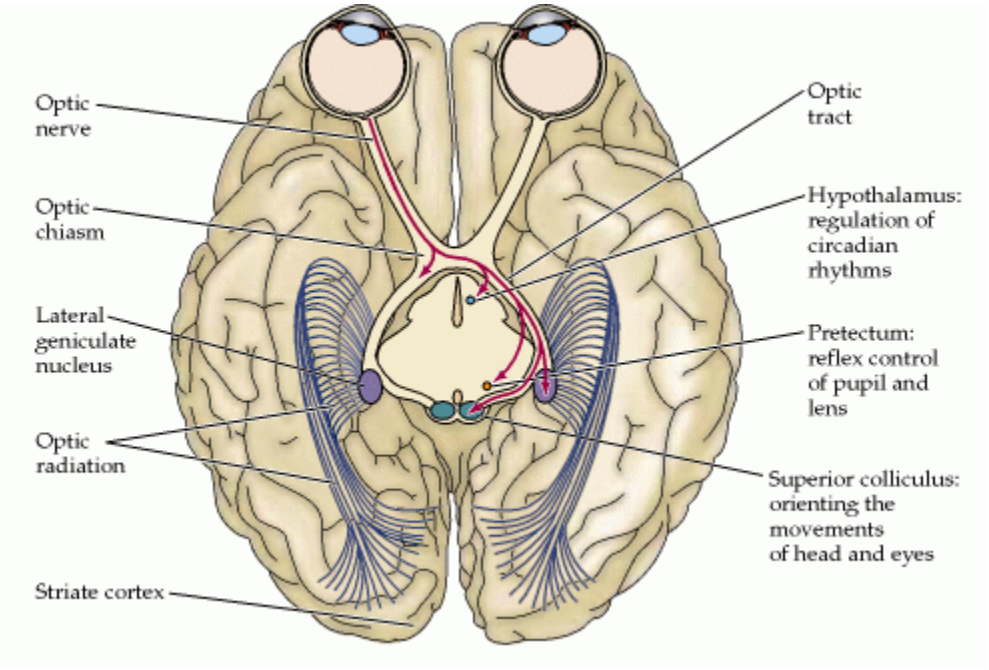

Figure 1.1 Ventral view of the primary visual pathway. This pathway proceeds from the retina via the optic nerve to the optic chiasm; then a subset of the fibers branches off and continues on to the lateral geniculate nucleus (LGN) of the thalamus and then LGN projects to the primary visual cortex. Modified after Purves et al., 2001.

In mammals, another prominent feedback loop is found in the midbrain between the superior colliculus (SC) and the nucleus parabigeminalis (PBN) (Graybriel, 1978). The SC is a multisensory structure which receives input from visual, auditory and somatosensory projections. It is involved in gaze control and spatial attention (Mueller et al., 2005) and is strongly interconnected with the midbrain PBN. The connections between the SC and the PBN are reciprocal and topographic (Sherk, 1979). Recently, it has been suggested that the PBN might help to orchestrate long-range excitation or inhibition across the SC (Lee and Hall, 2006); however, it is still unknown how the PBN functions to modulate neurons in the SC.

In non-mammalian vertebrates, the optic tectum is the homologous to the SC (Mendez-Otero et al., 1980). And the non-mammalian counterpart of the PBN is the isthmic system (Graybriel, 1978; Diamond et al., 1992), which is a complex of midbrain nuclei that is spatially separated from the tectum (Wang et al., 2004, 2006). Reciprocal connections between the optic tectum and the isthmic system have been reported in several species, such as birds (Hunt and Kuenzle, 1976; Hunt et al., 1977; Guentuerkuen and Remy, 1990; Hellmann et al., 2001; Toemboel et al., 2006; Wang et al., 2004, 2006;), reptiles (Wang et al., 1983; George et al., 1999), and frogs (Gruberg and Udin, 1978; Dudkin and Gruberg, 1999). The isthmotectal feedback loop has been implicated to mediate a spatial attentional mechanism (Wang et al., 2000; Gruberg et al., 2006; Maczko et al.,

2006; Marin et al., 2007) and may play a role in multisensory processing (Schroeder and Foxe, 2005; Bulkin and Groh, 2006).

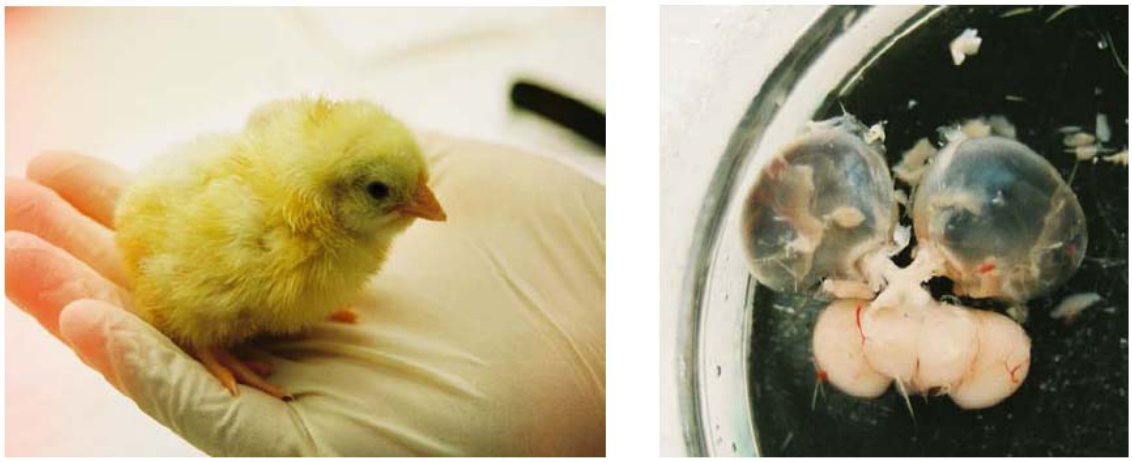

Figure 1.2 One day old chick and its eyes which project to the midbrain. More than 90% of RGC axons are projected to the optic tectum in the midbrain (Binggelli and Paule, 1969).

For a long time, studies of neural signal processing have overwhelmingly emphasized the feedforward connections and largely ignored the feedback connections, and it is only recently that a more balanced view, with feedback connections into account has emerged (Bullier, 2006). Given that feedback connections represent a key element in neural signal processing, it raises the largely unresolved question: How do neural feedback loops “work” in terms of synapses, microcircuitry, and system dynamics? To address this question, rodent brain slice preparations have been developed for the somatosensory (Agmon and Connors, 1991; Cruikshank et al., 2007; MacLean et al., 2005), visual (Li et al., 2003; MacLean et al., 2006), and auditory (Metherate and Cruikshank, 1999;

Cruikshank et al., 2002; Rose and Metherate, 2005; Schiff and Reyes, 2005) thalamocortical pathways. Complementary to these popular mammalian preparations, I chose to study the mechanisms of neural feedback using the isthmotectal loop in the midbrain of chick (Fig. 1.2), where both feedforward and feedback pathways can be maintained in a midbrain slice preparation (Fig. 1.3) (Wang et al., 2004, 2006; Gruberg et al, 2006; Luksch et al., 2005; Meyer et al., 2008; Shao et al., 2009).

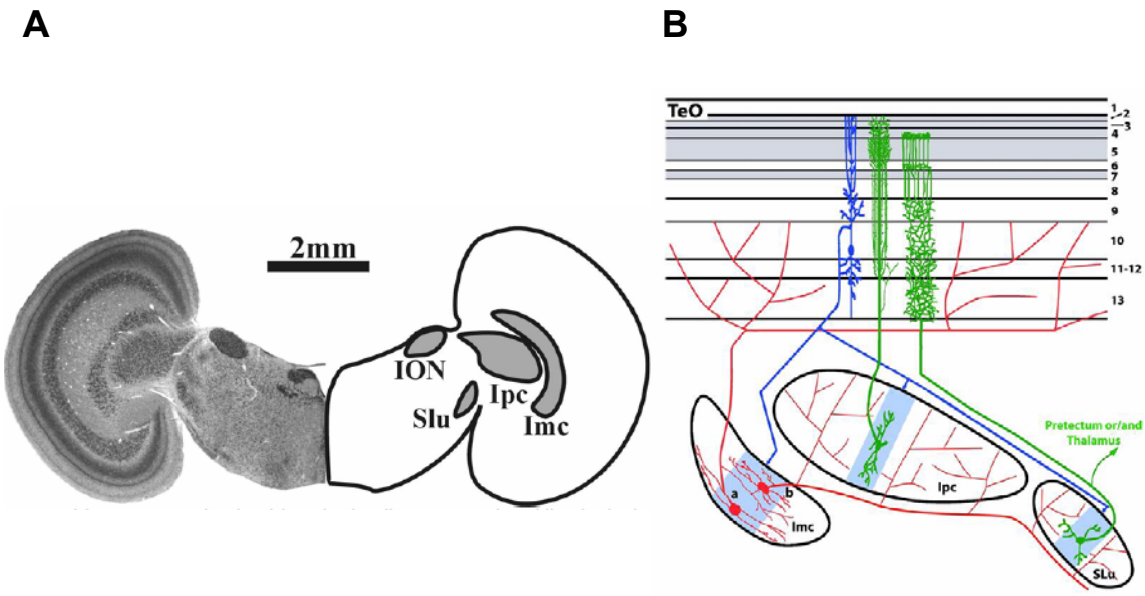

Figure 1.3 The anatomy of the isthmotectal loops. (A) Histological sections through the midbrain of a chick hatchling (left) and corresponding outlines of important isthmic nuclei (right). Abbreviations: n. isthmi pars parvocellularis (Ipc), n.isthmi pars magnocellularis (Imc), n. semilunaris (SLu) and the n. isthmo-opticus (ION). (B) Schematic drawing of the neural circuitry in the isthmotectal pathway. The gray shadings of the tectum represent retinorecipient tectal layers. Modified after Wang et al., 2006.

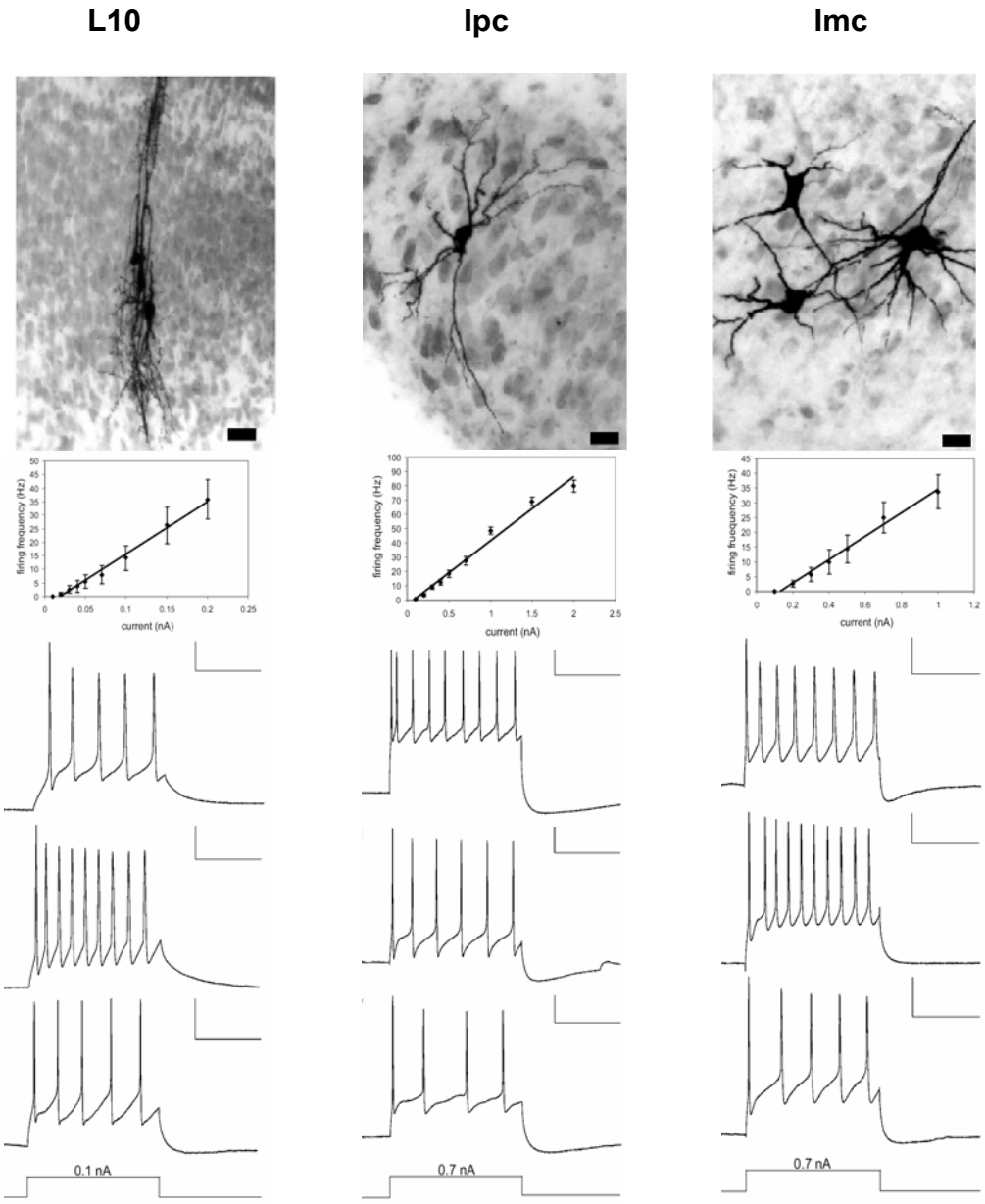

Figure 1.4 Morphological and electrophysiological properties of isthmotectal neurons: L10, lpc, and lmc. Intracellular biocytin fills (scale bar = 20 μm), average frequency vs. current curves from a population of cells, and characteristic spike responses to somatic current injection (scale bars = 20 mV and 100 ms) are shown.

The isthmotectal system in birds is a good system to study the feedback loops thanks to the detailed studies of the anatomy of avian isthmoectal system which provides a detailed background for functional investigations. In birds, the isthmic structure is subdivided into three subnuclei, the nucleus isthmi pars magnocellularis (Imc), the nucleus isthmi pars parvocellularis (Ipc) and the nucleus isthmi pars semilunaris (Slu) (Fig. 1.3). Neurons in the isthmotectal system are accessible in a slice preparation and we can obtain stable whole cell patch recordings from these neurons (Fig. 1.4). Most important, the reciprocal projections between the tectum and the nucleus isthmi have been shown to be preserved in slice preparations (Wang et al., 2004, 2006; Meyer et al., 2008; Shao et al., 2009) and, therefore, the mechanisms of the isthmotectal feedback loop can be studied *in vitro*. In addition, the prominent results of *in vivo* recordings from the avian isthmotectal feedback loop provided us with ample questions to motivate our research (Wang et al., 2000; Marin et al., 2005, 2007; Maczko et al., 2006).

In **Chapter 2** of this dissertation I will first describe the chick midbrain slice preparation and the experiment setups for whole-cell patch recording, pairwise recordings and gramicidin-perforated patch recordings. Then I will talk about one important characteristic property of Ipc neurons: spontaneous activities (Fig. 1.5). Spontaneous excitatory post-synaptic potentials (EPSPs) and occasional spikes have been found in almost all recorded Ipc neurons. Tectum lesion, voltage clamp, pairwise recording and a series of pharmacological experiments have

been done to investigate what are the excitatory inputs of these spontaneous activities. Our experimental results suggest that these spontaneous activities in Ipc are mediated by GABA, which usually acts as an inhibitory neurotransmitter in the central nervous system.

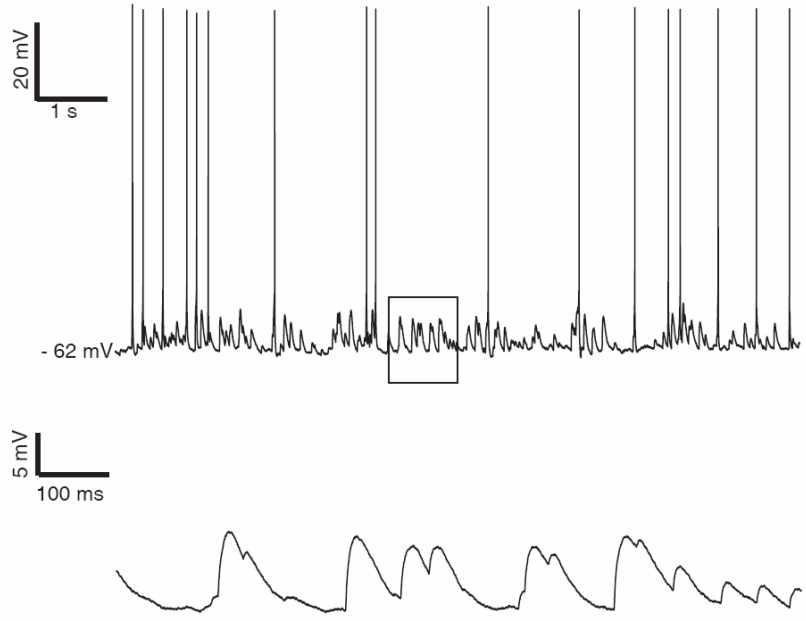

Figure 1.5 Characteristic spontaneous EPSPs and spikes in Ipc neurons, *top trace*, 10 seconds spontaneous activity in an Ipc neuron; bottom trace, focus view of EPSPs in boxed area in top trace.

Our main goal in **Chapter 3** is to investigate how oscillatory bursting is generated in the isthmotectal feedback loop. Ipc neurons, which are reciprocally connected with the tectal L10 neurons, respond with oscillatory bursts to visual stimulation (Marin et al., 2005). In contrast, our *in vitro* experiments show that both, L10 neurons and Ipc neurons, respond with regular spiking to somatic current

injection. To elucidate mechanisms of oscillatory bursting in this network of regularly spiking neurons, we investigated an experimentally constrained model of coupled leaky integrate-and-fire neurons with spike-rate adaptation. The model reproduces the observed Ipc oscillatory bursting in response to simulated visual stimulation. A scan through the model parameter volume reveals that Ipc oscillatory burst generation can be caused by strong and brief feedforward synaptic conductance changes. The mechanism is sensitive to the parameter values of spike-rate adaptation. In conclusion, we show that a network of regular-spiking neurons with feedforward excitation and spike-rate adaptation can generate oscillatory bursting in response to a constant input.

In **Chapter 4**, we further look into the dynamics of isthmotectal feedback loop by investigating the synaptic delays. We consider the effect of distributed delays in neural feedback systems. The avian optic tectum is reciprocally connected with the isthmic nuclei. Extracellular stimulation combined with intracellular recordings reveal a range of signal delays from 3 to 9 ms between isthmotectal elements. This observation together with mathematical analysis concerning the influence of a delay distribution on system dynamics raises the question whether a broad delay distribution can impact the dynamics of neural feedback loops. For a system of reciprocally connected model neurons we found that distributed delays enhance system stability in the following sense. With increased distribution of delays, the system converges faster to a fixed point and converges slower toward a limit cycle. Further, the introduction of distributed delays leads to an

increased range of the average delay value for which the system's equilibrium point is stable. The system dynamics are determined almost exclusively by the mean and the variance of the delay distribution and show only little dependence on the particular shape of the distribution.

Chapter 5 is to explore the properties of GABAergic inputs from Imc to Ipc. Typically GABA-mediated synaptic inputs hyperpolarize the membrane potential of post-synaptic cells away from spike threshold, thus reduce the excitability of targeted neurons. However, we found that the GABAergic inputs from Imc to Ipc acted differently: the reversal potential of this GABA mediated synaptic current is around -40 mV, i.e. stimulating Imc can evoke EPSPs or action potentials in Ipc neurons; but this excitation can switch to spike suppression when simultaneously applying current injections into post-synaptic Ipc neurons. We investigated the effects of GABA and intracellular [Cl^-] by whole cell patch recording and gramicidin perforated recording. The results suggested that suppression of spikes appears to be mediated by a large increase in conductance during GABA exposure.

In **chapter 6** I will discuss the open questions and future projects which can be investigated further in this area. I will put out the preliminary data for some of them.

Reference

Agmon A, Connors BW (1991) Thalamocortical responses of mouse somatosensory (barrel) cortex in vitro. Neuroscience 41: 365-379.

Binggelli RL, Paule WJ (1969) The pigeon retina: quantitative aspects of the optic nerve and ganglion cell layer. J Comp Neurol 137:1-18.

Bulkin DA, Groh JM (2006) Seeing sounds: visual and auditory interactions in the brain. Curr Opin Neurobiol 16: 415-419.

Bullier J, Hupe JM, James A, Girard P (2001) The role of feedback connections in shaping the response of visual cortical neurons. Progr Brain Res 134: 193-204.

Bullier J (2006) What is fed back? In: *2*3 Problems in Systems Neuroscience. Ed: Van Hemmen JL, Sejnowski TJ. Oxford University Press. pp.103-132.

Cruikshank SJ, Rose HJ, Metherate R (2002) Auditory thalamocortical synaptic transmission in vitro. J Neurophysiol 87: 361-384.

Diamond IT, Fitzpatrick D, Conley M (1992) A projection from the parabigeminal nucleus to the pulvinar nucleus in Galago. J Comp Neurol 316: 375-382.

Felleman DJ, VanEssen DC (1991) Distributed hierarchical processing in the primate cerebral cortex. Cereb Cortex 1: 738-742.

Graybriel AM (1978) A satellite system of the superior colliculus: the parabigeminal nucleus and its projections to the superficial collicular layers. Brain Res 145: 365-374.

Gruberg ER, Udin SB (1978) Topographic projections between the nucleus isthmi and the tectum of the frog *Rana pipiens*. J Comp Neurol 179: 487-500.

Dudkin EA, Gruberg ER (1999) Relative number of cells projecting from contralateral and ipsilateral nucleus isthmi to loci in the optic tectumis dependent on visuotopic location: horseradish peroxidase study in the leopard frog. J Comp Neurol 414: 212-216.

Goddard CA, Knudsen EI, Huguenard JR (2007) Intrinsic excitability of cholinergic neurons in the rat parabigeminal nucleus. J Neurophysiol 98: 3486-3493.

Gruberg ER, Dudkin EA, Wang Y, Marin G, Salas C, Sentis E, Letelier JC, Mpodozis J, Malpeli J, Cui H, Ma R, Northmore D, Udin S (2006) Influencing and interpreting visual input: The role of a visual feedback system. J Neurosci 26: 10368-10371.

Guentuerkuen O, Remy M (1990) The topographocal projection of the nucleus isthmi pars parvocellularis (Ipc) onto the tectum opticum in the pigeon. Neurosci Lett 111: 18-22.

Hellmann B, Manns M, Guentuerkuen O (2001) Nucleus isthmi, pars semilunaris as a key component of the tectofugal visual system in pigeons. J Comp Neurol 436: 153-166.

Hunt SP, Künzle H (1976) Observations on the projections and intrinsic organization of the pigeon optic tectum: an autoradiographic study based on anterograde and retrograde, axonal and dendritic flow. J Comp Neurol 170: 153-172.

Hunt SP, Streit P, Künzle H, Cuenod M (1977) Characterization of the pigeon isthmotectal pathway by selective uptake and retrograde movement of

radioactive compounds and by Golgi-like horseradish peroxidase labeling. Brain Res 129: 197-212.

Lee P, Hall WC (2006) An in vitro study of horizontal connections in the intermediate layer of the superior colliculus. J Neurosci 26: 4763-4768.

Li J, Guido W, Bickford ME (2003) Two distinct types of corticothalamic EPSPs and their contribution to short-term synaptic plasticity. J Neurophysiol 90: 3429-3440.

Luksch H, Scholz S, Wessel R (2005) Anatomy and electrophysiology of tecto-isthmal feedback loops in the chicken. German Neuroscience Society, poster 195A.

MacLean JN, Watson BO, Aaron GB, Yuste R (2005) Internal dynamics determine the cortical response to thalamic stimulation. Neuron 48: 811-823.

MacLean JN, Fenstermaker V, Watson BO, Yuste R (2006) A visual thalamocortical slice. Nat Methods 3: 129-34.

Maczko KA, Knudsen PF, Knudsen EI (2006). Auditory and visual space mapsin the cholinergic nucleus isthmi pars parvocelluaris of the barn owl. J Neurosci 49: 12799-127806.

Marin G, Salas C, Sentic E, Rojas X, Letelier JC, Mpodozis J (2007) A cholinergic gating mechanism controlled by competitive interactions in the optic tectum of the pigeon. J of Neurosci 27: 8112-8121.

Mendez-Otero R, Rocha-Miranda CE, Perry VH (1980) The organization of the parabigemino-tectal projections in the opossum. Brain Res 198:183-189.

Metherate R, Cruikshank SJ (1999) Thalamocortical inputs trigger a propagating envelope of gamma-band activity in auditory cortex in vitro. Exp Brain Res 126: 160-174.

Meyer U, Shao J, Chakrabarty S, Brandt SF, Luksch H, Wessel R (2008) Distributed delays stabilize neural feedback systems. Biol Cybern 99: 79-87.

Mueller JR, Philiastides MG, Newsome WT (2005) Microstimulation of the superior colliculus focuses attention without moving the eyes. Proc Natl Acad Sci 102: 524-529.

Purves D, Augustine GJ, Fitzpatrick D, Katz LC, LaMantia AS, McNamara JO, Williams SM (2001) Neuroscience (second edition). Sinauer Associates, Inc. pp 253-253.

Ro T, Breitmeyer B, Burton P, Singhal NS, Lane, D (2003) Feedback contributions to visual awareness in human occipital cortex. Curr Biol 13: 1038-1041.

Rose HJ, Metherate R (2005) Auditory thalamocortical transmission is reliable and temporally precise. J Neurophysiol 94: 2019-2030.

Salin PA, Bullier J (1995) Corticocortical connections in the visual system: Structure and function. Physiol Reviews 75: 107-154.

Schiff ML, Reyes AD (2005) Synaptic and membrane properties of thalamocortical recipient neurons in AI. SfN abstract 615.10.

Schroeder CE, Foxe JJ (2005) Multisensory contributions to low-level, unisensory processing. Curr Opin in Neurobiol 15: 454-458.

Shao J, Lai D, Meyer U, Luksch H, Wessel R (2009) Generating oscillatory bursts from a network of regular spiking neurons without inhibition. J Comput Neurosci 27:591-606.

Shepherd GM (2003) The synaptic organization of the brain. Oxford Univ Press, New York.Suga N, Ma X. Multiparametric cortifugal modulation and plasticity in the auditory system. Nat Rev Neurosci 4: 783-794.

Sherk H (1979) A comparison of visual-response properties in cat's parabigeminal nucleus and superior colliculus. J Neurophysiol 42: 1640-1655.

Sillito AM, Cudiero J, Jones HE (2006) Always returning: feedback and sensory processing in visual cortex and thalamus. Trends Neurosci 29: 307-316.

Van Essen DC, Maunsell JHR (1983) Hierarchical organization and functional streams in the visual cortex. Trends Neurosci 6: 370-375.

Wang Y, Xiao J and Wang SR (2000) Excitatory and inhibitory receptive fields of tectal cells are differentially modified by magnocellular and parvocellular divisions of the pigeon nucleus isthmi. J Comp Physiol A 186: 505-511.

Wang Y, Major DE, Karten HJ (2004) Morphology and connections of nucleus isthmi pars magnocellularis in chicks (*Gallus gallus*). J Comp Neurol 469: 275-297.

Wang Y, Luksch H, Brecha NC, Karten HJ (2006) Columnar projections from the cholinergic nucleus isthmi to the optic tectum in chicks (*Gallus gallus*): A possible substrate for synchronizing tectal channels. J Comp Neurol 494:7-35.

Chapter 2

GABA-MEDIATED SPONTANEOUS ACTIVITY IN THE CHOLINERGIC IPC NEURONS

2.1 Abstract

The nucleus isthmi pars parvocellularis (Ipc) is one of the isthmic structures in birds. It receives glutamatergic inputs from the optic tectum (OT), and projects through its paintbrush-like cholinergic endings back upon the tectum. Both projections preserve a high degree of topography, such that corresponding points of the visual field representation in these two structures are reciprocally connected. In addition, Ipc also receives non-topographic GABAergic input from the nucleus isthmi pars magnocellularis (Imc).

We conducted whole-cell recordings from Ipc cells in the midbrain slices of chickens (aged from P1 to P10). Almost all recorded Ipc cells have spontaneous activity: occasional spikes with a barrage of EPSPs. Tectum lesion, voltage clamp, gramicidin perforated patch recording, pairwise recording and a series of pharmacological experiments have been done to investigate what are the excitatory inputs of these spontaneous activities. Our experimental results suggest that these spontaneous EPSPs in Ipc are mostly mediated by GABA, which is usually the main inhibitory neurotransmitter in the central nervous system but here acts as an excitatory transmitter.

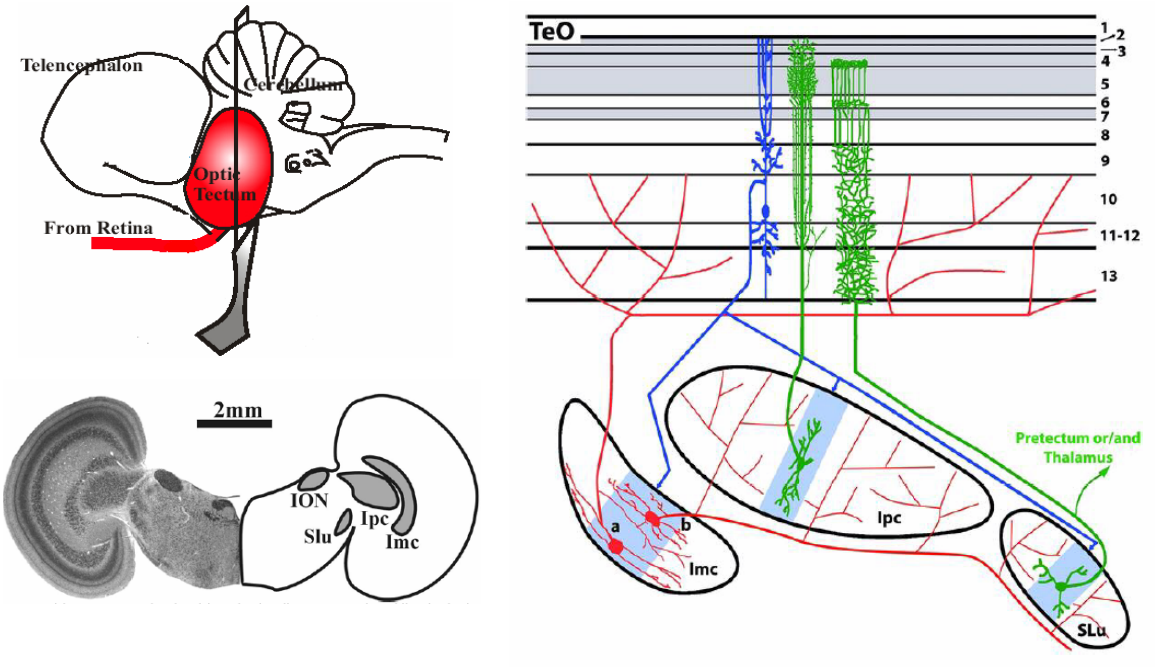

Figure 2.1 Location and connectivity of the isthmotectal feedback loop. *Left upper*, lateral view of avian brain and position of isthmotectal feedback loop. *Left down*, histological sections through the midbrain and corresponding outlines; *Right*, schematic drawing of neural circuitry in the isthmotectal pathway. Modified after Wang et al., 2006.

2.2 Introduction

In birds, the nucleus isthmi pars parvocellularis (Ipc) is a cholinergic midbrain nucleus that is interconnected with the optic tectum (OT) (Fig 2.1). Many studies have shown that the OT, which receives visual inputs via retinal ganglion cell (RGC) axons, plays a key role in visual information processing (Hodos and Karten, 1974; Bravo and Pettigrew, 1981; Chaves and Hodos, 1998; Laverghetta and Shimizu, 1999; Luksch et al., 2004; Khanbabaie et al., 2007). The connections between OT and Ipc are reciprocal and topographic in a way that Ipc

projects back to the same areas in OT where it receives input from (Wang et al., 2004, 2006). Because of the regulatory role of acetylcholine (ACh) in the neural network (Metherate et al. 1988; Ashe et al. 1989; McKenna et al. 1989; Hasselmo and McGaughy, 2004), it is suggested that the cholinergic Ipc functions to modulate the neuronal activities in OT (Wang et al., 2003; Marin et al., 2005; Maczko et al., 2006). In addition, Ipc and OT both receive non-topographic inputs from a GABAergic nucleus, the nucleus isthmi pars magnocellularis (Imc) (Fig. 2.1).

An analogous neural feedback circuitry is found in the midbrain of mammals, between the cholinergic parabigeminal nucleus (PBN) and the superior colliculus (SC) (Sherk 1979; Tokunaga and Otani 1978; Mufson et al., 1986). The properties of PBN have been studied in different species (Sherk 1979; Cui and Malpeli, 2003; Lee and Hall 2006; Goddard et al., 2007). One major characterization of PBN is that these neurons show a high rate of spontaneous activity, both *in vivo* recordings and recordings from brain slice preparations.

To study the electrophysiological properties of cholinergic Ipc neurons, we performed the whole-cell patch and gramicidin-perforated patch recordings in a slice preparation of chicken midbrains. In this study, we report that almost all Ipc neurons exhibit spontaneous activity which is characterized by a barrage of excitatory post-synaptic potentials (EPSPs) with occasional spikes. However, unlike PBN neuron's spontaneous spiking caused by intrinsic excitability

(Goddard et al., 2007), spontaneous activities in Ipc neurons are triggered by synaptic inputs. The complete blockage of spontaneous EPSPs and action potentials by bicuculline suggests this synaptic current is mediated by GABA.

2.3 Methods

2.3.1 The avian midbrain slice preparation

Fifty eight White Leghorn chick hatchlings (Gallus gallus) aged less than 3 days (unless otherwise noted, i.e. P8-P10) were used in this study. All procedures used in this study were approved by the local authorities and conform to the guidelines of the National Institutes of Health on the Care and Use of Laboratory Animals. Animals were injected with ketamine (40 mg per kg, Fort Dodge Animal Health, Fort Dodge, Iowa). Brain slices of the optic tectum were prepared following published protocols (Dye and Karten, 1996; Luksch et al., 1998; Luksch et al, 2004). Briefly, preparations were done in 0 ºC, oxygenated, and sucrose-substituted saline (240 mM sucrose, 3 mM KCl, 5 mM MgCl2, 0.5 mM CaCl2, 1.2 mM NaH2PO4, 23 mM NaHCO3, and 11 mM D-glucose). After decapitation, the brains were removed from the skull, and the forebrain, cerebellum, and medulla oblongata were discarded. A midsagittal cut was used to separate the two hemispheres. The two hemispheres were sectioned at 360-400 μm on a tissue slicer (VF-200 Microtome, Precisionary Instrument Inc.) in the transverse plane. Slices were collected in oxygenated ACSF (120 mM NaCl, 3 mM KCl, 1 mM MgCl2, 2 mM CaCl2, 1.2 mM NaH2PO4, 23 mM NaHCO3, and 11 mM D-glucose) and kept submerged in a chamber that is bubbled continuously with

carbogen (95% oxygen, 5% CO2) at room temperature. Slices were allowed to recover for 1 hour before recording. The slice was then transferred to a recording chamber (RC-26G, Warner Instruments, Hamden, CT) mounted on a fixed stage upright microscope equipped with DIC optics (BX-51WI, Olympus, Japan). The slice was held gently to the bottom of the chamber with a stainless steel anchor with Lycra threads, and the chamber was perfused continuously with oxygenated saline at room temperature. The lpc cells were visible with DIC optics.

2.3.2 Whole-cell patch recording and pairwise recording

Whole-cell patch recordings were obtained with glass micropipettes pulled from borosilicate glass (1.5 mm outer diameter; 0.86 mm inner diameter; AM Systems, Carlsborg, WA) on a horizontal puller (Sutter Instruments, San Rafael, CA) and filled with a solution containing 100 mM K-gluconate, 40 mM KCl, 10 mM HEPES, 0.1 mM $CaCl_2$, 2 mM $MgCl_2$, 1.1 mM EGTA, and 2 mM Mg-ATP; pH was adjusted to 7.2 with KOH. Patch pipettes were drawn to 1–2 μm tip diameter and had resistances between 3 and 8 MΩ (DC). Electrodes were advanced through the tissue with a motorized micromanipulator (MP-285, Sutter Instruments, San Rafael, CA) while constant positive pressure was applied. After the electrode had attached to a membrane and formed a seal, access to the cytosol was achieved by brief suction. Whole-cell patch recordings (current clamp) were performed with the amplifier (Axoclamp 2B, Axon Instruments, Foster City, CA) in the bridge mode. The series resistance was compensated with the bridge balance. Recordings with voltage clamp were performed with the same amplifier in the

SEVC (Single Electrode Voltage Clamp) mode. The sample rate was set optimized by monitoring the output on an oscilloscope.

The liquid junction potential (measured in ACSF and calculated by pClamp, Molecular Devices, Sunnyvale, CA) was 11 mV. However, all data shown in this chapter has NOT been corrected for the liquid junction potential.

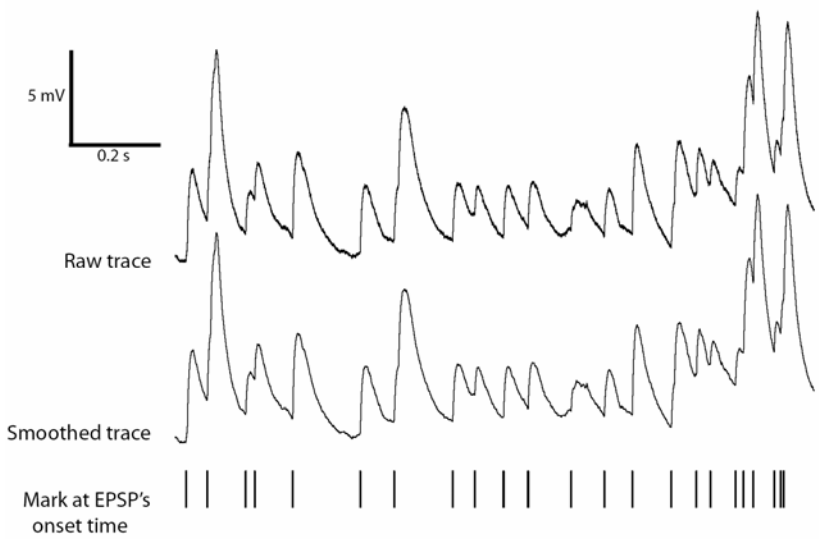

Figure 2.2 Spontaneous EPSPs analysis. Sample recording from an lpc neuron (raw trace) and after smoothing with a Gaussian kernel (smoothed trace). Events with a first derivative larger than 4 mV/ms (and less than 200 mV/ms; if larger than 200 mV/ms, a spike will be marked) are identified as EPSPs (mark at EPSP's onset time). The search strategy has a high success rate, but can miss the second EPSP in closely spaced pairs, for instance the large EPSP after #7 was missed.

Pairwise recordings were conducted with two electrodes that were the same as used in the single cell patch recordings. Procedures were similar as stated above. Two electrodes were advanced through the tissue and approached the target neurons simultaneously. Successful whole cell patch recording was obtained on one cell first, and then, with minimum interruption to the first neuron, the second whole-cell patch recording was achieved.

2.3.3 Gramicidin-perforated patch recording

The antibiotic gramicidin, when incorporated into lipid membranes, forms pores that are exclusively permeable to monovalent cations (i.e. Na^+ and K^+) and small molecules. Gramicidin-perforated patch recording has been shown to avoid artifactual changes in intracellular chloride concentration, thus one can more accurately examine the reversal potential of chloride synaptic currents. (Kyrozis and Reichling, 1995; Monsivais and Rubel, 2001)

Electrodes for gramicidin-perforated patch recordings were similarly pulled as those of whole-cell patch recordings. After filling the pipette tip with a solution containing 150 mM KCl and 10 mM Hepes, the pipette shank was backfilled by a syringe with the same solution additionally containing gramicidin dissolved DMSO at a final concentration of 40 μg/ml. For perforated-patch recording, after giga-ohm seal formation there was no brief suction to rupture the cell membrane. The series resistance measurements then decreased to <100 MΩ within 45 mins, at which time data acquisition began. Recordings were aborted if the perforated

patch ruptured, which was easily detected because of the high concentration of Cl^- in the gramicidin-perforated patch electrode (E_{cl} = 0 mV for this electrode).

2.3.4 Data acquisition and analysis

Analog data were stored, and analyzed on a personal computer equipped with a data acquisition card (PCI-MI0-16E-4) and LabView software (both National Instruments, Austin, TX). Data were analyzed by customized Matlab program (The MathWorks Inc, Natick, MA). Original traces were first smoothed by a Gaussian function (Fig. 2.2). The criterion for identifying an EPSP was the slope value of its rising phase (between 4 mV/ms and 200 mV/ms). A rising phase with a slope greater than 200 mV/ms was identified as a spike. And afterhyperpolarizations (AHP) of spikes were excluded from EPSP counting. Both start time and peak time of each EPSP were recorded for inter-EPSP-interval and amplitude analysis. The calculated values of inter-EPSP-intervals were distributed into 100 bins, thus the bin size was decided by the maximum value of inter-EPSP-interval. The fitting curves to the histogram of inter-EPSP-intervals, $f(\Delta t) = \lambda e^{-\Delta t/\tau}$, were obtained by least-square fitting method; fit the natural logarithm of f value to a linear function of Δt value. The first bin and last few bins of histogram were neglected for the fitting. All data presented as the mean ± SD.

2.3.5 Pharmacological experiments

All reagents were mixed with ACSF and then bath applied to the slices. Unless otherwise noted, all reagents were obtained from Sigma (St. Louis, MO). *CNQX*,

AMPA/Kainate (non-NMDA) glutamate receptor antagonist; *CPP*, NMDA glutamate receptor antagonist; *TTX*, Tetrodotoxin, blocker of Na^+ channels; *Bicuculline*, $GABA_A$ receptor antagonist.

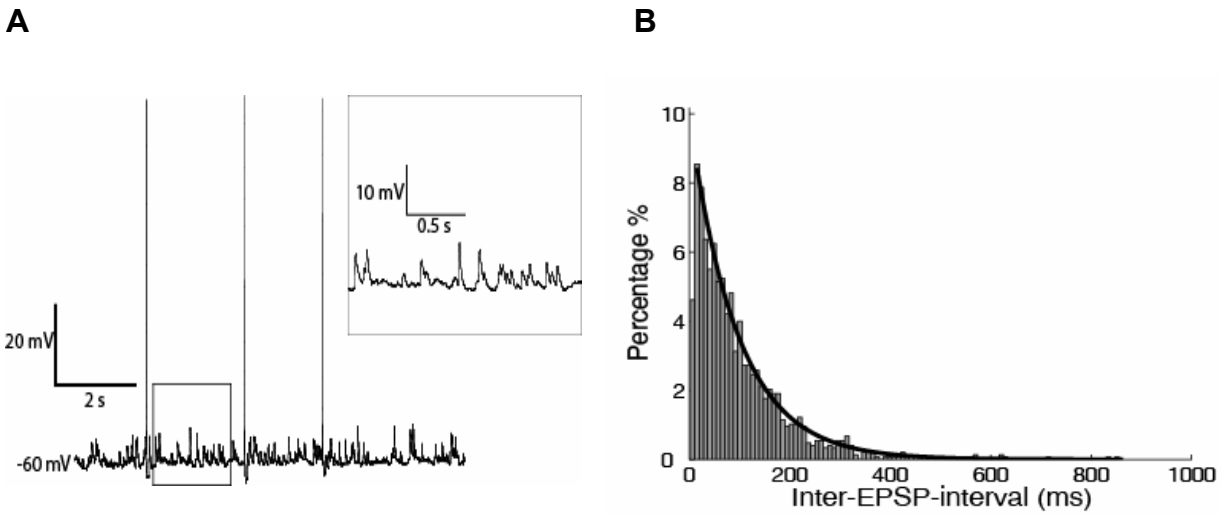

Figure 2.3 Spontaneous activity of Ipc neurons. (A) Spontaneous EPSPs and spikes, *inset,* focus view of EPSPs. (B) Histogram of distribution of inter-EPSP-intervals, N = 1473. The black solid line is fitted exponential curve, $f(\Delta t) = \lambda e^{-\Delta t/\tau}$, λ = 140.3, τ = 96.2 ms, Δt units in ms, which was obtained by least-square fitting method (R^2 = 0.94).

2.4 Results

We obtained stable whole-cell patch recordings from a total of 195 Ipc neurons. These cells had a membrane potential of -57 ± 6 mV. Among all tested cells, 188 Ipc cells (96.4% of total) exhibited spontaneous activity: a barrage of EPSPs with occasional spikes (Fig. 2.3A). Average firing rates were less than 1 Hz. EPSPs occurred at a frequency of 9.1 ± 2.5 Hz. According to the distribution of inter-

EPSP-intervals (Fig. 2.3B), which had an exponential decay shape and a coefficient of variation close to 1 (CV = 0.96, N = 1473), the generation of these spontaneous EPSPs is consistent with a Poisson process.

High [K^+] boosts the spontaneous activity of the lpc cells

To increase the excitability of the potential presynaptic neurons which send spontaneous inputs into the lpc, we bath applied a higher concentration of potassium (6-10 mM) to the slice. lpc neurons (n = 10) showed an increased membrane potential (between -50 mV to -38mV) with more EPSPs and more spikes (Fig. 2.4A, B). The frequency of EPSPs increased from 9.7 ± 2.6 Hz to 19.4 ± 6.9 Hz. The distribution of inter-EPSP-interval was still exponential shaped implying a possible Poisson process (Fig. 2.4 C, N=2140, CV = 1.06).

Spontaneous activity persists when the optic tectum is removed from the slice

To examine whether the synaptic inputs of the spontaneous activity originate in the optic tectum, we microsurgically removed the optic tectum from the slice (Fig. 2.5A, inset). We recorded from three slices in which we had removed the optic tectum. All tested lpc cells (n = 6) still exhibited spontaneous activities with both EPSPs and spikes (Fig. 2.5B). EPSPs continued to occur at a frequency of 10.5 ± 2.2 Hz, and the distribution of inter-EPSP-intervals still had an exponential shape and a CV of 1.25.

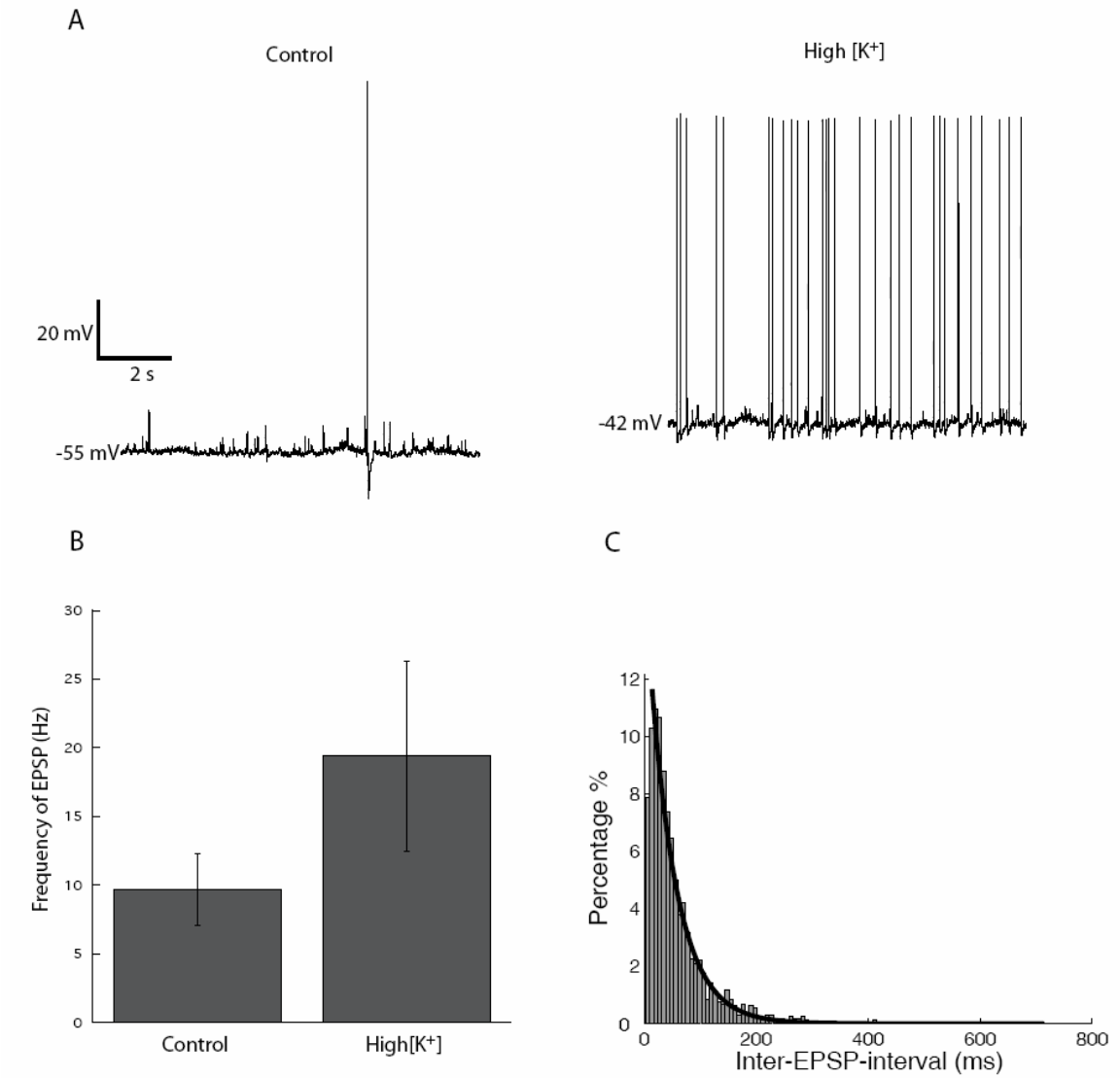

Figure 2.4 Effect of ACSF with high [K^+] to the spontaneous activity of lpc cells. (A) Spontaneous activity of an lpc neuron before (left) and after (right) the application of ACSF with high [K^+] (9 mM). (B) The frequency of EPSPs was greatly increased by high [K^+]. (C) Histogram of distribution of inter-EPSP-intervals in high [K^+] condition (N = 2140). The black solid line is fitted exponential curve, $f(\Delta t) = \lambda e^{-\Delta t/\tau}$, $\lambda = 335.7$, $\tau = 47.8$ ms, Δt units in ms, which was obtained by least-square fitting method ($R^2 = 0.92$).

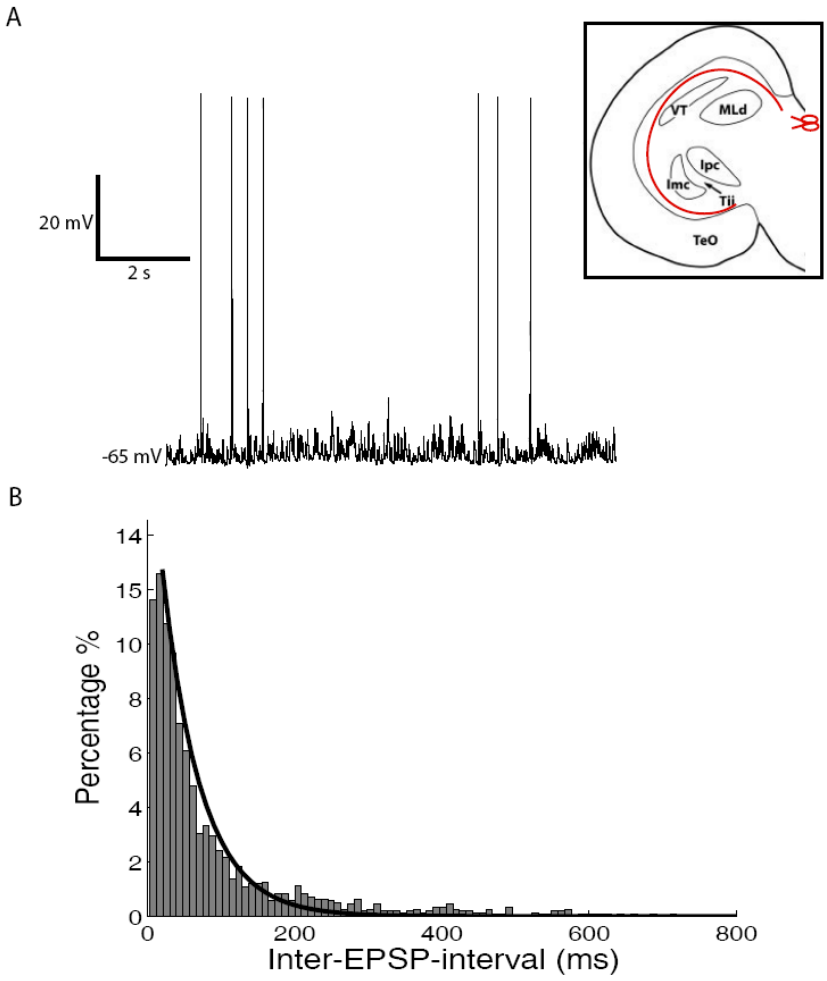

Figure 2.5 (A) Spontaneous activity of Ipc cell in the slice without optic tectum; *inset,* the optic tectum was surgically removed, along the red line (schematic drawing is from Wang et al, 2006, Fig. 6). (B) Histogram of distribution of inter-EPSP-intervals. N = 1582, CV = 1.25. The black solid line is fitted by an exponential curve, $f(\Delta t) = \lambda e^{-\Delta t/\tau}$, which was obtained by least-square fitting method ($R^2 = 0.87$); $\lambda = 395.7$, $\tau = 52.4$ ms, Δt units in ms.

Pharmacological experiments

To determine what synaptic transmitters are involved in the generation of spontaneous EPSPs in Ipc cells, we conducted several pharmacological experiments.

Bath application of 1 μM TTX, a sodium channel blocker, abolished all spontaneous spikes in the recorded cells (n = 6), but still left a few small amplitude EPSPs (Fig. 2.6A, left, right). The average amplitude of EPSPs changed from 2.2 ± 0.3 mV to 1.3 ± 0.2 mV and average frequency changed from 6.9 ± 2.0 Hz to 2.2 ± 0.6 Hz (Fig. 2.6A, center).

In all cells tested in the presence of 20 μM non-NMDA glutamatergic receptor antagonist CNQX (n = 8), spontaneous activity typical of Ipc neurons persisted (Fig. 2.6B, left). However, average frequency of EPSPs was decreased by the CNQX application, from 8.6 ± 3.3 Hz to 3.3 ± 0.7 Hz (Fig. 2.6B, center). Average amplitude slightly decreased from 2.5 ± 0.5 mV to 2.2 ± 0.5 mV. Application of CNQX also affected the distribution of EPSP amplitudes leading to a larger portion of small amplitude EPSPs (< 4 mV) and a smaller portion of large amplitude EPSPs (> 4 mV) (Fig. 2.6 B, right).

Application of 30 μM CPP, a NMDA glutamatergic receptor antagonist, also led to a decrease in amplitude and frequency of the spontaneous EPSPs. Average

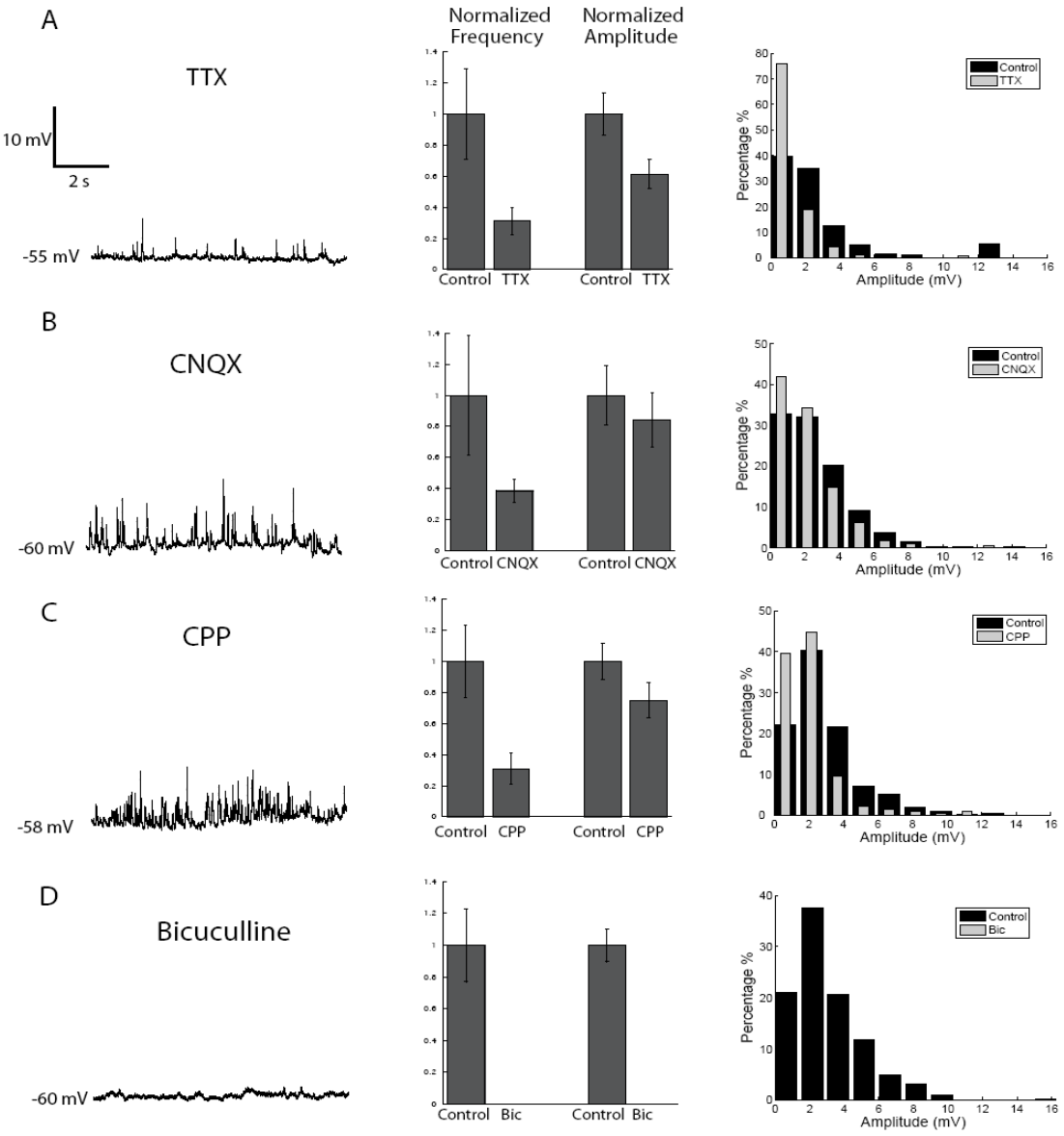

Figure 2.6 Effect of TTX, CNQX, CPP and bicuculline on spontaneous EPSPs. *Left column*, spontaneous EPSPs in lpc cells with (A) 1 μM TTX, (B) 20 μM CNQX, (C) 30 μM CPP and (D) 100 μM bicuculline. *Center column*, change of normalized average frequency and amplitude of EPSPs before and after the drug application. Values in control condition were scaled to 1. *Right column*, comparisons of distributions of EPSPs amplitude. Bin size was 1.5 mV.

amplitude of EPSPs in tested neurons (n = 4) changed from 3.0 ± 0.3 mV to 2.2 ± 0.3 mV and average EPSP frequency changed from 6.4 ± 1.5 Hz to 2.0 ± 0.6 Hz (Fig. 2.6C, center). Furthermore, the distribution of EPSP amplitudes changed in a similar way to the CNQX condition (Fig. 2.6 C, right).

Results were different when 100 μM bicuculline was applied. Spontaneous activity was completely eliminated by bicuculline in lpc neurons (n = 10), no EPSPs or spikes (Fig. 2.6D). Also 30 μM bicuculline was able to block all spontaneous EPSPs that could not be blocked by the application of 25 μM CNQX and 50 μM CPP (data not shown).

GABA depolarized the lpc cells

Based on the pharmacological experiments described above, only the GABA receptor blocker bicuculline was effective in blocking all EPSPs in lpc cells. To investigate the role of GABA transmitters, 0.1 mM GABA was bath applied to the slices. The membrane potentials of lpc neurons (n = 8) quickly depolarized by 10-25 mV (Fig. 2.7A, center); the tested neurons had no spontaneous EPSPs at that depolarized membrane potential (Fig. 2.7A, center) and did not respond to the 0.1 nA current injection (Fig. 2.7B, central); the cells' input resistance was dramatically decreased by the application of GABA (Fig. 2.7C, center). When the GABA was washed out by normal ACSF, spontaneous EPSPs were recorded again (Fig. 2.7A, right), the cell responded to the current injection (Fig. 2.7B,

right), and the input resistance increased back to its value in the control condition (Fig. 2.7C, right).

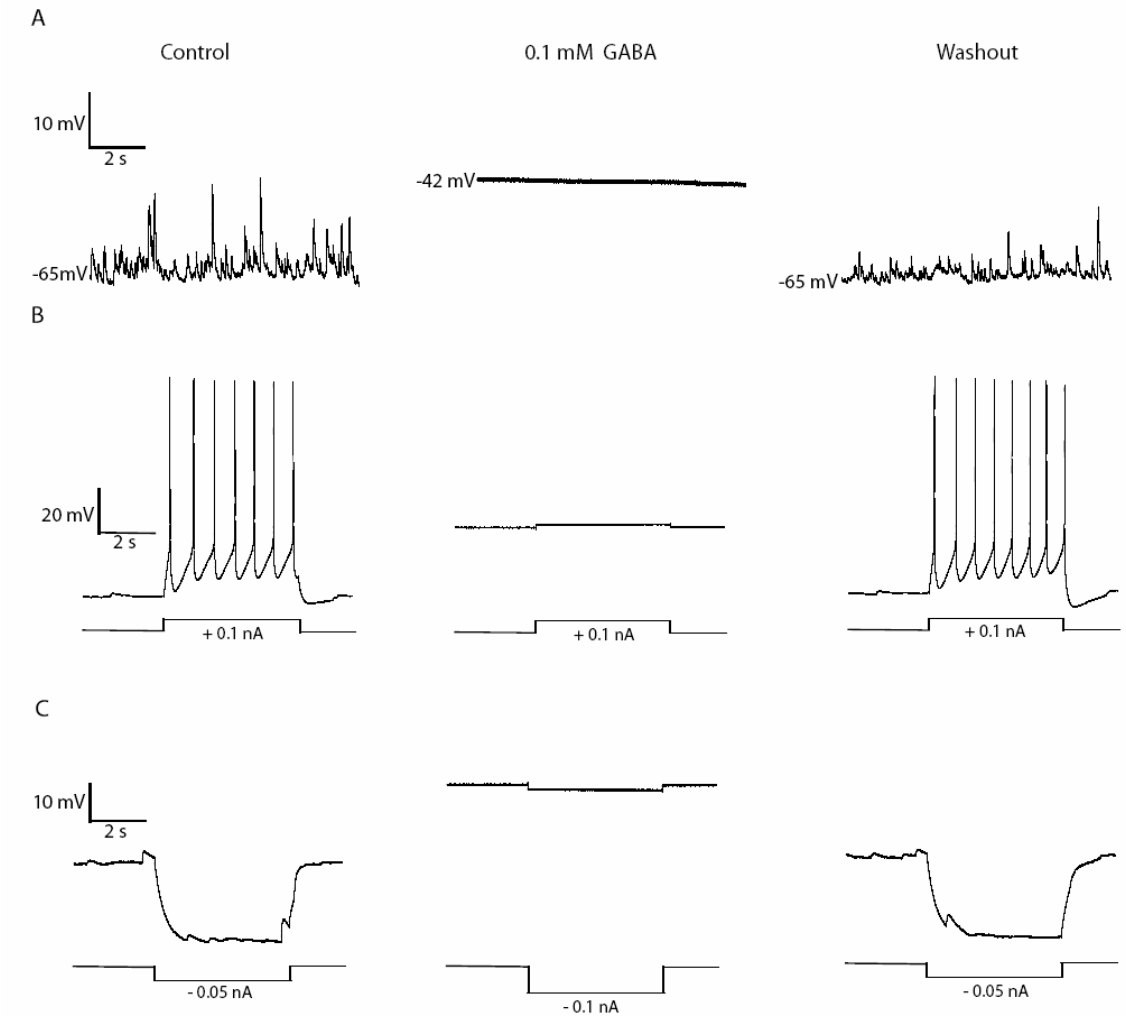

Figure 2.7 Effects of GABA on spontaneous activity of lpc cells. In (A) ,(B) and (C), *left column*, control condition; *middle column*, bath application of 0.1 mM GABA; *right column,* washout the GABA with normal saline. (A) Spontaneous EPSPs. (B) Responses to 0.1 nA current injection. (C) Responses to a small amount of hyperpolarizing current, 0.05 nA for control and washout condition, 0.1 nA for GABA applied condition.

Voltage Clamp

In addition to the pharmacological experiments, recording spontaneous synaptic currents in the voltage clamp mode also provided a clue about what transmitters are involved in generating the EPSPs in Ipc neurons. We recorded a total of 8 Ipc neurons under the voltage clamp. Spontaneous synaptic inputs of Ipc cells showed up as excitatory post-synaptic currents (EPSCs) in the voltage clamp mode (Fig. 2.8 A). Then the cells were clamped at different holding potentials, from -76 mV up to 0 mV. To obtain a reasonable estimation for the amplitude of the synaptic currents, in each recording of 10 seconds duration we picked the EPSC which had the largest amplitude, and averaged their amplitudes over 5 recordings for a certain holding potential. We plotted these averaged amplitudes as the averaged synaptic currents, against the different holding potential values. As shown in Figure 2.8B, averaged synaptic currents reversed sign at approximately - 40 mV. In other words, the reversal potential of spontaneous synaptic currents is around - 40 mV.

Gramicidin-perforated patch recordings

The reversal potential for GABAergic synaptic currents is mainly determined by the chloride concentration across the neuron membrane. To examine Ipc neurons spontaneous activity without bringing artifactual changes to the intracellular chloride concentration, we conducted gramicidin-perforated patch recordings from Ipc neurons (n=5). The results showed that spontaneous EPSPs and spikes were also found in Ipc neurons with perforated-patch recordings (Fig.

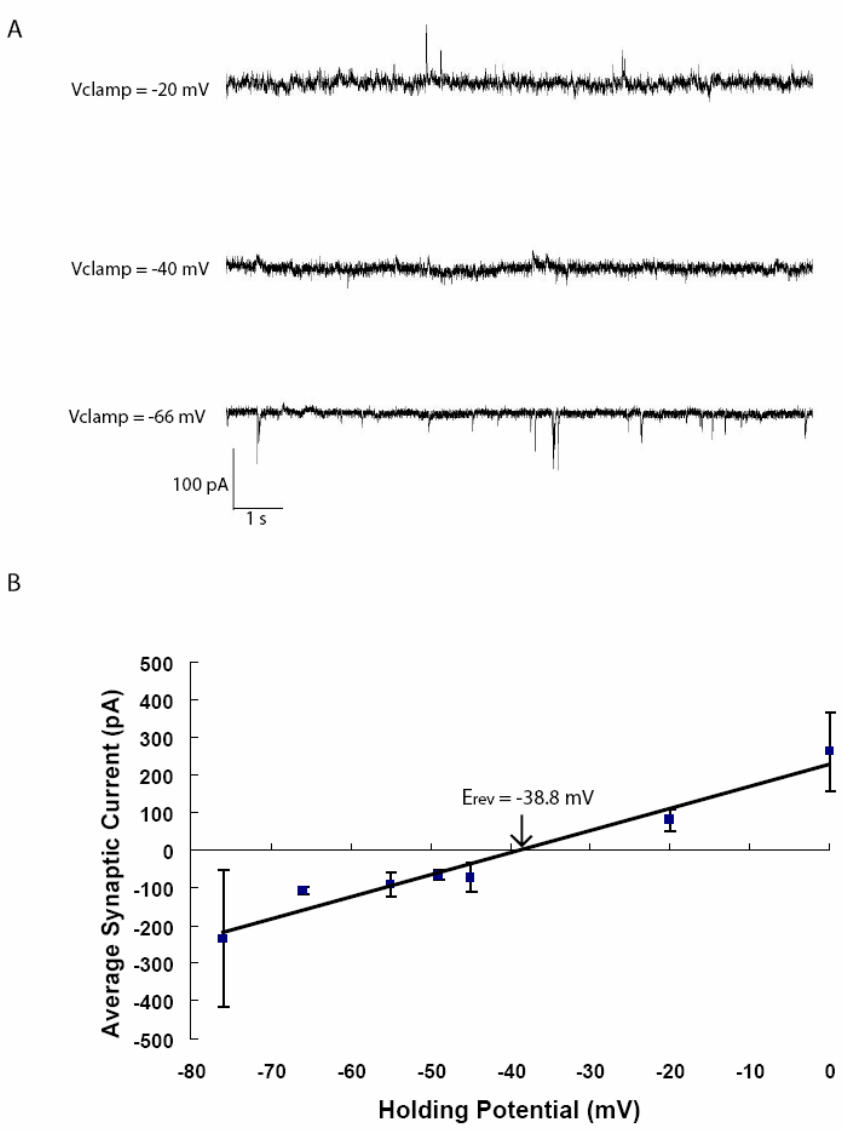

Figure 2.8 Spontaneous activities in voltage clamp mode. (A) Spontaneous EPSCs at different holding potentials, note that - 66 mV is the resting membrane potential for this neuron. (B) Synaptic currents of spontaneous EPSCs versus holding potentials. The values of synaptic currents were obtained by averaging over EPSCs (as described in text).

Figure 2.9 Gramicidin-perforated patch recordings of spontaneous activity in lpc neuron. *Left*, in control condition, spontaneous spikes and EPSPs persisted; *Right*, with application of 100 μM bicuculline, spontaneous activity was completely eliminated.

2.9A) and with application of 100 μM bicuculline, spontaneous activities was completely eliminated (Fig. 2.9B).

Pairwise Recordings

To determine whether spontaneous synaptic inputs of lpc cells are correlated or lpc cells are coupled with each other, we recorded from two adjacent lpc neurons (within 50 μm) simultaneously. In all recorded pairs (n = 15), most spontaneous EPSPs were uncorrelated (Fig. 2.10A). Very rarely, some synchronized EPSPs and spikes were found (Fig. 2.10B, asterisked). These pairs of lpc neurons appeared not to be coupled, since spikes in one cell did not cause any voltage deflection in the other (Fig. 2.10C).

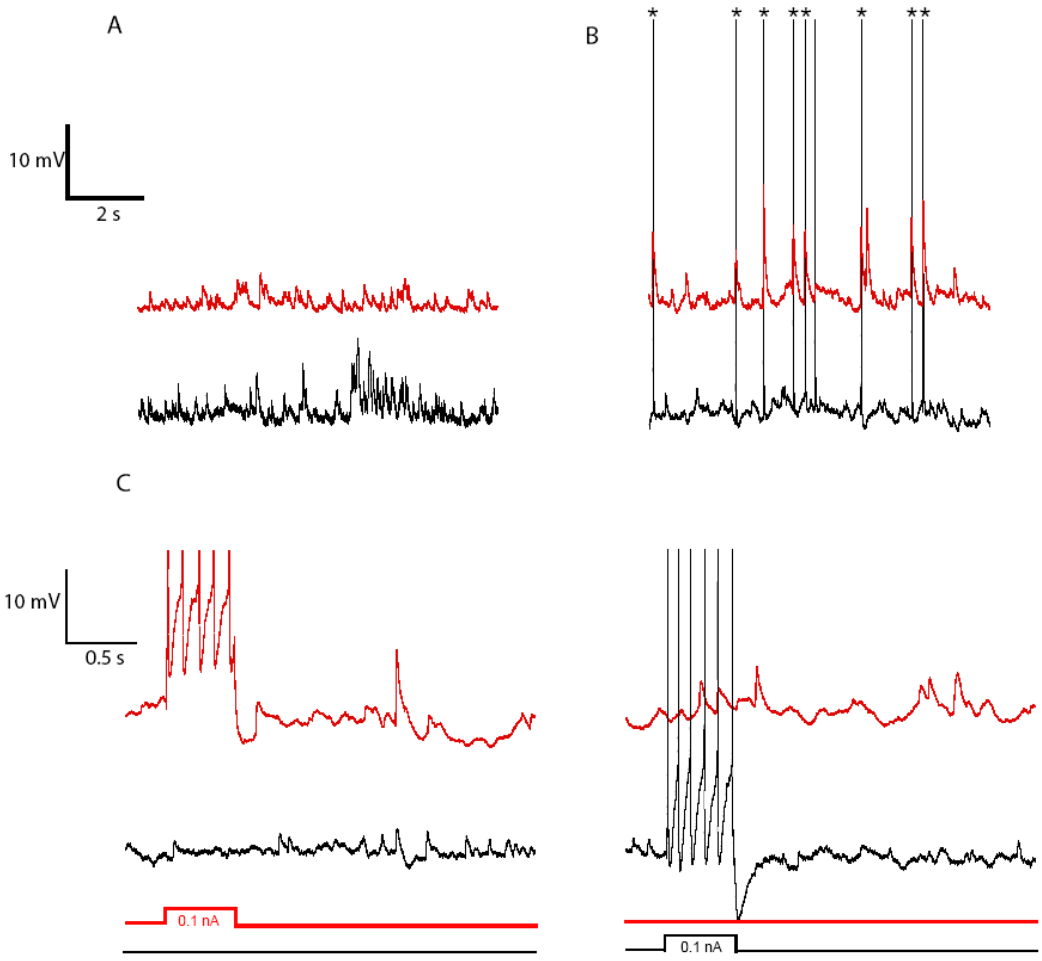

Figure 2.10 Simultaneous recordings of two adjacent Ipc neurons. (A) Spontaneous EPSPs of two Ipc neurons were not synchronized. Red trace, RMP = - 58 mV; black trace, RMP = - 54 mV. (B) Synchronized EPSPs and spikes were found in one pair of Ipc neurons (starred). (C) Somatic current injection into one Ipc neuron (action potentials truncated) did not evoke any voltage deflection in the other neuron.

To examine if there was spontaneous synchrony between tectum and Ipc, we conducted pairwise recordings from Ipc neuron and L10 neuron. The recorded pairs of Ipc and L10 neuron were chosen to be within a same column given that the reciprocal connections between L10 and Ipc are in a columnar way (Wang et

al, 2006). However, all recorded pairs of neurons (n = 4) were not synaptically connected in that spikes in one cell did not cause any voltage deflection in the other (data not shown). L10 neurons had fewer spontaneous EPSPs than those in lpc neurons (Fig 2.11, red trace). In 2 pairs of recorded neurons, occasional strong spontaneous inputs were found synchronized between lpc and L10 neurons. This suggests that lpc and tectal L10 neurons may share some strong common synaptic inputs, possibly from upper tectal layers given that the synchronized activity always started first at L10 neurons (Fig 2.11, inset).

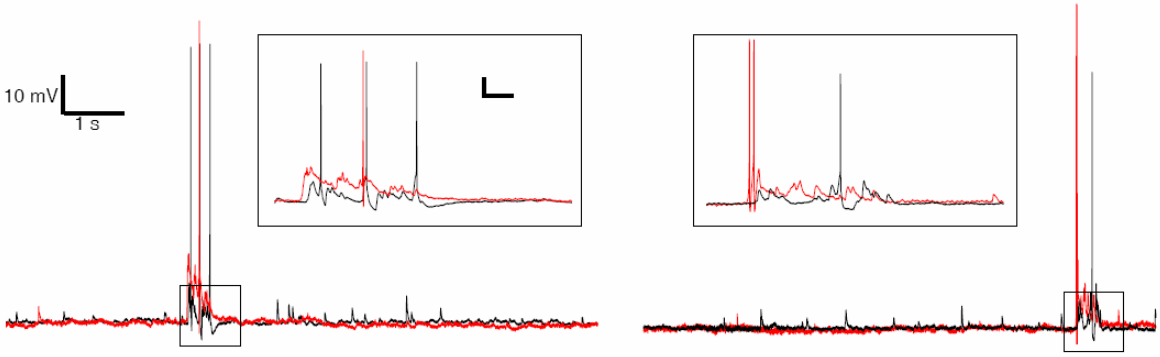

Figure 2.11 Simultaneous recordings of one lpc neuron and one L10 neuron. Black trace, recordings from lpc neuron, RMP = - 52 mV; Red trace; recordings from L10 neuron, RMP = - 57 mV. Scare bar in insets: 10 mV, 100 ms.

2.5 Discussion

In this study, we found that lpc neurons exhibit spontaneous EPSPs and spikes and that the distribution of inter-EPSP-intervals has an exponential shape suggesting a Poisson process for the generation of the EPSPs. The

pharmacological experiments showed that only bicuculline could effectively block all the spontaneous EPSPs in Ipc neurons implying that GABA mediates the EPSPs. Voltage clamp recordings from Ipc somata revealed that the spontaneous synaptic currents reversed sign at a membrane potential of approximately -40 mV. Interestingly, the application of GABA to control slices depolarized the Ipc membrane potential to the same level. By recording simultaneously from two adjacent Ipc neurons, we demonstrated that spontaneous EPSPs are uncorrelated within Ipc neurons and Ipc cells appear not to be coupled. This observation is consistent with the fact that there is also no anatomical evidence for coupling between Ipc neurons (Wang et al, 2006).

Though depolarizing actions of GABAergic currents usually occur in animal's early development phase (Ben-Ari, 2002), several factors lead us to propose that GABA-mediated spontaneous EPSPs in Ipc neurons is part of their mature phenotype and not an indicator of immaturity. First, the observation that Ipc neurons fire spontaneously in vitro is consistent with reports of spontaneous activity found in adult birds *in vivo* (Sherk 1979; Yan and Wang, 1986; Marin et al., 2005; Maczko et al., 2006). Second, we have recorded spontaneous EPSPs in Ipc neurons from chicks up to 10 days after hatching (data shown in Chapter 5). Third, our previous studies on the RGC-SGC pathway, which also used the midbrain slices preparation from P1-P3 chicks (Khanbabaie et al., 2007), indicate that the GABAergic horizontal neurons in tectal layer 5 hyperpolarize the postsynpatic SGC-I neurons, implying that the chloride concentration in SGC-I

neuron has already reached mature state at this age. Last, the behavior of chick shows that they are able to see and seek food immediately after hatching.

It is known that cholinergic PBN, the analog of Ipc in mammal, is spontaneously spiking because of its intrinsic excitability (Goddard et al., 2007).Here, however, we demonstrate that higher potassium concentration in ACSF results in a higher frequency of spontaneous EPSPs (Fig 2.4B), which implies that spontaneous EPSPs in Ipc are driven by synaptic inputs. The fact that spontaneous EPSPs are blockable by bicuculline and that Ipc only receives GABAergic inputs from Imc (Wang et al., 2004, 2006) suggests that Imc is the possible origin of spontaneous synaptic inputs to the Ipc. This hypothesis is also consistent with the fact that Imc shows a higher spontaneous firing rate than Ipc in vivo recordings (Sherk 1979; Yan and Wang, 1986; Marin et al., 2007). However, this raises another question: what are the spontaneous inputs to Imc neurons or are Imc neurons spontaneously active because of their intrinsic excitability? It is known that Imc only receives inputs from the optic tectum (Wang et al., 2004, 2006). Could optic tectum be the origin of spontaneous inputs to the nucleus isthmi? But when the optic tectum was surgically removed from the slice, the Ipc neurons still exhibited strong spontaneous EPSPs (Fig 2.5). And our pairwise recordings from Ipc neurons and L10 neurons showed that L10 neurons, which project to nucleus isthmi, actually had less spontaneous EPSPs than Ipc. The fact that some spontaneous EPSPs were still found in Ipc neurons even with application of 1 μM TTX implies an additional source of spontaneous GABA

releases that is not driven by spikes. One such possibility would be GABA release from glia cells, however, we have no evidence to support this hypothesis at present.

The Ipc in birds has been reported to affect the receptive fields of tectal neurons (Wang et al., 2000), generate oscillatory bursts in the tectum (Marin et al., 2005) and mediate shift of attention in birds (Marin et al., 2007). However, the function of spontaneous activity in the Ipc is not known yet. The subthreshold spontaneous EPSPs in Ipc embed the neural information transfer within isthmotectal feedback loop in a noisy background, thus it might contribute to the network dynamics since noise has been reported to be of great importance to many neural systems (Douglass et al., 1993; Wiesenfeld and Moss 1995). Spontaneous firing occurs frequently in neuromodulatory regions, such as the suprachiasmatic nucleus (Jackson et al., 2004; Pennartz et al., 1997) and in dopaminergic centers (Koyama et al., 2005; Puopolo et al., 2007). The finding that the Ipc is spontaneously active implies that the Ipc delivers a continuous, low level of ACh to the optic tectum. ACh has been reported to alter synaptic transmission in the superior colliculus of rodent (Endo et al., 2005; Lee eta l., 2001; Li et al., 2004), reduce saccade latency in monkeys (Aizawa et al., 1999) and also be crucial for attention (Hasselmo and McGaughy 2004). Therefore, spontaneous activity in Ipc may provide a constant regulation on the activity of tectal neurons for visual processing.

2.6 Reference

Aizawa H, Kobayashi Y, Yamamoto M, Isa T (1999) Injection of nicotine into the superior colliculus facilitates occurrence of express saccades in monkeys. J Neurophysiol 82: 1642-1646.

Arrigoni E, Chamberlin NL, Saper CB, McCarley RW (2006) Adenosine inhibits basal forebrain cholinergic and noncholinergic neurons in vitro. Neuroscience 140: 403-413.

Ashe JH, McKenna TM, Weinberger NM (1989) Cholinergic modulation of frequency receptive fields in auditory cortex: II. Frequency-specific effects of anticholinesterases provide evidence for a modulatory action of endogenous ACh. Synapse 4: 44-54.

Ben-Ari Y (2002) Excitatory actions of GABA during development: the nature of the nurture. Nat Rev Neurosci 3:728-739

Bravo H and Pettigrew JD (1981) The distribution of neurons projecting from the retina and visual cortex to the thalamus and tectum opticum of the barn owl, Tyto alba, and the burrowing owl, Speotyto cunicularia. J Comp Neurol 199(3):419-441.

Chaves LM and Hodos W (1998) Color reversal-learning deficits after tectofugal pathway lesions in the pigeon telencephalon. Behav Brain Res 90(1):1-12.

Cui H and Malpeli JG (2003) Activity in the parabigeminal nucleus during eye movements directed at moving and stationary targets. J Neurophysiol 89: 3128-3142.

Douglass JK, Wilkens L, Pantazelou E, Moss F (1993) Noise enhancement of information transfer in crayfish mechanoreceptors by stochastic resonance. Nature 365:337-340.

Endo T, Yanagawa Y, Obata K, Isa T (2005) Nicotinic acetylcholine receptor subtypes involved in facilitation of GABAergic inhibition in mouse superficial superior colliculus. J Neurophysiol 94: 3893-3902.

Goddard CA, Knudsen EI, Huguenard JR (2007) Intrinsic excitability of cholinergic neurons in the rat parabigeminal nucleus. J Neurophysiol 98: 3486-3493.

Hasselmo ME and McGaughy J (2004) High acetylcholine levels set circuit dynamics for attention and encoding and low acetylcholine levels set dynamics for consolidation. Prog Brain Res 145: 207-231.

Hodos W and Karten HJ (1974) Visual intensity and pattern discrimination deficits after lesions of the optic lobe in pigeons. Brain Behav Evol 9(3):165-194.

Jackson AC, Yao GL, Bean BP (2004) Mechanism of spontaneous firing in dorsomedial suprachiasmatic nucleus neurons. J Neurosci 24: 7985-7998.

Khanbabaie R, Mahani AS, Wessel R (2007) Contextual interaction of GABAergic circuitry with dynamic synapses. J Neurophysiol 97: 2802-2811.

Koyama S, Kanemitsu Y, Weight FF (2005) Spontaneous activity and properties of two types of principal neurons from the ventral tegmental area of rat. J Neurophysiol 93: 3282-3293

Kyrozis A and Reichling DB (1995) Perforated-patch recording with gramicidin avoids artifactual changes in intracellular chloride concentration. J Neurosci Methods 57(1):27-35.

Lee P and Hall WC (2006) An in vitro study of horizontal connections in the intermediate layer of the superior colliculus. J Neurosci 26: 4763-4768.

Lee PH, Schmidt M, Hall WC (2001) Excitatory and inhibitory circuitry in the superficial gray layer of superior colliculus. J Neurosci 21: 8145-8153

Li F, Endo T, Isa T (2004) Presynaptic muscarinic acetylcholine receptors suppress GABAergic synaptic transmission in the intermediate grey layer of mouse superior colliculus. Eur J Neurosci 20: 2079-2088

Luksch H, Khanbabaie R, Wessel R (2004) Synaptic dynamics mediate sensitivity to motion independent of stimulus details. Nature Neurosci 7:380-388.

Maczko KA, Knudsen PF, Knudsen EI (2006) Auditory and visual space maps in the cholinergic nucleus isthmi pars parvocellularis in the barn owl. J Neurosci 26: 12799-12806.

Marin G, Mpodozis, Sentis E, Ossandon T, Letelier JC (2005) Oscillatory bursts in the optic tectum of birds represent re-entrant signals from the nucleus isthmi pars parvocellularis. J Neurosci 25: 7081-7089.

Marin G, Salas C, Sentic E, Rojas X, Letelier JC, Mpodozis J (2007) A cholinergic gating mechanism controlled by competitive interactions in the optic tectum of the pigeon. J Neurosci 27: 8112-8121.

McKenna R, Ashe JH, Weinberger NM (1989) Cholinergic modulation of frequency receptive fields in auditory cortex: I. Frequency-specific effects of muscarinic agonists. Synapse 4: 30-43.

Metherate R, Tremblay N, Dykes RW (1988) The effects of acetylcholine on response properties of cat somatosensory cortical neurons. J Neurophysiol 59: 1231-1252.

Monsivais P and Rubel EW (2001) Accommodation enhances depolarizing inhibition in central neurons. J Neurosci 21(19): 7823-7830.

Mufson EJ, Martin TL, Mash DC, Wainer BH, Mseulam MM (1986) Cholinergic projections from the parabigeminal nucleus (Ch8) to the superior colliculus in the mouse: a combined analysis of horseradish peroxidase transport and choline acetyltransferase immunohistochemistry. Brain Res 370: 144-148.

Pennartz CM, Bierlaagh MA, Geurtsen AM (1997) Cellular mechanisms underlying spontaneous firing in rat suprachiasmatic nucleus: involvement of a slowly inactivating component of sodium current. J Neurophysiol 78: 1811-1825.

Puopolo M, Raviola E, Bean BP (2007) Roles of subthreshold calcium current and sodium current in spontaneous firing of mouse midbrain dopamine neurons. J Neurosci 27: 645-656.

Sherk H (1979) A comparison of visual-response properties in cat's parabigeminal nucleus and superior colliculus. J Neurophysiol 42: 1640-1655.

Tokunaga A and Otani K (1978) Neuronal organization of the corpus parabigeminum in the rat. Exp Neurol 58: 361-375.

Wang SR (2003) The nucleus isthmi and dual modulation of the receptive field of tectal neurons in non-mammals. Brain Res Rev 41: 13-25.

Wang Y, Major DE, & Karten HJ (2004) Morphology and connections of nucleus isthmi pars magnocellularis in chicks (*gallus gallus*). J Comp Neurol 469: 275-297.

Wang Y, Luksch H, Brecha NC, Karten HJ (2006) Columnar projections from the cholinergic nucleus isthmi to the optic tectum in chicks (*Gallus gallus*): A possible substrate for synchronizing tectal channels. J Comp Neurol 494:7-35.

Wang Y, Xiao J, Wang SR (2000) Excitatory and inhibitory receptive fields of tectal cells are differentially modified by magnocellular and parvocellular divisions of the pigeon nucleus isthmi. J Comp Physiol A, 186: 505-511.

Wiesenfeld K and Moss F (1995) Stochastic resonance and the benefits of noise: from ice ages to crayfish and SQUIDs. Nature 373: 33-36.

Wilson CJ (2005) The mechanism of intrinsic amplification of hyperpolarizations and spontaneous bursting in striatal cholinergic interneurons. Neuron 45: 575-585.

Yan K and Wang SR (1986) Visual responses of neurons in the avian nucleus isthmi. Neurosci Lett 64: 340-344.

Chapter 3

GENERATING OSCILLATORY BURSTS FROM A NETWORK OF REGULAR SPIKING NEURONS WITHOUT INHIBITION

3.1 Abstract

Avian nucleus isthmi pars parvocellularis (Ipc) neurons are reciprocally connected with the layer 10 (L10) neurons in the optic tectum and respond with oscillatory bursts to visual stimulation. Our *in vitro* experiments show that both neuron types respond with regular spiking to somatic current injection and that the feedforward and feedback synaptic connections are excitatory, but of different strength and time course. To elucidate mechanisms of oscillatory bursting in this network of regularly spiking neurons, we investigated an experimentally constrained model of coupled leaky integrate-and-fire neurons with spike-rate adaptation. The model reproduces the observed Ipc oscillatory bursting in response to simulated visual stimulation. A scan through the model parameter volume reveals that Ipc oscillatory burst generation can be caused by strong and brief feedforward synaptic conductance changes. The mechanism is sensitive to the parameter values of spike-rate adaptation. In conclusion, we show that a network of regular-spiking neurons with feedforward excitation and spike-rate adaptation can generate oscillatory bursting in response to a constant input.

3.2 Introduction

Oscillatory bursts play an important role in stimulus encoding (Gabbiani et al. 1996; Lesica, Stanley 2004; Oswald et al. 2004; Reinagel et al. 1999) and in the communication between neurons (Izhikevich et al. 2003; Lisman 1997; Sherman 2001). Mechanisms of oscillatory burst generation (Coombes and Bressloff 2005) range from the interaction of fast and slow currents in single neurons (Izhikevich 2007; Krahe and Gabbiani 2004; Rinzel and Ermentrout 1998; Wang and Rinzel 2003) to the interaction of neurons in networks typically consisting of excitatory and inhibitory connections (Buzsaki 2006; Traub et al. 2004). Here, we investigate oscillatory burst generation in a recurrently connected network of spiking neurons with excitatory synapses, where activity-dependent adaptation replaces the stabilizing role of inhibition.

The avian isthmotectal system (Fig. 3.1) plays a key role in visual information processing (Cook 2001; Maczko et al. 2006; Marin et al. 2007; Wang 2003). It consists of three key anatomical elements. A subpopulation of tectal layer 10 (L10) neurons receive retinal inputs and project to the ipsilateral nucleus isthmi pars parvocellularis (Ipc) and the nucleus isthmi pars magnocellularis (Imc) in a topographic fashion (Wang et al. 2004, 2006). The cholinergic Ipc neurons form topographic reciprocal connections with the tectum, where their axons terminate in a columnar manner ranging from layer 2 to 12 (Wang et al. 2006). The GABAergic Imc neurons consist of two cell types. One type projects broadly to

the Ipc, whereas the other type projects upon tectal layers 10 to 13 (Wang et al. 2004).

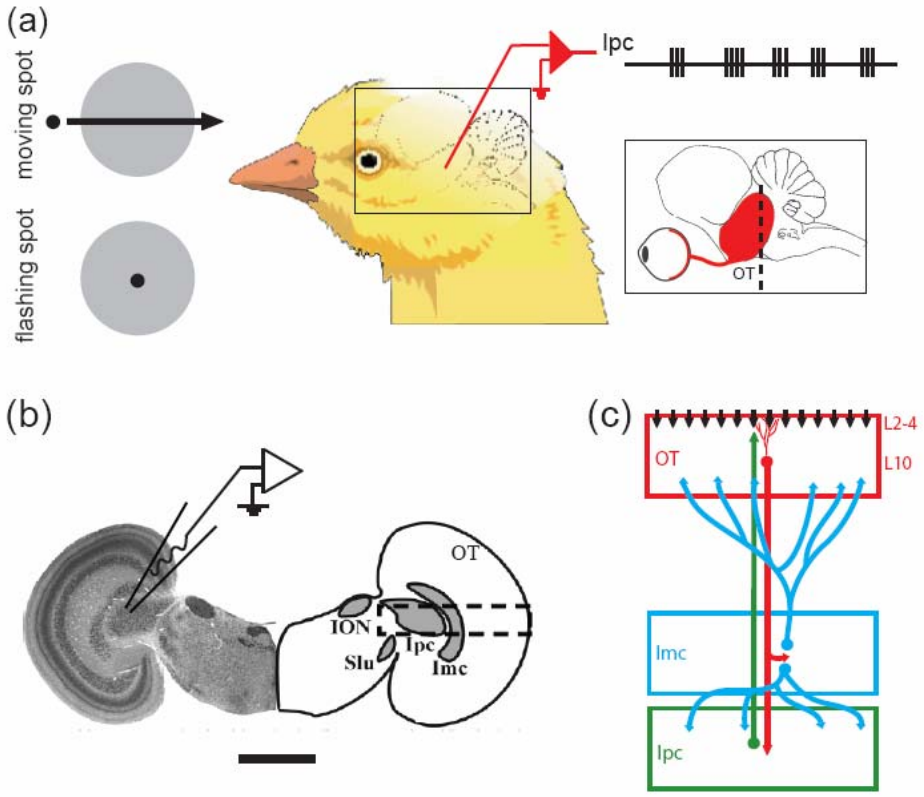

Figure 3.1 Schematic drawings of *in vivo* and *in vitro* recording set-ups. (a) Recordings *in vivo* showed that nucleus isthmi pars parvocellularis (Ipc) neurons responded to moving dots and flashing dots with oscillatory bursts (Marin et al. 2005). The rectangle inset shows a schematic lateral view of the chick brain with the retina, optic nerve, and optic tectum (OT) in red. The dashed line indicates the approximate location of the transverse slicing. (b) A transverse slice of the chick midbrain both in histological image and corresponding outlines (scale bar = 2 mm). The nucleus isthmo-opticus (ION) and the nucleus semilunaris (SLu) are not considered in this

study. The patch-electrode schematic indicates a typical recording location from an Ipc neuron. The dashed rectangle indicates the location of the schematic circuitry described in (c). (c) Schematic drawings of the isthmotectal circuitry consisting of the retinal ganglion cells axons (vertical black arrows), the tectal layer 10 (L10) neurons (red), the Ipc neurons (green), and the nucleus isthmi pars magnocellularis (Imc) neurons (blue).

Ipc neurons respond with fast oscillatory bursts to flashing or moving visual stimulations (Fig. 3.1(a); Marin et al. 2005). Because of the extensive arborisation of Ipc axons in upper tectal layers (Wang et al. 2006), the Ipc oscillatory bursts (Marin et al. 2005) are also detected in extracellular recordings from superficial and intermediate tectal layers (Knudsen 1982; Neuenschwander and Varela 1993; Neuenschwander et al. 1996). Thus, as pointed out by Marin and co-workers, oscillatory burst recordings in the tectum may falsely be interpreted as oscillatory bursts originating in the tectum (Marin et al. 2005). The oscillatory bursts in tectal recordings disappear after injecting micro-drops of lidocaine into the corresponding area of the Ipc nucleus (Marin et al. 2005), thus confirming the role of the Ipc neurons in the oscillatory burst generation. The Ipc nucleus receives two inputs (Fig. 3.1(b), (c)). It receives glutamatergic (Hellmann et al. 2001; Marin et al. 2007) and possibly cholinergic (Britto et al. 1992; Wang et al. 2006) inputs from a subpopulation of tectal L10 neurons, characterized by unusual “shepherd’s crook” axons that arise from the apical dendrite and then make a U-turn to leave the tectum through deeper layers (Wang et al. 2006). It

receives GABAergic input from the adjacent Imc nucleus (Wang et al. 2004). Importantly, the Ipc oscillatory burst responses persist when the Imc nucleus is inactivated via local application of CNQX (see Fig. 3.7D in Marin et al. 2007). Further, the retinal inputs to L10 neuron dendrites in upper tectal layers (Fig. 3.1(c)) show no evidence of bursting; rather in vivo recordings seem to suggest that spots of light produce continuous and long-lasting evoked potentials in superficial tectal layers (Holden 1980; Letelier et al. 2000). These observations narrow down the possible mechanisms for the observed Ipc oscillatory burst generation to the reciprocally connected L10 and Ipc neurons. For instance, the delays in the reciprocal connection (Meyer et al. 2008) could imply the involvement of delayed feedback in the induction of oscillatory dynamics (Brandt et al. 2006; Brandt and Wessel 2007; Brandt et al. 2007; Chacron et al. 2005; Doiron et al. 2003; Laing and Longtin 2003; Milton 1996).

To investigate the mechanisms of the observed oscillatory bursting in Ipc, we conducted whole-cell recordings from L10 and Ipc neurons combined with synaptic stimulations in chick brain slice preparations (Fig. 3.1(b)). Based on the in vitro experimental results, we built a model network consisting of reciprocally connected leaky integrate-and-fire neurons, representing L10 and Ipc neurons, and tested under what conditions this experimentally constrained model network reproduces the observed bursting activity in Ipc.

3.3 Methods

3.3.1 Experiments

White Leghorn chick hatchlings (*Gallus gallus*) of less than 3 days of age were used in this study. All procedures used in this study were approved by the local authorities and conform to the guidelines of the National Institutes of Health on the Care and Use of Laboratory Animals. Animals were injected with ketamine (40 mg per kg, i.m.). Brain slices of the midbrain were prepared following published protocols (Dye and Karten 1996; Luksch et al. 2001). Briefly, preparations were done in 0°C, oxygenated, and sucrose-substituted saline (240 mM sucrose, 3 mM KCl, 5 mM $MgCl_2$, 0.5 mM $CaCl_2$, 1.2 mM NaH_2PO_4, 23 mM $NaHCO_3$, and 11 mM D-glucose). After decapitation, the brains were removed from the skull, and the forebrain, cerebellum, and medulla oblongata were discarded. A midsagittal cut was used to separate the tectal hemispheres. The tectal hemispheres were sectioned at 500 μm on a tissue slicer (Vibroslice, Campden or VF-200, Precisionary Instruments) in either the transverse or the horizontal plane. Slices were collected in oxygenated saline (120 mM NaCl, 3 mM KCl, 1 mM $MgCl_2$, 2 mM $CaCl_2$, 1.2 mM NaH_2PO_4, 23 mM $NaHCO_3$, and 11 mM D-glucose) and kept submerged in a chamber that was bubbled continuously with carbogen (95% oxygen, 5% CO_2) at room temperature. The slice was then transferred to a recording chamber (RC-26G, Warner Instruments) mounted on a fixed-stage upright microscope equipped with differential interference contrast optics (BX-51WI, Olympus). The slice was held gently to the bottom of the chamber with an anchor of nylon threads, and the chamber was perfused

continuously with oxygenated saline at room temperature. The potential effects of temperature or age on measured cellular and synaptic properties were not addressed in this study. The L10 and Ipc neurons are visible with DIC optics.

Local electrical stimulation was achieved by inserting bipolar tungsten electrodes under visual control into either the tectal layers 10/11, or the Ipc nuclei with a three-axis micromanipulator (U-31CF, Narishige). Electrodes were custom-built from 50-µm diameter, insulated tungsten wires (California Fine Wire) that were glued together with cyanoacrylate and mounted in glass micro capillaries for stabilization. The wires protruded several hundred µm from the capillaries, and the tips were cut at an angle. Stimulus isolators (Isolated Pulse Stimulator 2100, AM Systems) generated biphasic current pulses (20 – 200 µA, 500 µs).

Whole-cell recordings were obtained with glass micropipettes pulled from borosilicate glass (1.5 mm OD, 0.86 mm ID, AM Systems) on a horizontal puller (P-97, Sutter Instruments or DMZ Universal Puller, Zeitz Instruments) and were filled with a solution containing 100 mM K-Gluconate, 40 mM KCl, 10 mM HEPES, 0.1 mM $CaCl_2$, 2 mM $MgCl_2$, 1.1 mM EGTA, 2 mM Mg-ATP, pH adjusted to 7.2 with KOH. Electrodes were advanced through the tissue under visual guidance with a motorized micromanipulator (MP-285, Sutter Instruments) while constant positive pressure was applied and the electrode resistance was monitored by brief current pulses. Once the electrode had attached to a membrane and formed a seal, access to the cytosol was achieved by brief

suction. Whole-cell recordings were performed with the amplifier (Axoclamp 2B, Axon Instruments or SEC-05L, npi-electronic) in the bridge mode (current clamp). The liquid junction potential was measured and estimated to be approximately -10 mV. This correction was ignored, i.e., the real membrane potentials are more negative than the stated values. The series resistance was estimated by toggling between the bridge and the DCC (discontinuous current clamp) mode, and subsequently compensated with the bridge balance. Depolarizing and hyperpolarizing currents were injected through intracellular electrodes. Analog data were low-pass filtered (4-pole Butterworth) at 1 kHz, digitized at 5 kHz, stored, and analyzed on a PC equipped with a PCI-MIO-16E-4 and LabView software (both National Instruments).

Labeling of a subset of recorded neurons was carried out as described previously (Luksch et al. 1998; Mahani et al. 2006). In brief, whole-cell patch recordings were obtained as described above. Additionally, the electrode solution contained 0.5% Biocytin (w/v) to label the recorded neurons. Individual cells were filled intracellularly with 2 nA of positive current injection over 3 minutes through the patch electrode. After recording and labeling, slices were kept in oxygenated ACSF for an additional 30 minutes and subsequently fixed by immersion in 4% paraformaldehyde in PB for at least 4 hours. Slices were then washed in phosphate buffer (PB, 0.1 M, pH 7.4) for at least 4 hours, immersed in 15% sucrose in PB for at least 4 hours and then immersed in 30% sucrose in PB for 12 hours, and resectioned at 60 µm on a freezing microtome. The sections were

collected in PB and the endogenous peroxidase blocked by a 15-minute immersion in 0.6% hydrogen peroxide in methanol. The tissue was washed several times in PB, and then incubated in the avidin-biotin complex solution (ABC Elite kit, Vector Labs) and the reaction product visualized with a heavy-metal intensified DAB protocol. Following several washes in PB, the 60 µm-thick sections were mounted on gelatin-coated slides, dried, dehydrated, and coverslipped. Sections were inspected for labeled neurons, and only data from cells that could unequivocally be classified according to published criteria (Wang et al. 2004, 2006) were taken for further analysis. Cells were reconstructed at medium magnification (10x or 20x) with a camera lucida on a Leica microscope and projected onto the 2D plane.

3.3.2 Two-Neuron Model

We investigated the network dynamics of two reciprocally connected model neurons, representing the L10 and the Ipc neuron in the avian isthmotectal system. Each model neuron is of the leaky integrate-and-fire type with spike-rate adaptation. The dynamic of the membrane potentials V_{L10} and V_{Ipc} are determined by two coupled differential equations:

$$\tau_{m,L10}\frac{dV_{L10}}{dt} = E_{r,L10} - V_{L10} - R_{m,L10}(I_{sra,L10} + I_{Ipc\to L10} - I_{e,L10}) \quad (1)$$

$$\tau_{m,Ipc}\frac{dV_{Ipc}}{dt} = E_{r,Ipc} - V_{Ipc} - R_{m,Ipc}(I_{sra,Ipc} + I_{L10\to Ipc}) \quad (2)$$

where $E_{r,L10}$ denotes the resting membrane potential of the L10 neuron, $R_{m,L10}$ is the membrane input resistance, and $\tau_{m,L10}$ is the membrane time constant. The

measured membrane time constants (Table 3.1) are larger than the measured axonal delays (Meyer et al. 2008). Thus delays in synaptic voltage responses of leaky integrate-and-fire model neurons are dominated by the membrane time constants. Therefore, we did not explicitly include axonal delays in the network model. When the membrane potential V_{L10} reaches the threshold $V_{\theta,L10}$ it is reset to $V_{reset,L10}$ instantaneously. This is interpreted as the occurrence of a spike. The external current input $I_{e,L10}$ to the L10 neuron represents the stimulus from the retinal ganglion cell. The spike-rate adaptation current,

$$I_{sra,L10} = g_{sra,L10}(t)(V_{L10} - E_{sra,L10}) \tag{3}$$

has the adaptation reversal potential $E_{sra,L10}$, and the time varying adaptation conductance $g_{sra,L10}(t)$, which evolves according to the differential equation

$$\tau_{sra,L10} \frac{dg_{sra,L10}}{dt} = -g_{sra,L10} \tag{4}$$

Whenever the neuron fires a spike, the adaptation conductance changes according to

$$g_{sra,L10}(t^+) \rightarrow g_{sra,L10}(t^-) + \Delta g_{sra,L10} \tag{5}$$

The synaptic current

$$I_{Ipc\rightarrow L10} = g_{Ipc\rightarrow L10} P_{Ipc\rightarrow L10}(t)(V_{L10} - E_{Ipc\rightarrow L10}) \tag{6}$$

from the Ipc neuron to the L10 neuron projection is proportional to the open probability $P_{Ipc\rightarrow L10}(t)$ of the synaptic conductance, where $g_{Ipc\rightarrow L10}$ is the maximum synaptic conductance and $E_{Ipc\rightarrow L10}$ is the synaptic reversal potential. The open

Neuron	$\tau_m\,(ms)$	$R_m\,(\mathrm{M}\Omega)$	$E_r\,(mV)$	$V_\theta\,(mV)$	$V_{reset}\,(mV)$	$\tau_{sra}\,(ms)$	$\Delta g_{sra}\,(nS)$	$E_{sra}\,(mV)$
L10	104	480	-55	-39	-50	50	1.25	-70
Ipc	25	135	-61	-40	-50	60	8.15	-70

Table 3.1 Single neuron parameters.Abbreviations: τ_m = membrane time constant, R_m= membrane input resistance, E_r = resting membrane potential, V_θ = threshold for spiking, V_{reset} = reset voltage, τ_{sra} = spike-rate adaptation time constant, Δg_{sra} = spike-rate adaptation conductance increment, E_{sra} = spike-rate adaptation reversal potential.

probability $P_{Ipc\to L10}(t)$ of the synaptic conductance from the Ipc to the L10 neuron has the form

$$P_{Ipc\to L10}(t) = B_{Ipc\to L10}\sum_k\left(\exp(-\frac{t-t_{Ipc}^k}{\tau_{1,Ipc\to L10}})-\exp(-\frac{t-t_{Ipc}^k}{\tau_{2,Ipc\to L10}})\right) \tag{7}$$

where the normalization factor

$$B_{Ipc\to L10} = \left(\left(\frac{\tau_{2,Ipc\to L10}}{\tau_{1,Ipc\to L10}}\right)^{\tau_{rise,Ipc\to L10}/\tau_{1,Ipc\to L10}} - \left(\frac{\tau_{2,Ipc\to L10}}{\tau_{1,Ipc\to L10}}\right)^{\tau_{rise,Ipc\to L10}/\tau_{2,Ipc\to L10}}\right)^{-1} \tag{8}$$

ensures that the peak value of $P_{Ipc\to L10}(t)$ generated by a single spike equals to 1, the variable t_{Ipc}^k represents the time at which the Ipc neuron generates the *kth* spike, and a summation is performed over all spikes generated by the Ipc neuron. The time constant $\tau_{1,Ipc\to L10}$ and $\tau_{2,Ipc\to L10}$ ($\tau_{1,Ipc\to L10} > \tau_{2,Ipc\to L10}$) determine the time course of the synaptic conductance change. The synaptic rise time

is $\tau_{rise,Ipc\to L10} = \frac{\tau_{1,Ipc\to L10}\tau_{2,Ipc\to L10}}{\tau_{1,Ipc\to L10} - \tau_{2,Ipc\to L10}}$, while $\tau_{1,Ipc\to L10}$ represents the fall time. The variables and parameters of the Ipc model neuron in Eq. (2) are all analogous to those of the L10 model neuron. The Ipc model neuron does not receive an external current input.

The Ipc steady-state response (taken to start 100 ms after stimulus onset) is represented by the "burst score" (Fig. 3.5). A spike preceded by an inter-spike-interval (ISI) of more than 10 ms and followed by an ISI of less than 4 ms is classified as the beginning of a burst. Subsequent spikes with ISIs of less than 4 ms are part of the burst. All other spikes are classified as isolated (Sillito and Jones 2002). The burst score is defined by the number of bursts divided by the sum of the number of bursts and the number of isolated spikes in the steady-state response. The score equals 1 when all spikes belong to bursts and equals 0 when all spikes are isolated. When the firing rate exceeds 1000 Hz the Ipc response is classified as diverging.

3.3.3 Population model with uncorrelated noise

For the population model of L10 and Ipc neurons (Fig. 3.6a) each individual neuron is of the leaky integrate-and-fire type with spike-rate adaptation as described above. Each population consists of 400 neurons. When referring to an individual neuron, we use the subscript i for L10 neurons and the subscript j for

Ipc neurons. The dynamics of the membrane potentials V_i (L10 neuron i) and V_j (Ipc neuron j) are determined by the coupled differential equations:

$$\tau_{m,L10}\frac{dV_i}{dt} = E_{r,L10} - V_i - R_{m,L10}(I_{sra,i} + I_{Ipc\to i} - I_{e,i} + \chi_i) \tag{9}$$

$$\tau_{m,Ipc}\frac{dV_j}{dt} = E_{r,Ipc} - V_j - R_{m,Ipc}(I_{sra,j} + I_{L10\to j} + \chi_j) \tag{10}$$

The synaptic currents, $I_{L10\to j}$ and $I_{Ipc\to i}$, are similar in form to the one described above, Eq. (7), but now include contributions from a population of presynaptic neurons. For instance, the synaptic current in Ipc neuron j

$$I_{L10\to j} = \sum_i g_{L10\to Ipc} P_{ji}(t) W_{ji}(V_j - E_{L10\to Ipc}) \tag{11}$$

includes contributions from all L10 synaptic inputs to Ipc neuron j. The synaptic conductance is the product of the maximum synaptic conductance, $g_{L10\to Ipc}$, and the weight distribution

$$W_{ji} = \exp\left(-\frac{(i-j)^2}{2\Delta^2_{L10\to Ipc}}\right) \tag{12}$$

of width $\Delta_{L10\to Ipc}$. The latter reflects the narrow topographic projection from L10 to Ipc (Wang et al. 2006). The open probability of the synaptic conductance from L10 neuron i to Ipc neuron j has the form

$$P_{ji}(t) = B_{L10\to Ipc}\sum_k\left(\exp(-\frac{t-t_i^k}{\tau_{1,L10\to Ipc}}) - \exp(-\frac{t-t_i^k}{\tau_{2,L10\to Ipc}})\right) \tag{13}$$

The time constants and the normalization factor are the same as described above. The variable t_i^k represents the time at which the L10 neuron i generates

the kth spike. The total synaptic current received by Ipc neuron j is therefore a sum of all the synaptic currents from the population of L10 neurons. The expression for the synaptic current $I_{Ipc\to i}$ received by L10 neuron i has a similar form.

The external current input, $I_{e,i} = (I_0 + \eta_{e,i})H(i-160)H(240-i)$, to L10 neuron i represents the stimulus from the retinal ganglion cell. This external current input has a constant component I_0 and a noise component $\eta_{e,i}$. The Heaviside step function, H, expresses that the current to L10 neurons is non-zero between neuron #160 and #240 and zero elsewhere. The noise component, $\eta_{e,i}$, is modeled as uncorrelated white noise of standard deviation σ_e, i.e., $\left\langle \eta_{e,i}(t)\eta_{e,i'}(t') \right\rangle = 2\sigma_e^2\delta(t-t')\delta_{ii'}$.

To allow for spontaneous activity, each L10 and Ipc neuron receives an uncorrelated noise current, χ_i and χ_j, respectively. The noise currents are modeled as uncorrelated white noise, i.e. $\left\langle \chi_i(t)\chi_{i'}(t') \right\rangle = 2\sigma_{L10}^2\delta(t-t')\delta_{ii'}$ and $\left\langle \chi_j(t)\chi_{j'}(t') \right\rangle = 2\sigma_{Ipc}^2\delta(t-t')\delta_{jj'}$ of standard deviation σ_{L10} and σ_{Ipc}, respectively.

In one set of simulations, we implemented an after-depolarization to the Ipc leaky integrate-and-fire model neurons using a phenomenological description (Doiron et al. 2007). When an Ipc spike occurs, an after-depolarizing current $I_{ADP} = Ax(t)$

is evoked after a time delay τ_{ADP}. Here $x(t)$ evolves according to the set of two differential equations $\frac{dx}{dt} = y$ and $\frac{dy}{dt} = -\alpha^2 x - 2\alpha y + \alpha^2 \sum_i \delta(t - t_i - \tau_{ADP})$, where t_i is the time at which the Ipc neuron spikes, α is the inverse of the time constant of the depolarization current and A is the current amplitude. The ADP current parameters ($A = 0.7$ nA, $\tau_{ADP} = 0.5$ ms, $\alpha = 4.5$ s^{-1}) were chosen for the simulated after-depolarization to match a large recorded after-depolarization.

The source code for the model is accessible at https://senselab.med.yale.edu/ModelDB/showmodel.asp?model=120783 .

3.4 Results

3.4.1 Cellular and synaptic properties of L10 and Ipc neurons

The Ipc nucleus receives glutamatergic inputs from a subpopulation of L10 neurons with the characteristic shepherd's crook axon (Wang et al. 2006). A total of 12 neurons located in tectal layer 10 were recorded and were sufficiently labeled for unequivocal identification as shepherd's crook neurons. This type of neuron consists of an apical dendrite, several basal dendrites, and an axon originating from the apical dendrite with a characteristic U-turn before it courses towards the deep tectal layers (Fig. 3.2(a)). The average resting membrane potential was –59 ± 8 (mean ± SD, n = 12) mV, the average input resistance was 349 ± 198 MΩ, and the average membrane time constant was 105 ± 77 ms. We analyzed the cellular properties of the L10 neurons with depolarizing somatic

current injections from 0.01 to 0.2 nA. The recorded L10 neurons responded with a regular series of action potentials (Fig. 3.2(b)). The average firing rates, determined from the total number of spikes divided by the duration of the current pulse, increased approximately linearly with current amplitude (Fig. 3.2(c)). The average instantaneous onset firing rates, determined from the inverse of the first interspike intervals in response to the onset of the current pulse, were larger than the average firing rates (Fig. 3.2(c)), thus indicating some level of spike-rate adaptation.

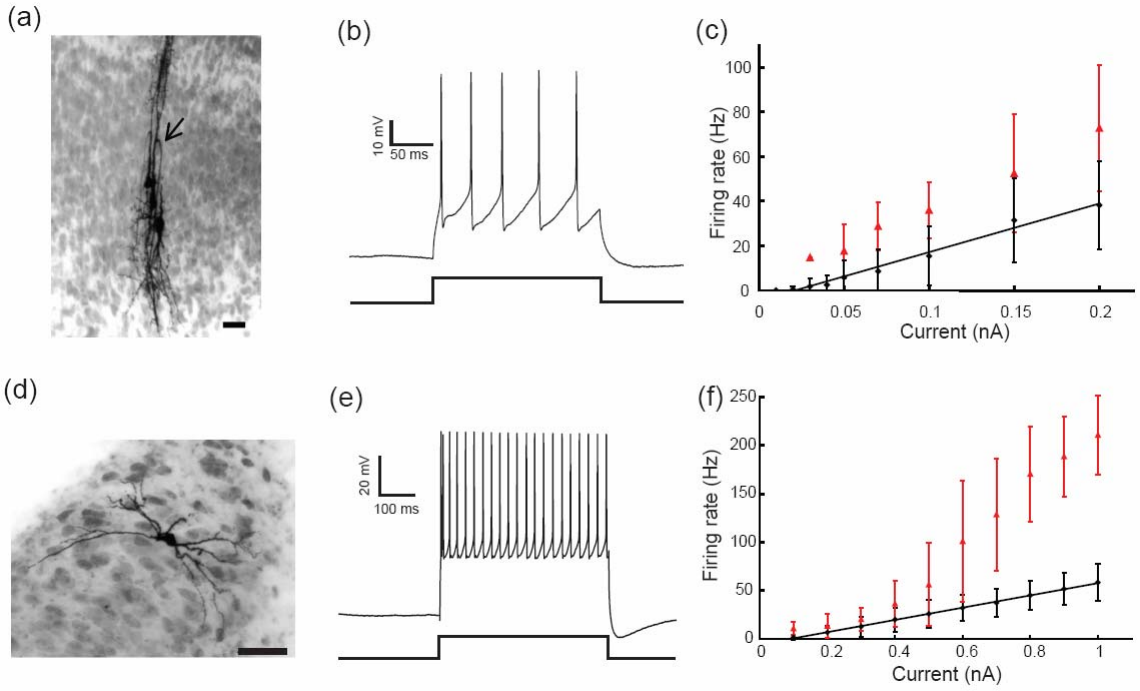

Figure 3.2 Morphological and electrophysiological properties of L10 and lpc neurons. (a) Intracellular biocytin fills of three tectal L10 neurons. The U-shaped axon (arrow head) characterizes the center neuron as a shepherd's crook neuron, which projects to the nucleus isthmi. A U-shaped axon is also visible for the left neuron. Scale bar = 20 µm. (b) Response of a

representative L10 neuron to a 0.1 nA current step. (c) Average firing rate (black diamonds) and instantaneous firing rate (the inverse of the first interspike intervals, red triangles) vs. current for the population of recorded L10 neurons. The black line represents a linear fit ($F(I) = 217.86 \times I - 4.61$ **;** $r^2 = 0.9821$**) of the firing rate,** F **, as a function of the injected current,** I **, to the measured average firing rate data points. (d) Intracellular biocytin fill in an lpc neuron (scale bar = 50 µm). (e) Response of a representative lpc neuron to a 0.5 nA current step. (f) Average firing rate (black diamonds) and instantaneous firing rate (the inverse of the first interspike intervals, red triangles) vs. current for the population of recorded lpc neurons. The black line represents a linear fit (** $F(I) = 63.427 \times I - 5.73$ **;** $r^2 = 0.9988$**) of the firing rate as a function of the injected current to the measured average firing rate data points.**

A total of 45 cells were recorded in the lpc nucleus and 27 of them were labeled sufficiently to allow for the attribution to the lpc nucleus. The filled lpc neurons were round or oval in shape and had a bipolar dendritic structure (Fig. 3.2(d)). The efferents from lpc neurons terminate in the optic tectum in “paintbrush” terminal fields in a columnar manner (Wang et al. 2006). The average resting membrane potential was –61 ± 7 mV, the input resistance was 114 ± 37 MΩ, and the average membrane time constant was 35 ± 15 ms. The recorded lpc neurons responded with a regular sequence of spikes to depolarizing current injections in the range from 0.1 to 1.0 nA injected into the soma (Fig. 3.2(e)). The average

firing rates increased approximately linearly with current amplitude (Fig. 3.2(f)). For current amplitudes above ~0.5 nA, the average instantaneous onset firing rates were larger than the average firing rates (Fig. 3.2(f)), thus indicating some level of spike-rate adaptation.

For completeness, we tested the possibility of intrinsic bursting from hyperpolarized levels, such as the T current-mediated bursting in thalamic relay neurons (McCormick and Huguenard 1992; Sherman 2001; Wang 1994; Zhan et al. 1999). We observed regular spiking in response to depolarizing current steps from hyperpolarized levels of -90 mV in L10 and Ipc neurons (Figure 3.3).

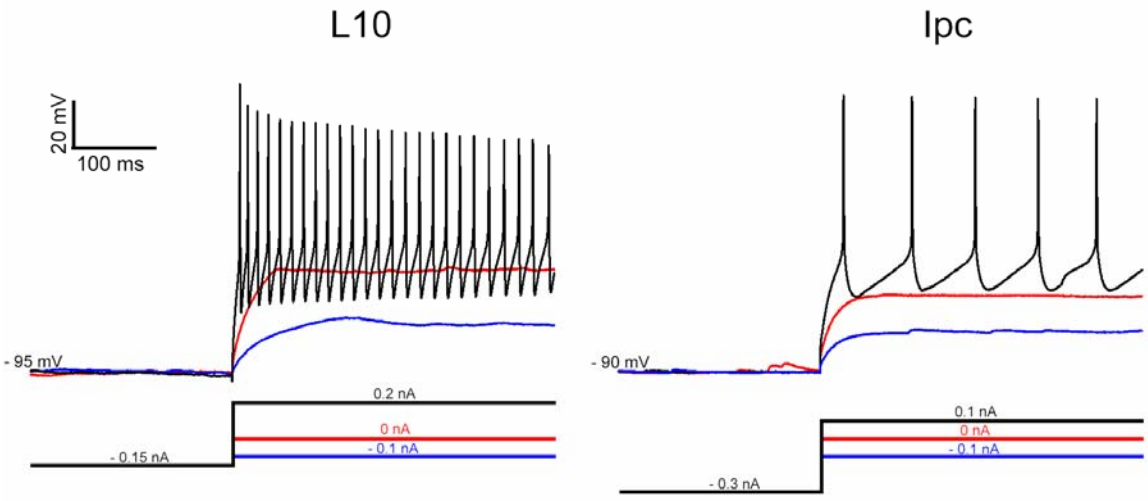

Figure 3.3 L10 and Ipc neurons respond with regular spiking to depolarizing current steps from hyperpolarized levels.

To measure the amplitude and time courses of the reciprocal synaptic connections between L10 and Ipc neurons, we positioned an extracellular stimulus electrode in either structure and recorded the response to local

extracellular electrical stimulation in the other one. Recorded Ipc neurons responded to the stimulation in tectal layer 10 with fast and strong EPSPs that could generate one to three action potentials for sufficiently strong stimulation (Fig. 3.4(a)). The synapse showed little depression (Fig. 3.4(a) inset). From seven recorded L10 → Ipc connections we estimated the values for the synaptic time constants, $\tau_{1,L10\to Ipc} = 7.2 \pm 4.7$ ms and $\tau_{2,L10\to Ipc} = 0.47 \pm 0.16$ ms, by matching the time course of model neuron synaptic responses (Sec. 3.3.2) to the recorded subthreshold EPSPs. The feedback connection was qualitatively different.

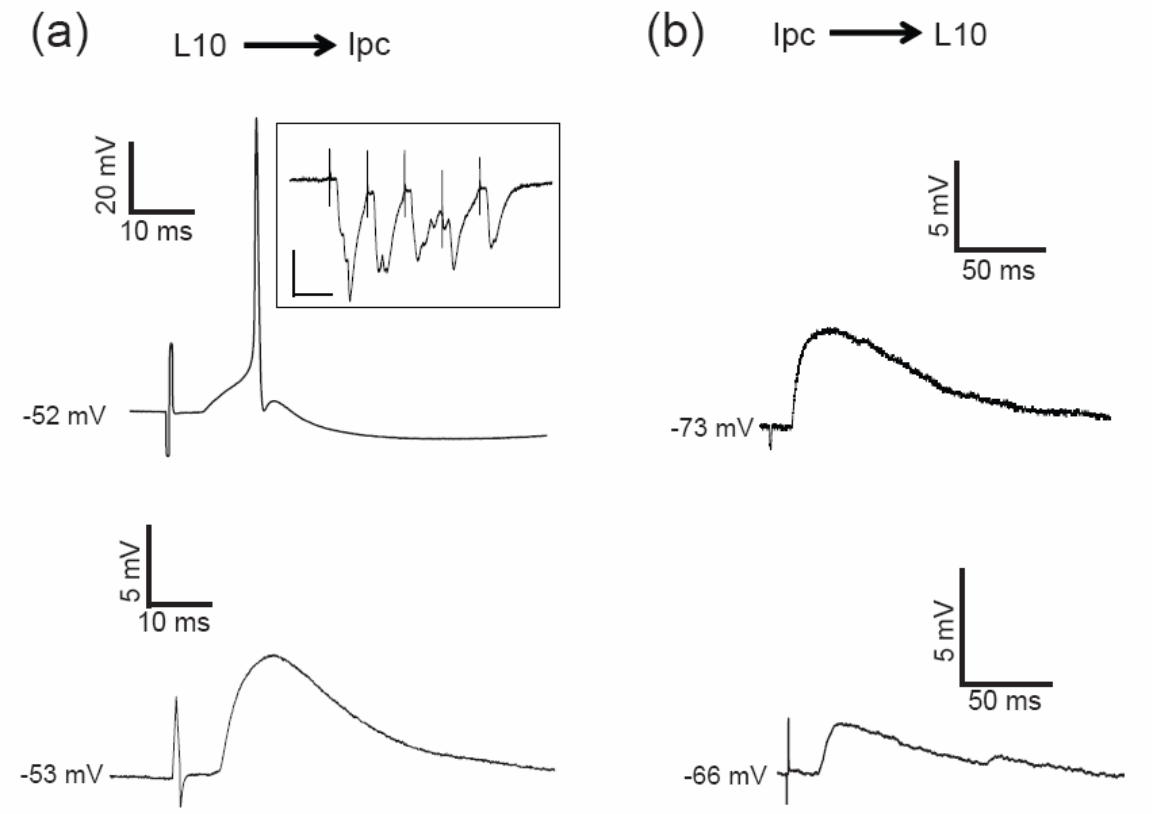

Figure 3.4 Synaptic properties of the L10 → Ipc and the Ipc → L10 connections. (a) Brief electrical stimulation with a biphasic current pulse (200 μA, 500 μs) in tectal layer 10 evoked an EPSPs plus spikes or just

EPSPs in the recorded Ipc neurons. Inset: Synaptic current recorded from an Ipc neuron in voltage clamp in response to electrical stimulation in tectal layer 10 with a train of 5 pulses of 20 ms interval. The membrane potential was held at –70 mV (scale bars = 20 ms, 200 pA). (b) Brief electrical stimulation in the Ipc nucleus evoked long-lasting EPSPs in recorded L10 neurons. Note the different scale bars in (a) and (b).

Recorded L10 neurons responded to brief electrical stimulation within the Ipc nucleus with small and long lasting EPSPs (Fig. 3.4(b)). The large L10 membrane time constant of approximately 100 ms precludes a reliable estimation of the synaptic time constant for the Ipc → L10 connection from the voltage response. Therefore, we limited the quantification of the synaptic responses to the time course of the EPSPs. The recorded EPSPs dropped to 37 % of their peak value after 87 ± 8 ms (n = 3 cells). These observations indicate that in the avian isthmotectal system the synaptic conductance change is strong and brief in the feedforward direction, L10 → Ipc, and weak and long-lasting in the feedback direction, Ipc → L10.

3.4.2 Determine experimentally constrained model parameters

For our model investigation into the mechanisms of oscillatory burst generation, we considered leaky integrate-and-fire model neurons, representing the L10 and the Ipc neuron in the avian isthmotectal system. The cellular properties of a model neuron (Eq. (1) to (5)) are specified by 8 parameters. We constrained the

parameters by comparing the simulated responses of the L10 and Ipc model neurons (Eq. (1) and (2)) to depolarizing current injections (Fig. 3.5) with the experimental results (Fig. 3.2). A L10 (Fig. 3.5(a)) or Ipc (Fig. 3.5(b)) model neuron responds with a regular spike train to an injected current pulse. Because of the spike-rate adaptation (Eq. (3) to (5)), a model neuron responds with a short inter-spike-interval (ISI) between successive spikes at the onset of a current pulse. The ISI then increases with time t after the current pulse onset and reaches a steady state within the duration of the current pulse. From the simulated spike train, we calculated the average firing rate, dividing the number of spikes by the duration of the current pulse. We repeated this procedure for different current amplitudes. We then derived the model F-I curve by fitting a linear function through the calculated average firing rates (Fig. 3.5(c), (d)).

Current (nA)	A (ms)		B (ms)		r^2	
	Exp	Theo	Exp	Theo	Exp	Theo
0.1	31.53	51.37	22.35	48.57	0.092	0.996
0.15	24.74	30.97	27.13	35.90	0.046	0.998
0.2	22.78	22.11	26.55	29.33	0.089	0.980

Table 3.2 Fitting ISI curves, $ISI(t) = A(1 - \exp(-t / B))$, to calculated ISI data points from recorded and simulated spike trains for L10 neurons. The small r^2 values for the experimental data are due to the large variations of ISI values between cells, which are also reflected in the large SD of the

measured firing rates (Fig. 3.2). The values of A, B and r^2 for 0.2 nA correspond to Fig. 3.5(e)

We also calculated the inter-spike-interval (ISI) between successive spikes in the simulated spike train and fitted an exponential function to the calculated values (Fig. 3.5(e), (f)). All 8 cellular parameter values (Table 3.1) were tuned within their experimental constraints until the model F-I curve and the ISI functions for all current amplitudes (Table 3.2 and 3.3) matched the experimental data (Fig.3.5(c) to (f)). The 8 cellular parameter values for each neuron were then kept fixed for all the simulations presented in the paper.

Current (nA)	A (ms)		B (ms)		r^2	
	Exp	Theo	Exp	Theo	Exp	Theo
1	17.47	16.68	20.47	27.48	0.36	0.97
0.9	19.36	18.73	20.85	28.56	0.25	0.97
0.8	22.62	21.37	22.04	30.15	0.25	0.96
0.7	27.22	24.84	24.21	31.94	0.24	0.96
0.6	32.44	28.68	29.55	34.68	0.15	0.95
0.5	42.67	36.82	33.81	38.30	0.089	0.95
0.4	52.22	48.49	34.09	44.42	0.027	0.91

Table 3.3 Fitting ISI curves, $ISI(t) = A(1 - \exp(-t/B))$, to calculated ISI data points from recorded and simulated spike trains for Ipc neurons. The small r^2 values for the experimental data are due to the large variations of ISI

values between cells, which are also reflected in the large SD of the measured firing rates (Fig. 32). The values of A, B and r^2 for 1 nA correspond to Fig. 3.5(f)

The model contains two types of synapses (Eq. (6) to (8)), each of which is described by 4 parameters. We adopted the synaptic reversal potential from the literature. The L10 → Ipc projection is mediated in part by glutamate receptor subtypes GluR1 or GluR2/3 (Hellmann et al. 2001) and is blocked by CNQX (Marin et al. 2007). Therefore, we assume a standard value of $E_{L10\to Ipc} = 0$ mV for the synaptic reversal potential of the glutamate receptor channel complex (Koch 1999). Ipc neurons also show a strong somatic staining for the α7 subunit of nicotinic acetylcholine receptors (nAChR) (Britto et al. 1992; Wang et al. 2006). Since the reversal potential for the nAChR channel complex of –5 mV (Koch 1999) is close to the synaptic reversal potential of 0 mV, we did not add the nAChR channel complex as a separate pathway in the model L10 → Ipc projection. Ipc neurons project with dense cholinergic axonal terminals across many tectal layers (Bagnoli et al. 1992; Hellmann et al. 2001; Medina and Reiner 1994; Sorenson et al. 1989; Wang et al. 2006). Therefore, for the Ipc →L10 projection, we assumed $E_{Ipc\to L10} = -5$ mV, which is a typical reversal potential for the nAChR channel complex (Koch 1999). The time course of the synaptic conductance change is determined by two time constants (Eq. (7)). For the Ipc model neuron with AMPA synaptic conductances (Hellmann et al. 2001; Marin et

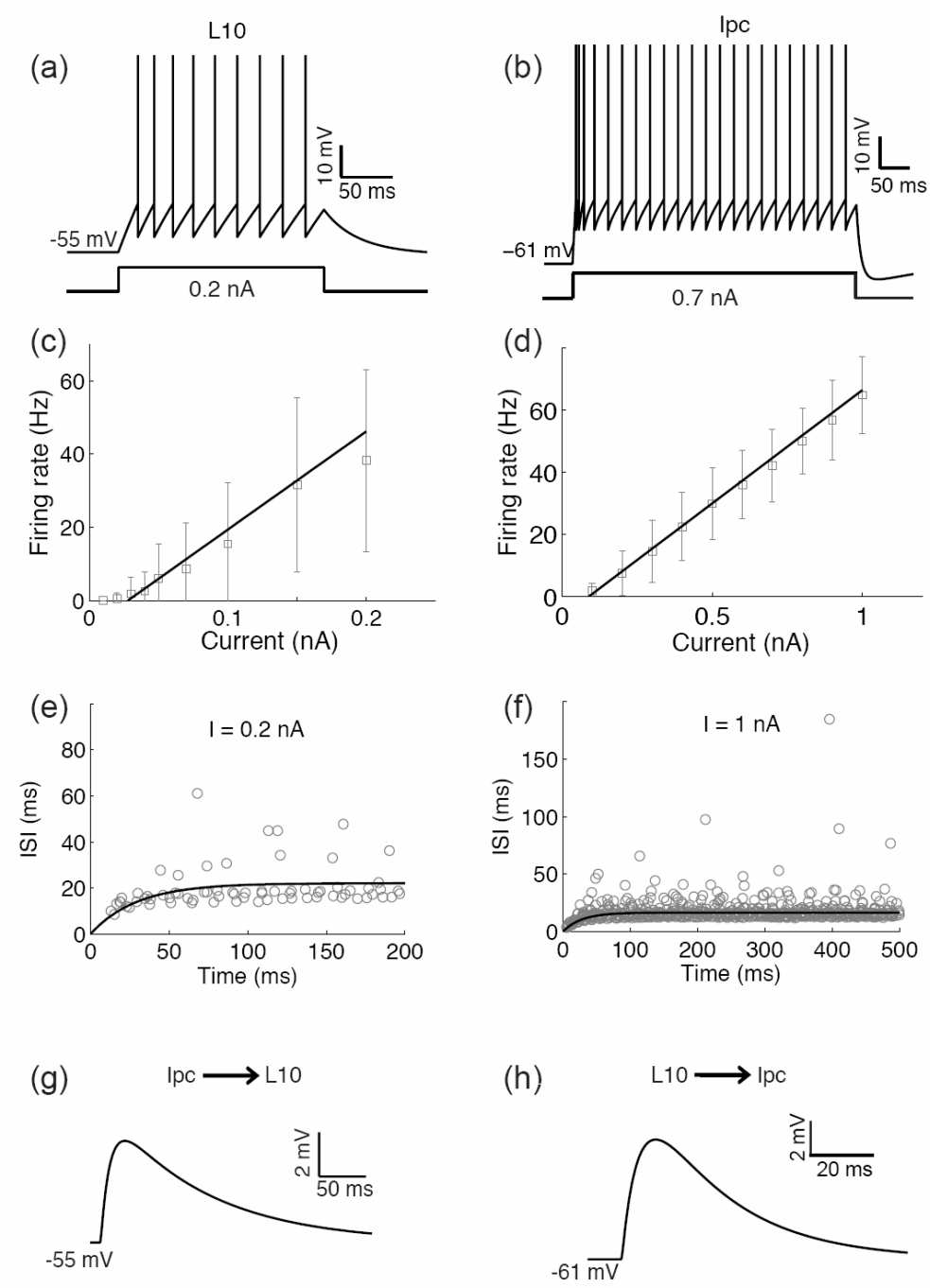

Figure 3.5 Cellular and synaptic properties of L10 and Ipc model neurons. (a) The response of the L10 model neuron to an injected current pulse of 0.2 nA amplitude. (b) The response of the Ipc model neuron to an injected current pulse of 0.7 nA amplitude. (c) The fitted F-I curve of the L10 model

neuron, $F(I) = 268.4 \times I - 7.5$ **;** $r^2 = 0.9883$ **. The experimental data (average firing rates from Fig. 3.2(c)) of the recorded real L10 neurons in response to current injections are shown for comparison (gray squares). (d) The fitted F-I curve of the Ipc model neuron,** $F(I) = 73.0 \times I - 6.5$ **;** $r^2 = 0.9992$ **. The experimental data (average firing rates from Fig. 3.2(f)) of the recorded real Ipc neurons in response to current injections are shown for comparison (gray squares). (e) The fitted ISI curve,** $ISI(t) = A(1 - \exp(-t / B))$**, of the L10 model neuron for a current injection of 0.2 nA (see Table 3.2). The experimental data from 9 recorded real L10 neurons in response to the same current injection are shown for comparison (gray circles). (f) The fitted ISI curve,** $ISI(t) = A(1 - \exp(-t / B))$ **, of the Ipc model neuron for a current injection of 1.0 nA (see Table 3.3). The experimental data from 18 recorded real Ipc neurons in response to the same current injection are shown for comparison (gray circles). (g) The synaptic response of the L10 model neuron to a single pre-synaptic action potential. The synaptic parameters were** $g_{Ipc \to L10} = 2.08$ **nS,** $\tau_{1,Ipc \to L10} = 10$ **ms,** $\tau_{2,Ipc \to L10} = 1$ **ms and the cellular parameters were the same as described in the text and Table 3.1. (h) The synaptic response of an Ipc neuron to a single pre-synaptic action potential. The synaptic parameters were** $g_{L10 \to Ipc} = 5.2$ **nS,** $\tau_{1,L10 \to Ipc} = 5.6$ **ms,** $\tau_{2,L10 \to Ipc} = 0.3$ **ms, and the cellular parameters were the same as described in the text and Table 3.1. The synaptic input caused the Ipc neuron to spike**

two times in a short period of time. The number of spikes depends on the chosen value of the maximum synaptic conductance.

al. 2007) typical rise time values, $\tau_{rise,L10\rightarrow Ipc} = 0.32$ ms, and fall time values, $\tau_{1,L10\rightarrow Ipc} = 5.6$ ms, were taken from the literature (Destexhe et al. 1994) and are consistent with the estimates based on our recordings (Fig. 3.4(a)). Matching L10 model neuron synaptic response to the recordings (Fig. 3.4(b)) led to a synaptic rise time of $\tau_{rise,Ipc\rightarrow L10} = 1.1$ ms and a fall time of $\tau_{1,Ipc\rightarrow L10} = 10$ ms. With the chosen values for the synaptic time constants, the time courses of the model synaptic responses (Fig. 3.5(g), (h)) reproduce slow EPSPs in the L10 neuron (Fig. 3.4(b)) and fast EPSPs in the Ipc neuron (Fig. 3.4(a)). Note that the maximum synaptic conductance is not constrained by the in vitro measurement. The extracellular stimulation was not limited to single-axon stimulation, rather the number of stimulated synaptic inputs depended on the chosen stimulus current and the position of the stimulus electrode relative to the presynaptic axons.

3.4.3 Mechanisms of oscillatory bursting in a reciprocally coupled pair of L10 and Ipc model neurons

Armed with the biologically plausible and experimentally constrained description of the cellular and synaptic properties of individual L10 and Ipc model neurons, we next investigated whether a reciprocally coupled pair of neurons (Fig. 3.6(a)) could generate oscillatory bursting in the Ipc model neuron in response to a plausible representation of a retinal flash of light. Since a brief flash of light

generates long-lasting evoked potentials in tectal superficial layers in vivo (Holden 1980; Letelier et al. 2000), we simulated the retinal input by a depolarizing current pulse of 0.2 nA amplitude and 350 ms duration into the L10 model neuron. For the chosen values of a strong L10 → Ipc and a weak Ipc → L10 maximum synaptic conductance, the current injection generates a regular sequence of spikes with an average firing rate of 51 Hz in the L10 model neuron (Fig. 3.6(b)). Concurrently, the Ipc model neuron responds with a short burst of spikes to every presynaptic L10 spike, thus generating oscillatory bursting in the Ipc model neuron (Fig. 3.6(c)).

Our model simulation shows that the recorded oscillatory bursts in Ipc neurons in response to a flash of light (Marin et al. 2005) can be mediated by feedforward mechanisms alone. Qualitatively, the following sequence of events causes Ipc oscillatory bursts. The retina and its tectal projection transform a brief flash of light into a long-lasting L10 synaptic current (approximated as an external current input in the model), which in turn causes the L10 neuron to spike. The L10 neuron spike generates a large depolarizing synaptic current in the Ipc neuron. The synaptic current is sufficiently strong to generate a spike and to push the membrane potential repeatedly from the reset value to the threshold for spiking, thus generating a burst of multiple spikes with ISIs of less than 4 ms. A synaptic and a cellular mechanism jointly contribute to the termination of the burst; the short duration of the synaptic current, determined by the synaptic fall time,

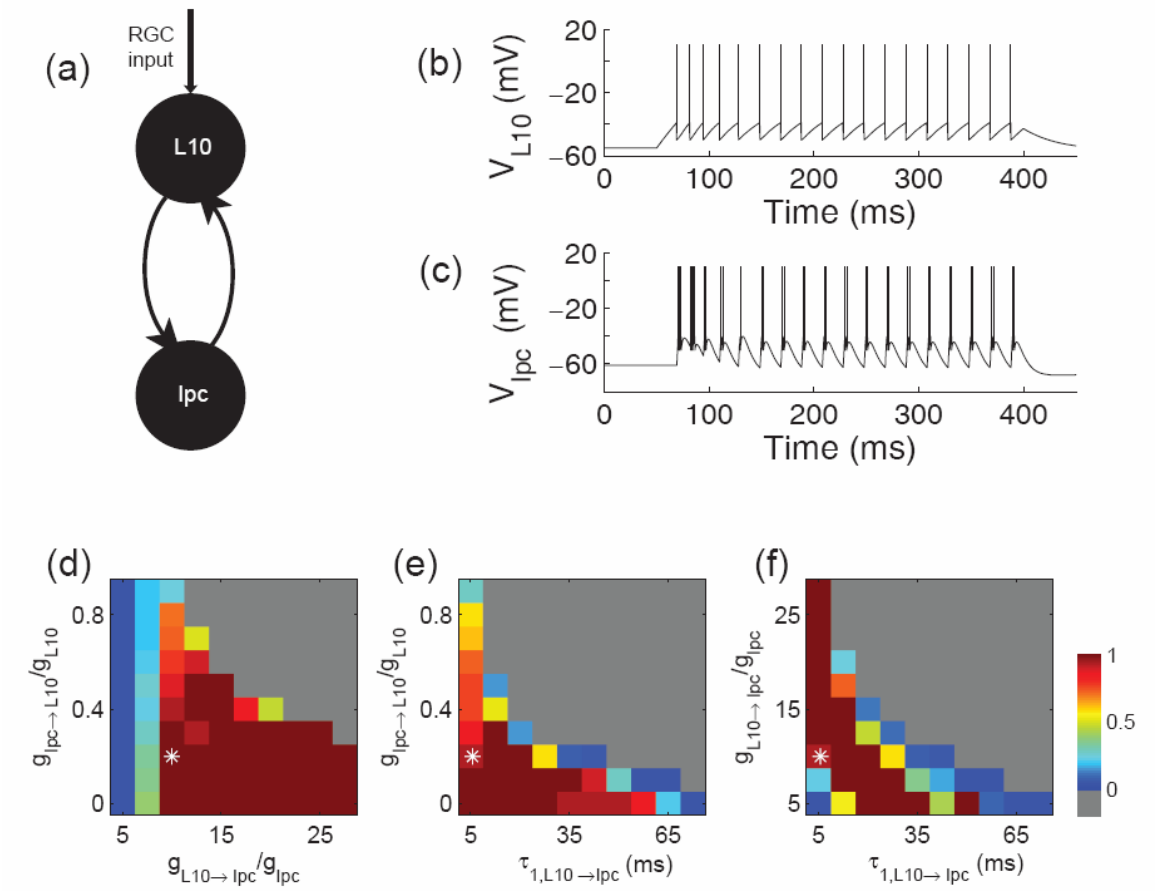

Figure 3.6 Generation of oscillatory bursting in a pair of model neurons with recurrent excitation. (a) Schematic drawing of the reciprocally coupled pair of L10 and lpc model neurons with retinal (RGC) inputs to the L10 model neuron. (b) and (c) Responses of the reciprocally coupled L10 and lpc model neurons to depolarizing current injection into the L10 model neuron. The injected current had a duration of 350 ms (starting at time = 50 ms) and an amplitude of 0.2 nA. The cellular and synaptic parameter values were chosen as described in the text and Table 3.1. The maximum synaptic conductances relative to the membrane conductance were $g_{L10\rightarrow Ipc} / g_{Ipc} = 10$ and $g_{Ipc\rightarrow L10} / g_{L10} = 0.2$. The lpc burst score (see Methods) for this trace

equals $14/15 \cong 0.93$ **. (d), (e), (f) Ipc responses for three cross sections through the 3-dimensional parameter space spanned by the maximum synaptic conductances** $g_{L10\to Ipc}/g_{Ipc}$ **and** $g_{Ipc\to L10}/g_{L10}$**, and by the feedforward synaptic fall times** $\tau_{1,L10\to Ipc}$ **. The three cross sections intersect the point (asterisk) 10, 0.2, 5.6 ms, respectively, which is also the parameter set chosen for the sample trace in (b) and (c). The Ipc responses are represented in pseudo color by the burst score. When all spikes belong to bursts the score is 1 (red), when all spikes are isolated the score is 0 (blue), when the firing rate exceeds 1000 Hz the Ipc response is classified as diverging (gray).**

$\tau_{1,L10\to Ipc}$, and the activation of the spike-rate adaptation current with every Ipc spike. The arrival of the next L10 spike, approximately 20 ms after the previous one in the displayed simulation (Fig. 3.6(b)), evokes the next burst in the Ipc neuron. Since the L10 neuron responds to the flash-induced long-lasting L10 synaptic current with a regular spike train, the Ipc neuron also responds with a regular sequence of bursts. In short, regular sequences of L10 spikes are transformed into regular sequences of Ipc bursts.

This mechanism of Ipc oscillatory burst generation is valid for the parameter area that represents a strong feedforward L10 → Ipc and a weak feedback Ipc → L10 maximum synaptic conductance (Fig. 3.6(d)). For reduced L10 → Ipc maximum synaptic conductance, only sequences of Ipc spikes rather than bursts are

generated. Interestingly, the Ipc → L10 feedback can render the L10 spike train more irregular, but is not necessary for the Ipc burst generation. Rather, for increased Ipc → L10 feedback maximum synaptic conductance, the two neurons excite each other continuously and the system transitions into a diverging regime. Another important parameter is the feedforward synaptic fall time, $\tau_{1,L10\to Ipc}$, which contributes to the termination of the burst. For increasing values of $\tau_{1,L10\to Ipc}$, significant temporal summation of EPSPs occurs in the Ipc neuron, the Ipc spike-rate adaptation is not enough to terminate the bursts, and the system transitions into a diverging regime (Fig. 3.6(e), (f)). The numerical value of $\tau_{1,L10\to Ipc}$ at which the transition to divergence occurs decreases with decreasing ISI of the L10 neuron, which of course depends on the chosen value of the retinal input; 0.2 nA for the simulation results shown in Fig. 3.6. For decreasing values of the feedforward synaptic fall time, $\tau_{1,L10\to Ipc}$, the time for burst generation is too short and only isolated Ipc spikes occur. Thus, there is a limited range of parameter values for burst generation (Fig. 3.6(f)). With decreasing $\tau_{1,L10\to Ipc}$ values the burst generation becomes more robust to the value of the feedforward maximum synaptic values, $g_{L10\to Ipc}$.

3.4.4 A population of L10 and Ipc neurons with spontaneous activity

Does the mechanism of oscillatory bursting in a reciprocally coupled pair of L10 and Ipc model neurons extend to populations of neurons? Because of the finite width of the L10→Ipc projection (Wang et al. 2006), an Ipc neuron, embedded

within the isthmotectal system, receives synaptic inputs from more than one L10 neuron. Further, because of the high level of spontaneous activity (Maczko et al. 2006; Sherk 1979), the Ipc neuron may receive uncorrelated inputs at such a high frequency that it will spike tonically, not burst. This raises an important question: Under what conditions does this simple mechanism of oscillatory burst generation break down in a population of L10 and Ipc neurons with spontaneous activity when each Ipc neuron receives inputs from many L10 neurons?

To address this question we investigated a population model of L10 and Ipc neurons with topographic reciprocal excitation (Fig. 3.7(a)) and spontaneous activity. Important model parameters are the widths, $\Delta_{L10\to Ipc}$ and $\Delta_{Ipc\to L10}$, of the projections, which determine the strength of synaptic inputs from other neurons, and the standard deviations, σ_e, σ_{L10} and σ_{Ipc} ,of the noise currents, which determine the uncorrelated activity of neurons. For a set of parameters within the bursting regime, a stimulus current step delivered to a group of L10 neurons (centered around L10 neuron #200) generates oscillatory bursts in Ipc neuron #200 (Fig. 3.7(b)). Because of the width and the strength of the L10 → Ipc projection, the spiking activity spreads to numerous Ipc neurons beyond the group of Ipc neurons that correspond to the topographic projection of the directly stimulated group of L10 neurons. In contrast, the feedback projection, Ipc → L10, of the same width, is too weak to generate L10 spikes beyond the group of directly stimulated L10 neurons. The feedback projection does however cause dispersion in the timing of L10 spikes, i.e., because of the larger summation of

excitatory feedback, L10 neurons in the center spike earlier than L10 neurons away from the center. The uncorrelated L10 activity introduces variability in the Ipc burst duration.

For narrow feedback, i.e., $\Delta_{Ipc \to L10}$ is small, the number of correlated L10 inputs to an Ipc neuron increases with increasing width, $\Delta_{L10 \to Ipc}$, of the feedforward projection and thus the Ipc neuron generates more bursts rather than isolated spikes (Fig. 3.7(c)). However, for broad feedback, L10 spike trains from neurons away from the center are less correlated. Thus, with increasing width of the feedforward projection, Ipc burst generation increases only over a narrow range then the Ipc activity diverges. In this parameter region, the adaptation current is not sufficient to prevent the system from diverging.

Because of the strong feedforward synapse, Ipc burst generation is very sensitive to uncorrelated noise in L10 neurons. The mechanism of feedforward burst generation breaks down when the value of the standard deviations, σ_e or σ_{L10}, of the noise currents approach the chosen mean value, 0.18 nA, of the stimulus current (Fig. 3.7(d) and (e)). Because of the weak feedback connection and suppressive effect of adaptation current, Ipc burst generation is much less sensitive to uncorrelated noise current into Ipc neurons (Fig. 3.7(f)).

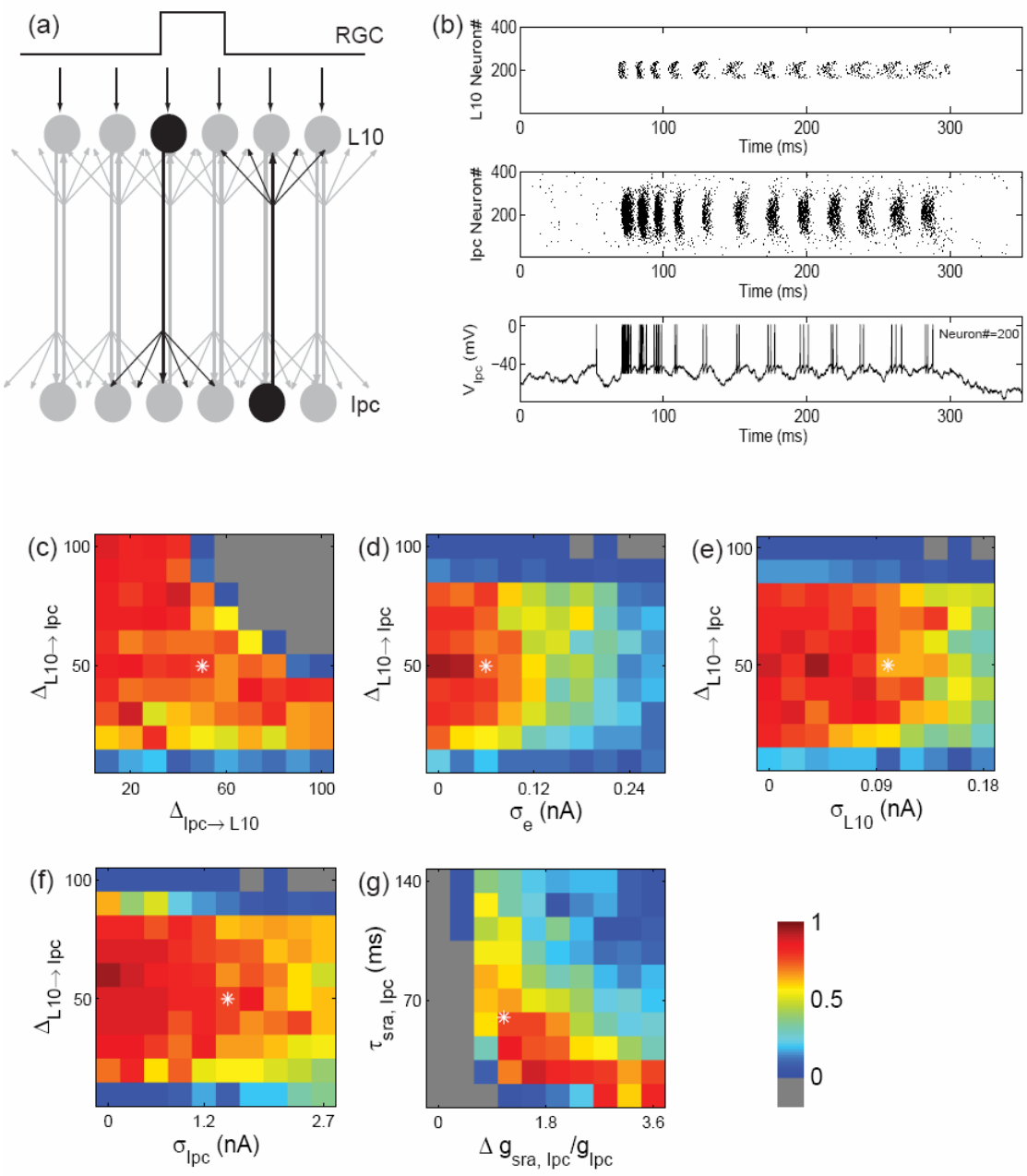

Figure 3.7 Generation of oscillatory bursts in a population model with recurrent excitation and uncorrelated noise. (a) Schematic drawing of the reciprocally coupled populations of L10 and Ipc model neurons with local RGC inputs to a small group of L10 neurons. The projections are topographic, but have a certain width as indicated by the spread of arrows.

(b) Sample L10 and Ipc population responses (raster plot of spikes) to a stimulus current step delivered to 80 neurons centered on L10 neuron #200. The concurrent voltage response of Ipc neuron #200 is shown in the bottom trace. Single neuron parameters are listed in Table 3.1. The stimulus, synaptic, and noise parameters are: $I_0 = 0.18$ **nA,** $g_{L10 \to Ipc} = 1.85$ **nS,** $g_{Ipc \to L10} = 4.69 \times 10^{-3}$ **nS,** $\Delta_{L10 \to Ipc} = 50$ **,** $\Delta_{Ipc \to L10} = 50$ **,** $\sigma_e = 0.06$ **nA,** $\sigma_{Ipc} = 1.5$ **nA,** $\sigma_{L10} = 0.1$ **nA. The stimulus current is turned on at** $t = 50$ **ms and lasts for 250 ms. (c) to (f) Ipc responses for four cross sections through the 5-dimensional parameter space spanned by the spatial width of the synaptic weight distributions** $\Delta_{L10 \to Ipc}$ **and** $\Delta_{Ipc \to L10}$ **, and the white noise standard deviations** σ_e**,** σ_{Ipc}**, and** σ_{L10}**. The four cross sections intersect the point (asterisk) 50, 50, 0.06 nA, 1.5 nA, 0.1 nA, respectively, which is also the parameter set chosen for the sample trace in (b). The Ipc responses are represented in pseudo color (see Fig. 3.6) by the "average burst score", which is the burst score (see Methods) averaged over 5 trials. (g) Ipc responses for different values of the Ipc spike-rate adaptation increment,** $\Delta g_{sra,Ipc}$ **, and the decay time constant,** $\tau_{sra,Ipc}$**. All other parameters are as in (b).**

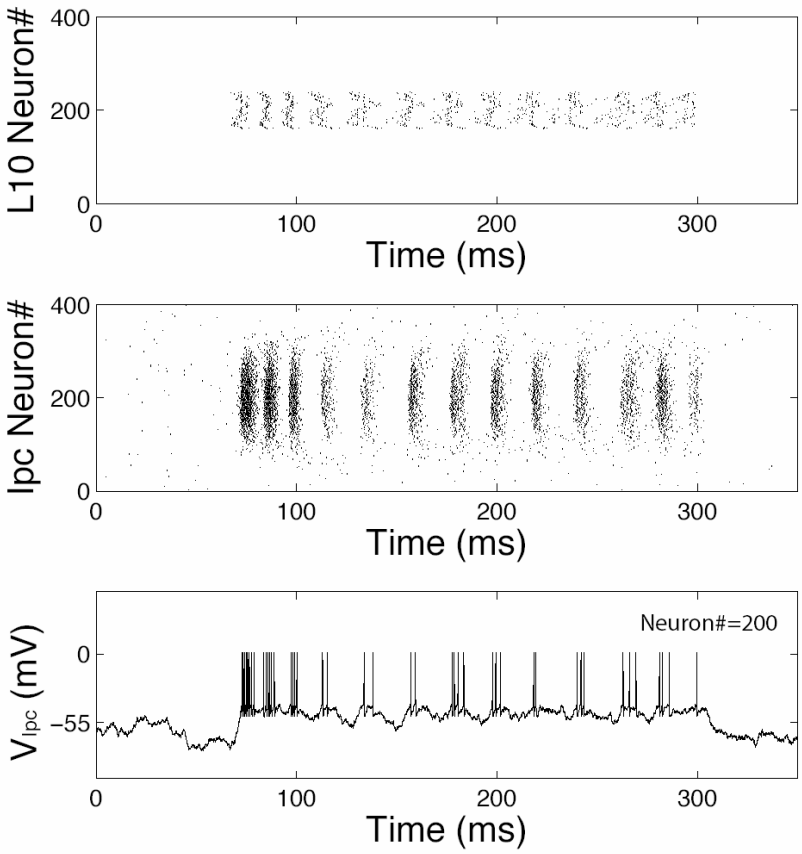

Figure 3.8 The role of noise correlation in Ipc oscillatory burst generation. Sample L10 and Ipc population responses (raster plot of spikes) to a stimulus current step delivered to 80 neurons centered on L10 neuron #200. The concurrent voltage response of Ipc neuron #200 is shown in the bottom trace. Single neuron parameters are listed in Table 3.1. The stimulus, synaptic, and most noise parameters are as in Fig. 3.7(b): $I_0 =$ **0.18 nA,** $g_{L10\to Ipc} = 1.85$ **nS,** $g_{Ipc\to L10} = 4.69\times10^{-3}$ **nS,** $\Delta_{L10\to Ipc} = 50$ **,** $\Delta_{Ipc\to L10} = 50$**,** $\sigma_{Ipc} = 1.5$ **nA,** $\sigma_{L10} = 0.1$ **nA. The stimulus current is turned on at** $t =$ **50 ms and lasts for 250 ms. Here, the noise in the input current is increased to** $\sigma_e = 0.2$ **nA and the correlation length is** $\lambda = 30$**. Note that for**

uncorrelated noise of this amplitude Ipc neurons do not burst (see Fig. 3.7(d)).

In contrast, Ipc burst generation is less sensitive to noise in L10 neurons when the noise is correlated. Because of common inputs to adjacent L10 neurons, noise correlations in the L10 input currents are likely to exist. Given the potential importance of noise correlations for burst generation and stimulus representation in sensory systems (Chacron and Bastian 2008), we investigated the role of noise correlations in the isthmotectal system. We simulated the population model with correlated noise, $\eta_{e,i}$, in the external current input, $I_{e,i} = (I_0 + \eta_{e,i})$, to the subset of L10 neurons, labeled $i = 160$ to $i = 240$. The noise correlation in the external current input to two L10 neurons, i and i', decreases with distance as described by $\langle \eta_{e,i}(t)\eta_{e,i'}(t') \rangle = 2\sigma_e^2 \exp(-|i - i'|/\lambda)\delta(t - t')$, where λ represents a correlation length (Abbott and Dayan 1999). In the limit of $\lambda \to 0$, we recover the case of uncorrelated noise, $\langle \eta_{e,i}(t)\eta_{e,i'}(t') \rangle = 2\sigma_e^2 \delta(t - t')\delta_{ii'}$. It is instructive to start the simulation with uncorrelated noise with a large standard deviation, $\sigma_e = 0.2$ nA, comparable to the value of the constant component, I_0. In this case, L10 neurons produce largely uncorrelated spike trains and Ipc neurons do not burst (burst score below 0.3; Fig. 3.7(d)). However, with increasing noise correlation, spike trains of stimulated L10 neurons become more correlated and Ipc bursting resumes. For instance, with a correlation length of $\lambda = 30$ the burst score reaches 0.9 (Figure 3.8).

The Ipc spike-rate adaptation conductance is determined by the decay time constant, $\tau_{sra,Ipc}$, and the conductance increment, $\Delta g_{sra,Ipc}$. Interestingly, the two-dimensional parameter space reveals a narrow region for Ipc burst generation (Fig. 3.7(g)). For the conductance increment decreasing from this region, the Ipc neuron activity diverges as expected, since spike-rate adaptation is the only activity-dependent regulatory mechanism in this network of reciprocal excitation. For the conductance increment increasing from this region, the Ipc neuron produces isolated spikes, rather than bursts, to synaptic inputs. Similarly, Ipc activity diverges with decreasing decay time constant and transitions to tonic spiking when the time constant increases.

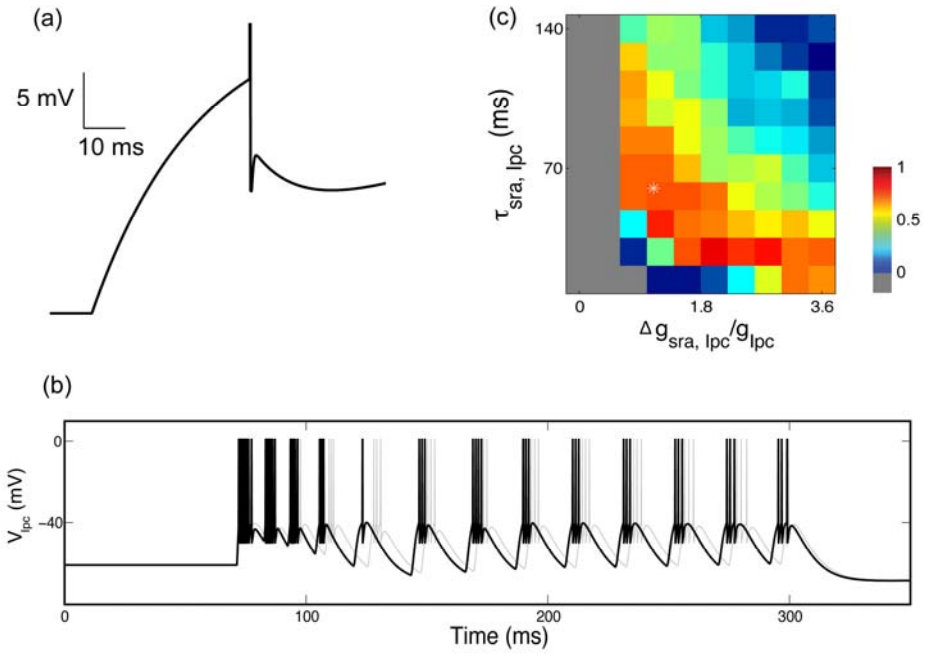

Figure 3.9 The role of the ADP for Ipc burst generation in the population model. (a) The response of a model Ipc neuron with ADP to a depolarization current injection of 0.2 nA. (b) The response of the center Ipc neuron in a population to a square shaped stimulus for model Ipc neurons with ADP

(black) and without ADP (gray). Bursts are generated in both cases, but the activity of the neuron with ADP is slightly increased. For simplicity, only the deterministic model was considered. (c) To investigate the effect of ADP further, we conducted a parameter scan in the lpc adaptation parameter space as in Fig. 3.7(g). The ADP slightly increases the region with high bursting scores.

Since some lpc recordings displayed a spike after-depolarization (ADP) and since in general ADPs can provide a mechanism for bursting (Higgs and Spain 2009), the potential role of ADPs in the case of lpc bursting was evaluated. We implemented ADPs in the lpc model neuron using a simple formalism (Doiron et al. 2007), where each lpc spike triggers a delayed depolarizing current (see Sec. 3.3.3). Simulation results with the ADP included indicate that the ADP is not necessary for lpc burst generation; however the ADP slightly enlarges the region of parameter space for burst generation (Fig. 3.9) compared to lpc model neurons without ADPs (Fig. 3.7(g)).

3.5 Discussion

We measured the cellular and synaptic properties of avian L10 and lpc neurons in vitro. We found regular spiking neurons with spike-rate adaptation. We also found reciprocal excitation, with a strong and brief feedforward L10 → lpc and a weak and long-lasting feedback lpc → L10 synaptic conductance change. Our

simulation of an experimentally constrained excitatory neural network reveals that Ipc oscillatory burst generation in response to simulated retinal inputs to L10 neurons can be mediated by regular L10 neuron spiking combined with Ipc burst responses to an L10 spike. The mechanism requires a strong and brief feedforward synaptic conductance change and is aided by Ipc spike-rate adaptation. The measured weak and long-lasting feedback synaptic conductance change is not necessary for Ipc oscillatory burst generation. Increasing components of uncorrelated Ipc inputs force a transition from oscillatory bursting to irregular tonic spiking.

3.5.1 Excitatory neural networks with adaptation

The mechanisms of oscillatory burst generation typically have in common a fast excitatory current causing a train of spikes and an activity-dependent slow inhibitory current that interrupts the spike train (Izhikevich 2007; Marder and Calabrese 1996). However, purely excitatory neural networks can produce oscillatory bursts as well (Feller 1999; O'Donovan 1999; Smith et al. 1991). In these networks, recurrent excitation mediates episodes of activity, which is terminated by activity-dependent depression or adaptation (Hansel et al. 1995; Nesse et al. 2008; Tabak et al. 2000; Tabak and Rinzel 2005; Van Vreeswijk and Hansel 2001; Vladimirski et al. 2008) rather than inhibitory synaptic currents.

Adaptation affords a rich repertoire of neurophysiological effects (Kohn 2007). Our model simulations indicate that the Ipc spike-rate adaptation current plays an

important role in terminating the burst. The oscillatory bursts in Ipc neurons are evoked by the strong projection from periodically firing L10 neurons. Without the adaptation current, the burst duration is largely determined by the synaptic fall time, $\tau_{1,L10\to Ipc}$. For increasing values of $\tau_{1,L10\to Ipc}$, a small increase in maximum synaptic conductance, $g_{L10\to Ipc}$ and $g_{Ipc\to L10}$, would push the system from bursting to diverging. In contrast, when the Ipc spike-rate adaptation current is present, it provides an activity-dependent negative feedback that terminates the bursts after a few spikes. Ipc spike-rate adaptation thus enlarges the volume for bursting in the three-dimensional parameter space (Fig. 3.6(d), (e), (f)). Two parameters, the decay time constant, $\tau_{sra,Ipc}$, and the conductance increment, $\Delta g_{sra,Ipc}$, specify the Ipc spike-rate adaptation conductance. The population model investigation reveals a narrow area for bursting in this two-dimensional parameter space (Fig. 3.7(g)).

Spike-rate adaptation is often mediated by potassium currents with slow inactivation (Brown et al. 1990; Brownstone 2006; Lewis et al. 1986; Storm 1990). In the phenomenological description chosen for our model, the parameter values for the spike-rate adaptation (Table 3.1) are experimentally constrained by the measured $F(I)$ and $ISI(t)$ curves (Fig. 3.5). The fact that the $ISI(t)$ curves for model and real neurons are well matched for all current injection values considered (Fig. 3.5(e), (f) and Table 3.2, 3.3), indicates that the leaky integrate-and-fire model provides a good approximation for the real L10 and Ipc neurons.

3.5.2 Brief feedforward synaptic conductance changes

Even with the experimentally constrained spike-rate adaptation included, oscillatory burst generation requires the synaptic fall time, $\tau_{1,L10\to Ipc}$, to be well below 100 ms (Fig. 3.6(e), (f)). With increasing synaptic fall times the excitatory synaptic potentials in the Ipc neuron sum. As a result the system activity transits into the diverging regime even for small synaptic conductances. This model result is consistent with the observation that the L10 → Ipc projection is mediated by AMPA-type glutamate receptors (Hellmann et al 2001; Marin et al. 2007) and possibly by nicotinic acetylcholine receptors (Britto et al. 1992; Wang et al. 2006); both of which have the required short synaptic fall times (Destexhe et al. 1994).

3.5.3 Neuronal noise produces variable burst durations

The consequences of neuronal noise and correlations on the integrative properties of neural systems have received increasing attention in recent years (Averbeck et al. 2006; Chance et al. 2002; Destexhe and Contreras 2006; Destexhe and Rudolph 2009; Fox et al. 2006; Wolfart et al. 2005). Ipc bursts in vivo have variable burst durations (Marin et al. 2005). Our population model provides a simple explanation. Uncorrelated L10 activities, mediated by noise currents, add variability to the Ipc burst duration (Fig. 3.7(b)). With increasing noise levels the Ipc response transitions from bursting to irregular spiking (Fig. 3.7(d), (e)). Because of the weak feedback connection and the suppressive effect of adaptation current, the mechanism of Ipc burst generation is less sensitive to noise currents into Ipc neurons (Fig. 3.7(f)).

3.5.4 The cholinergic feedback is weak

We recorded a slow and long-lasting Ipc → L10 synaptic potential change (Fig. 3.4(b)). This observation is consistent with, but does not test, the previously-discussed hypothesis that the cholinergic feedback to the optic tectum might be mediated by a paracrine mode of synaptic transmission (Gruberg et al. 1994; Sargent et al. 1989; Sereno and Ulinski 1987; Wang et al. 2006).

Our model simulations indicate that the Ipc → L10 feedback is not necessary for the Ipc oscillatory burst generation (Fig. 3.6(d)). However, these model results can not exclude the possibility that feedback may contribute to the oscillatory burst generation in vivo via mechanisms not included in the simple model. For instance, cholinergic feedback may control the excitability (Kawai et al. 2007) of RGC axons, the calcium influx into RGC axon terminals (Dudkin and Gruberg 2003) and thus synaptic transmission, or may activate GABAergic tectal circuits (Luksch and Golz 2003) with potentially inhibitory effect on L10 neurons.

Feedback in our model can affect the oscillatory burst pattern. With increasing feedback strength the L10 spike train pattern, and thus the Ipc oscillatory burst pattern, becomes more irregular. Interestingly, the related concept of spike-triggered feedback currents has previously been included in leaky integrate-and-fire models to provide more realistic model responses (Jolivet et al. 2004; Paninski et al. 2004 Pillow et al. 2005).

When the Ipc → L10 feedback increases above a critical value, the L10 and Ipc neuron excite each other continuously and the system transitions into a diverging regime (Fig. 3.6(d)). The latter observation is consistent with the 'no-strong-loops hypothesis' (Crick and Koch 1998), which states that a strong excitatory loop formed between two cortical areas would lead the system into uncontrolled oscillations (Schnitzler and Gross 2005).

Although the Ipc → L10 feedback is apparently weak and is not required for the oscillatory burst generation, cholinergic feedback is involved in tectal visual processing. For instance, cholinergic feedback enhances calcium influx into optic nerve fiber terminals in frog (Dudkin and Gruberg 2003) and inactivation of cholinergic feedback prevents visual responses in the ascending visual pathway to the nucleus rotundus in birds (Marin et al. 2007). Bursts facilitate synaptic transmission across unreliable synapses via increased transmitter release (Izhikevich et al. 2003; Lisman 1997; Sherman 2001). We expect this effect to be significant for paracrine transmission in the cholinergic feedback as well. In conclusion, delivering the cholinergic feedback via oscillatory bursting Ipc axon terminals in the tectum is likely to be of great importance for the population coding of visual information in the intricate retino-tecto-rotundal pathway (Khanbabaie et al. 2007; Luksch et al. 1998, 2001, 2004; Mahani et al. 2006; Marin et al. 2003).

3.6 References

Abbott LF, & Dayan P (1999) The effect of correlated variability on the accuracy of a population code. Neural Comput 11: 91-101.

Averbeck BB, Latham PE, & Pouget A (2006) Neural correlations, population coding and computation. Nat Rev Neurosci 7: 358-366.

Bagnoli P, Fontanesi G, Alesci R, & Erichsen J (1992) Distribution of neuopeptide Y, substance P, and choline acetyltransferase in the developing visual system of the pigeon and effects of unilateral retina removal. J Comp Neurol 318: 392-414.

Brandt SF, Pelster A, & Wessel R (2006) Variational calculation of the limit cycle and its frequency in a two-neuron model with delay. Phys Rev E 74: 036201.

Brandt SF, & Wessel R (2007) Winner-take-all selection in a neural system with delayed feedback. Biol Cybern 97: 221-228.

Brandt SF, Pelster A, & Wessel R (2007) Synchronization in a neuronal feedback loop through asymmetric temporal delays. Europhys Lett 79: 38001.

Britto LR, Keyser KT, Lindstrom JM, & Karten HJ (1992) Immunohistochemical localization of nicotinic acetylcholine receptor subunits in the mesencephalon and diencephalon of the chick (Gallus gallus). J Comp Neurol 317: 325-340.

Brown DA, Gähwiler BH, Griffith WH, & Halliwell JV (1990) Membrane currents in hippocampal neurons. Prog Brain Res 83: 141-160.

Brownstone RM (2006) Beginning at the end: repetitive firing properties in the final common pathway. Prog Neurobiol 78: 156-172.

Buzsaki G (2006) Rhythms of the brain. Oxford University Press.

Chacron MJ, Longtin A, & Maler L (2005) Delayed excitatory and inhibitory feedback shape neural information transmission. Phys Rev E 72: 051917.

Chacron MJ, & Bastian J (2008) Population coding by electrosensory neurons. J Neurophysiol 99: 1825-1835.

Chance FS, Abbott LF, & Reyes AD (2002) Gain modulation from background synaptic input. Neuron 35: 773-782.

Crick F, & Koch C (1998) Constraints on cortical and thalamic projections: the no-strong-loops hypothesis. Nature 391: 245-250.

Cook RG (2001) Avian visual cognition. Available on-line at: www.pigeon.psy.tufts.edu/avc/

Coombes S, & Bressloff PC (2005) Bursting: the genesis of rhythm in the nervous system. World Scientific Press.

Destexhe A, Mainen ZF, & Sejnowski TJ (1994) Synthesis of models for excitable membranes, synaptic transmission and neuromodulation using a common kinetic formalism. J Comp Neurosci 1: 195-230.

Destexhe A, & Contreras D (2006) Neuronal computations with stochastic network states. Science 314: 85-90.

Destexhe A, & Rudolph M (2009) Neuronal noise. Springer.

Doiron B, Chacron MJ, Maler L, Longtin A, Bastian J (2003) Inhibitory feedback required for network oscillatory responses to communication but not to prey stimuli. Nature 421: 539-543.

Doiron B, Oswald AMM, & Maler L (2007) Interval coding. II. Dendrite-dependent mechanisms. J Neurophysiol 97: 2744-2757.

Dudkin EA, & Gruberg ER (2003) Nucleus isthmi enhances calcium influx into optic nerve fiber terminals in Rana pipiens. Brain Res 969: 44-52.

Dye JC, & Karten HJ (1996) An in vitro study of retinotectal transmission in the chick: role of glutamate and GABA in evoked field potentials. Visual Neurosci13:747–758.

Feller MB (1999) Spontaneous correlated activity in developing neural circuits. Neuron 22: 653-656.

Fox MD, Snyder AZ, Zacks JM, & Raichle ME (2006) Coherent spontaneous activity accounts for trial-to-trial variability in human evoked brain responses. Nat Neurosci 9: 23-25.

Gabbiani F, Metzner W, Wessel R, & Koch C (1996) From stimulus encoding to feature extraction in weakly electric fish. Nature 384: 564-567.

Gruberg ER, Hughes TE, & Karten HJ (1994) Synaptic interrelationships between the optic tectum and ipsilateral nucleus isthmi in Rana pipiens. J Comp Neurol 339: 353-364.

Hansel D, Mato G, & Meunier C (1995) Synchrony in excitatory neural networks. Neural Comput 7: 307-337.

Hellmann B, Manns M, & Güntürkün O (2001) Nucleus isthmi, pars semilunaris as a key component of the tectofugal visual system in pigegons. J Comp Neurol 436: 153-166.

Higgs MH, & Spain WJ (2009) Conditional bursting enhances resonant firing in neocortical layer 2-3 pyramidal neurons. J Neurosci 29: 1285-1299.

Holden AL (1980) Field potentials evoked in the avian optic tectum by diffuse and punctiform luminous stimuli. Exp Brain Res 39: 427-432.

Izhikevich EM (2007) Dynamical Systems in Neuroscience: The Geometry of Excitability and Bursting. Cambridge, MA: The MIT Press.

Izhikevich EM, Desai NS, Walcott EC, & Hoppensteadt FC (2003) Bursts as a unit of neural information: selective communication via resonance. Trends Neurosci 26: 161-167.

Jolivet R, Lewis TJ, & Gerstner W (2004) Generalized integrate-and-fire models of neuronal activity approximate spike trains of a detailed model to a high degree of accuracy. J Neurophysiol 92: 959-976.

Kawai H, Lazar R, & Metherate R (2007) Nicotinic control of axon excitability regulates thalamocortical transmission. Nat Neurosci 10: 1168-1175.

Khanbabaie R, Mahani A, & Wessel R (2007) Contextual interaction of GABAergic circuitry with dynamic synapses. J Neurophysiol 97: 2802-2811.

Knudsen EI (1982) Auditory and visual maps of spaces in the optic tectum of the owl. J Neurosci 2: 1177-1194.

Koch C (1999) Biophysics of Computation: Information Processing in Single neurons. New York: Oxford University Press, p. 85-116.

Kohn A (2007) Visual adaptation: Physiology, mechanisms, and functional benefits. J Neurophysiol 97: 3155-3164.

Krahe R, & Gabbiani F (2004) Burst firing in sensory systems. Nat Rev Neurosci 5: 13-23.

Laing CR, & Longtin A (2003) Dynamics of deterministic and stochastic paired excitatory-inhibitory delayed feedback. Neural Comput 15: 2779-2822.

Lesica NA, & Stanley GB (2004) Encoding of natural scene movies by tonic and burst spikes in the lateral geniculate nucleus. J Neurosci 24: 10731-10740.

Letelier JC, Mpodozis J, Marin G, Morales D, Rozas C, Madrid C, & Velasco M (2000) Spatiotemporal profile of synaptic activation produced by the electrical and visual stimulation of retinal inputs to the optic tectum: a current source density analysis in the pigeon (Columbia livia). Eur J Neurosci 12: 47-57.

Lewis DV, Huguenard JR, Anderson WW, & Wilson WA (1986) Membrane currents underlying bursting pacemaker activity and spike frequency adaptation in invertebrates. Adv Neurol 44: 235-261.

Lisman J (1997) Bursts as a unit of neural information: making unreliable synapses reliable. Trends Neurosci, 20: 38-43.

Luksch H, Cox K, & Karten HJ (1998) Bottlebrush dendritic endings and large dendritic fields: motion-detecting neurons in the tectofugal pathway. J Comp Neurol 396:399–414.

Luksch H, Karten HJ, Kleinfeld D, & Wessel R (2001) Chattering and differential signal processing in identified motion sensitive neurons of parallel visual pathways in chick tectum. J Neurosci 21:6440– 6446.

Luksch H, & Golz S (2003) Anatomy and physiology of horizontal cells in layer 5b of the chicken optic tectum. J Chem Neuroanat 25: 185-194.

Luksch H, Khanbabaie R, & Wessel R (2004) Synaptic dynamics mediate sensitivity to motion independent of stimulus details. Nat Neurosci 7: 380-388.

Maczko KA, Knudsen PF, & Knudsen EI (2006) Auditory and visual space maps in the cholinergic nucleus isthmi pars parvocellularis in the barn owl. J Neurosci 26: 12799-12806.

Mahani AS, Khanbabaie R, Luksch H, & Wessel R (2006) Sparse spatial sampling for the computation of motion in multiple stages. Biol Cybern 94: 276-287.

Marin G, Letelier JC, Henny P, Sentis E, Farfan G, Fredes F, Pohl N, Karten H, & Mpodozis J (2003) Spatial organization of the pigeon tecto-rotundal pathway: An interdigitating topographic arrangement. J Comp Neurol 458:361-380.

Marin G, Mpdozis J, Sentis E, Ossandon T, & Letelier JC (2005) Oscillatory bursts in the optic Tectum of birds represent re-entrant signals from the nucleus isthmi pars parvocellularis. J Neurosci 25: 7081-7089.

Marin G, Salas C, Sentic E, Rojas X, Letelier JC, & Mpodozis J (2007) A cholinergic gating mechanism controlled by competitive interactions in the optic tectum of the pigeon. J Neurosci 27: 8112-8121.

Marder E, & Calabrese R (1996) Principles of rhythmic motor pattern generation. Physiol Rev 76: 687-717.

McCormick DA, & Huguenard JR (1992) A model of the electrophysiological properties of thalamocortical relay neurons. J Neurophysiol 68: 1384-1400.

Medina L, & Reiner A (1994) Distribution of choline acetyltransferase immunoreativity in the pigeon brain. J Comp Neurol 342: 497-537.

Meyer U, Shao J, Chakrabarty S, Brandt SF, Luksch H, & Wessel R (2008) Distributed delays stabilize neural feedback systems. Bioll Cybern 99: 79-87.

Milton J (1996) Dynamics of small neural populations. CRM Monograph Series.

Nesse WH, Borisyuk A, & Bressloff PC (2008) Fluctuation-driven rhythmogenesis in an excitatory neuronal network with slow adaptation. J Comput Neurosci 25: 317-333.

Neuenschwander S, & Varela FJ (1993) Visually triggered neuronal oscillations in the pigeon: an autocorrelation study of tectal activity. Eur J Neurosci 5: 870-881.

Neuenschwander S, Engel AK, Konig P, Singer W, & Varela FJ (1996) Synchronization of neuronal responses in the optic tectum of awake pigeons. Visual Neurosci 13: 575-584.

O'Donovan MJ (1999) The origin of spontaneous activity in developing networks of the vertebrate nervous system. Curr Opin Neurobiol 9: 94-104.

Oswald AM, Chacron MJ, Doiron B, Bastian J, & Maler L (2004) Parallel processing of sensory input by bursts and isolated spikes. J Neurosci 24: 4351-4362.

Paninski L, Pillow JW, & Simoncelli EP (2004) Maximum likelihood estimation of a stochastic integrate-and-fire neural encoding model. Neural Comput 16: 2533-2561.

Pillow JW, Paninski L, Uzzell VJ, Simoncelli EP, & Chichilnisky EJ (2005) Prediction and decoding of retinal ganglion cell responses with a probabilistic spiking model. J Neurosci 25: 11003-11013.

Reinagel P, Godwin D, Sherman SM, & Koch C (1999) Encoding of visual information by LGN bursts. J Neurophysiol 81: 2558-2569.

Rinzel J, & Ermentrout B (1998) Analysis of neural excitability and oscillations. In: Koch C and Segev I (Eds), Methods of neuronal modeling: From Synapses to networks, 2nd edition, pp. 252-291, Cambridge: Bradford.

Sargent PB, Pike SH, Nadel DB, & Lindstrom JM (1989) Nicotinic acetylcholine receptor-like molecules in the retina, retinotectal pathway, and optic tectum of the frog. J Neurosci 9: 565-573.

Sillito AM, & Jones HE (2002) Corticothalamic interactions in the transfer of visual information. The Philosophical Transactions of the Royal Society B 357: 1739-1752

Schnitzler A, & Gross J (2005) Normal and pathological oscillatory communication in the brain. Nat Rev Neurosci 6: 285-296.

Sereno MI, & Ulinski PS (1987) Caudal topographic nucleus isthmi and the rostral nontopographic nucleus isthmi in the turtle, Pseudemys scripta. J Comp Neurol 261: 319-346.

Sherk H (1979) A comparison of visual-response properties in cat's parabigeminal nucleus and superior colliculus. J Neurophysiol 42: 1640-1655.

Sherman SM (2001) Tonic and burst firing: dual modes of thalamocortical relay. Trends Neurosci 24: 122-126.

Smith JC, Ellenberger HH, Ballanyi K, Richter DW, & Feldman JL (1991) Pre-Bötzinger complex: A brainstem region that may generate respiratory rhythm in mammals. Science 254: 726-729.

Sorenson EM, Parkinson D, Dahl JL, & Chiappinelli VA (1989) Immunohistochemical localization of choline acetyltransferase in the chicken mesencephalon. J Comp Neurol 281: 641-657.

Storm JF (1990) Potassium currents in hippocampal pyramidal cells. Progress in Brain Res 83: 161-187.

Tabak J, Senn W, O'Donovan MJ, & Rinzel J (2000) Modeling of spontaneous activity in developing spinal cord using activity-dependent depression in an excitatory network. J Neurosci 20: 3041-3056.

Tabak J, & Rinzel J (2005) Bursting in excitatory neural networks. In: Coombes S, Bressloff PC (Eds.) Bursting: the genesis of rhythm in the nervous system. Hackensack World Scientific, pp. 273-301.

Traub RD, Bibbig A, LeBeau FEN, Buhl EH, & Whittington MA (2004) Cellular mechanisms of neuronal population oscillations in the hippocampus in vitro. Annu Rev Neurosci 27: 247-248.

Van Vreeswijk C, & Hansel D (2001) Patterns of synchrony in neural networks with spike adaptation. Neural Comput 13: 959-992.

Vladimirski BB, Tabak J, O'Donovan MJ, & Rinzel J (2008) Episodic activity in a heterogeneous excitatory network, from spiking neurons to mean field. Jf Comput Neurosci 25: 39-63.

Wang XJ (1994) Multiple dynamic modes of thalamic relay neurons: rhythmic bursting and intermittent phase-locking. Neuroscience 59: 21-31.

Wang SR (2003) The nucleus isthmi and dual modulation of the receptive field of tectal neurons in non-mammals. Brain Res Rev 41: 13-25.

Wang Y, Major DE, & Karten HJ (2004) Morphology and connections of nucleus isthmi pars magnocellularis in chicks (gallus gallus). J Comp Neurol 469: 275-297.

Wang Y, Luksch H, Brecha NC, & Karten HJ (2006) Columnar projections from the cholinergic nucleus isthmi to the optic tectum in chicks (gallus gallus): a possible substrate for synchronizing tectal channels. J Comp Neurol 494: 7-35.

Wang XJ, & Rinzel J (2003) Oscillatory and bursting properties of neurons. In: Arbib MA (ed) Handbook of brain theory and neural networks. MIT Press, pp. 835-840.

Wolfart J, Debay D, LeMasson G, Destexhe A, & Bal T (2005) Synaptic background activity controls spike transfer from thalamus to cortex. Nat Neurosci 8: 1760-1767.

Zhan XJ, Cox C, Rinzel J, & Sherman SM (1999) Current clamp and modeling studies of low threshold calcium spikes in cells of the cat's lateral geniculate nucleus. J Neurophysiol 81: 2360-2373.

Chapter 4

DISTRIBUTED DELAYS STABILIZE NEURAL FEEDBACK SYSTEMS

4.1 Abstract

We consider the effect of distributed delays in neural feedback systems. The avian optic tectum is reciprocally connected with the isthmic nuclei. Extracellular stimulation combined with intracellular recordings reveal a range of signal delays from 3 to 9 ms between isthmotectal elements. This observation together with prior mathematical analysis concerning the influence of a delay distribution on system dynamics raises the question whether a broad delay distribution can impact the dynamics of neural feedback loops. For a system of reciprocally connected model neurons, we found that distributed delays enhance system stability in the following sense. With increased distribution of delays, the system converges faster to a fixed point and converges slower toward a limit cycle. Further, the introduction of distributed delays leads to an increased range of the average delay value for which the system's equilibrium point is stable. The system dynamics are determined almost exclusively by the mean and the variance of the delay distribution and show only little dependence on the particular shape of the distribution.

4.2 Introduction

The signal flow in the brain is not just feedforward; rather, feedback dominates most neural pathways (Shepherd 2003). Often pairs of reciprocally connected neurons are spatially separate by several millimeters. For instance, the primate corticothalamic feedback loop extends over a distance of approximately 100 mm. Thus for a typical action potential speed of 1 mm/ms we expect a signal delay of 100 ms. When signal delays are larger than the neural response time, complex loop dynamics emerge (Foss et al. 1996, 1997; Foss and Milton 2000).

For reciprocally connected *populations* of neurons, large delays can introduce another dimension, namely the *distribution* of delay times. Such a distribution could be an epiphenomenon in the evolution of larger brains, or it could be of adaptive significance. Work from applied mathematics states an influence of the distribution of delay times on system dynamics (Cooke et al. 1982; Gopalsamy et al. 1998; Bernard et al. 2001; Eurich et al. 2002; Liao et al. 2004; Atay 2003; Thiel et al. 2003; Zhao 2003; Eurich et al. 2005). Intrigued by the latter possibility, we asked two questions: What is the distribution of delay times in an experimentally accessible neural feedback system? What is the impact of distributed delays on a mathematically tractable neural model feedback system?

We measured the distribution of delay times in the isthmotectal feedback system of birds (Luksch 2003; Wang 2003) (Fig. 4.1a). In our experiments, the distribution of delays did not arise from trial-to-trial variability at one recording site,

but rather from the fact that different recording sites yielded different values for the delays between isthmotectal elements.

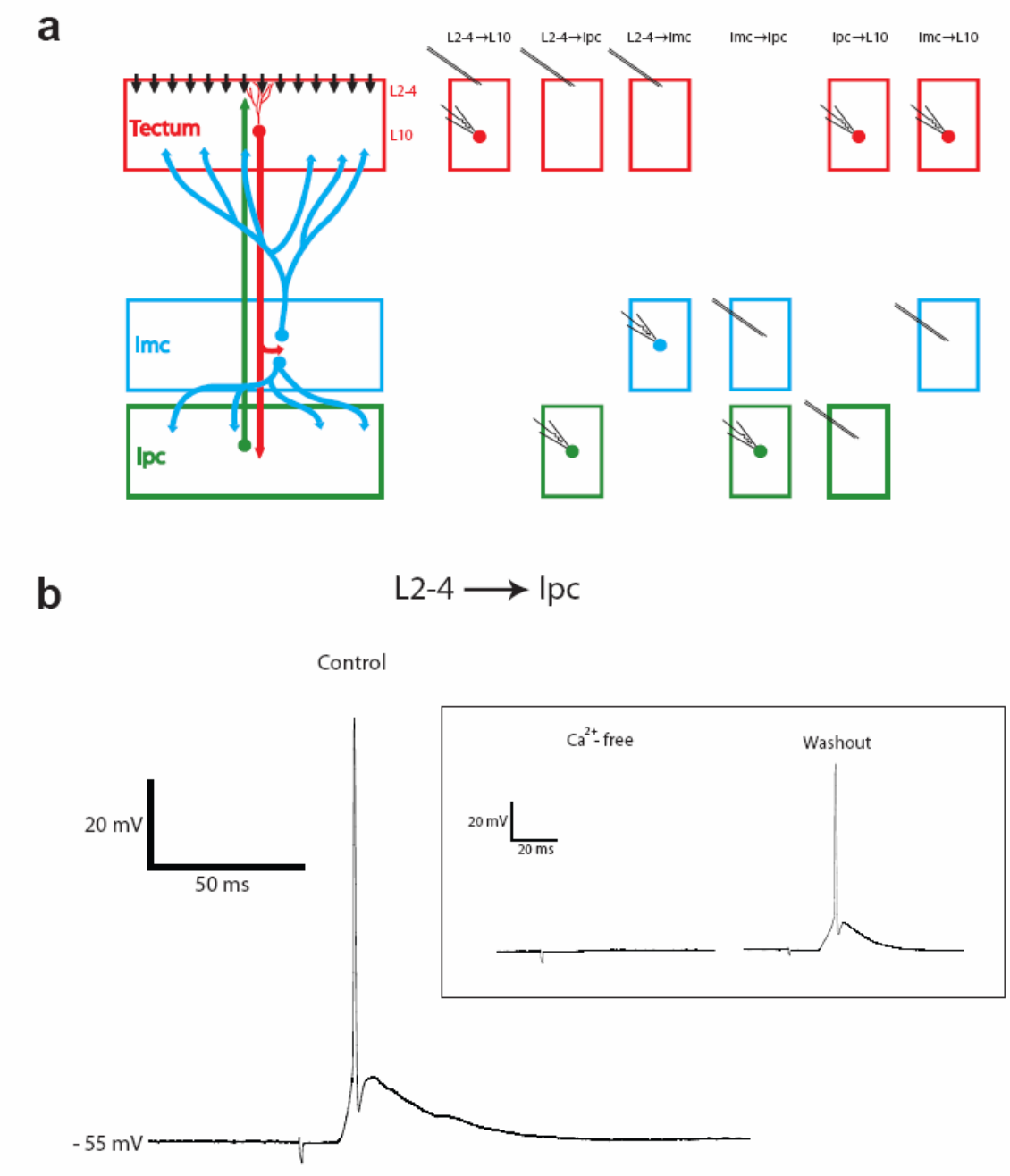

Figure 4.1 Schematic of the isthmotectal circuitry and representative response to electrical stimulation. a Schematic of the isthmotectal circuitry. Retinal ganglion cell (RGC) axons (black arrows) enter in upper tectal

layers. A subpopulation of tectal L10 neurons (red) projects to Imc and Ipc. The Imc nucleus consists of two populations of neurons (blue); one projecting broadly back to lower tectal layers and one projecting broadly to the Ipc nucleus. Ipc neurons (green) project back to the tectum with axons reaching into upper tectal layers. The six smaller columns indicate the positions of the stimulating and recording electrodes for the six experimental paradigms. b Intracellular recording from an Ipc neuron in response to electrical stimulation in tectal L2-4. Inset: The Ipc neuron does not respond in Ca^{2+}-free saline, thus excluding the possibility of antidromic Ipc axon stimulation in L2-4.

The avian isthmic nuclei (parabigeminal nucleus in mammals) receive a topographically organized projection from the tectum (superior colliculus in mammals), to which they project back and have been conjectured to mediate spatiotemporal attentional mechanisms (Wang 2003; Marín et al. 2005; Gruberg et al. 2006; Maczko et al. 2006; Marin et al. 2007). In models of visual attention, the stimulus is encoded in a "saliency map" that topographically represents the conspicuity of the stimulus over the visual scene. The most salient location is then chosen by a "winner-take all" (WTA) network, i.e., by a neurally implemented maximum detector (Koch and Ullman 1985; Sereno and Ulinski 1987; Wang and Frost 1991).

The isthmic nuclei in birds consist of three substructures: pars parvocellularis (Ipc), pars magnocellularis (Imc), and pars semilunaris (SLu) that are spatially separated from the tectum (Wang et al. 2004, 2006). In response to visual stimulation, the Ipc neurons undergo a transition from quiescence to rhythmic firing (Marin et al. 2005, 2007). Delays can drive a neural feedback loop over a stability boundary resulting in oscillatory behavior (Babcock and Westervelt 1987; Marcus and Westervelt 1989; Laing and Longtin 2003; Brandt et al. 2006a, 2007a, 2007b). To elucidate the impact of a delay *distribution* on the system dynamics, we investigated, through numerical simulations and mathematical analysis, a model of reciprocally coupled neurons with distributed delays.

4.3 Measured distribution of delays

To measure the signal delays between pairs of isthmotectal elements, we obtained intracellular whole-cell recordings from identified neurons in a midbrain slice preparation and stimulated groups of presynaptic neurons or axons with brief electrical pulses delivered extracellularly (Fig. 4.1b). Neurons were identified by their location within the midbrain slice preparation and for a subset of recorded neurons we obtained additional morphological identification via intracellular fills (Wang et al. 2004, 2006).

A subpopulation of tectal layer 10 (L10) neurons projects to both the ipsilateral Ipc and Imc in a topographic fashion (Ramon y Cajal 1911; Hunt and Künzle 1976; Hunt et al. 1977; Woodson et al. 1991; Wang et al. 2004, 2006). Their

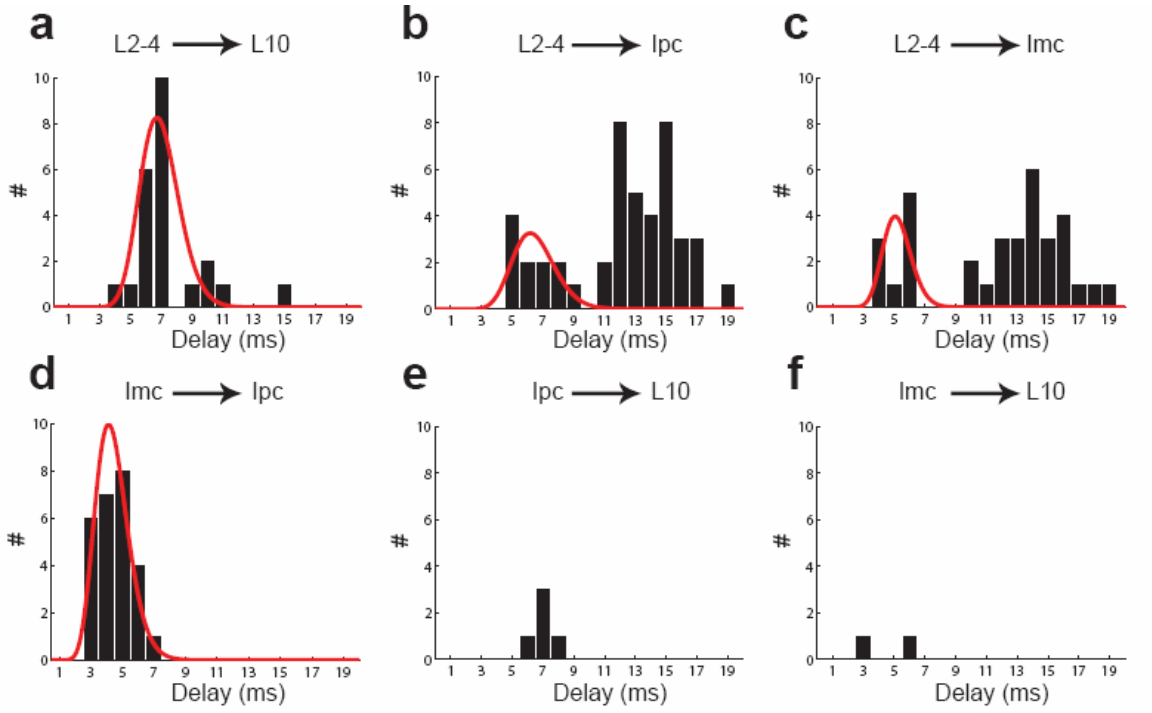

Figure 4.2 Measured distribution of signal delays between isthmotectal elements and plot of the corresponding gamma distribution (red curves in a to d) with the same mean and standard deviation. a L2-4 to L10. b L2-4 to lpc. c L2-4 to lmc. d lmc to lpc. e lpc to L10. f lmc to L10. In all cases, the histogram distribution represents the number (#) of neurons with that mean delay, derived from multiple trials for each neuron.

apical dendrite courses straight up to layer 2 with few ramifications and basal dendrites reach down to the border of layer 13. Retinal axon terminals overlap with the apical dendrite in tectal layers 2 to 7 (Domesick and Morest 1977; Sebesteny et al. 2002). We placed a stimulus electrode in layer 2 to 4 (L2-4) and recorded from L10 neurons with whole-cell recordings in response to L2-4 stimulation. The delays from the beginning of the stimulus pulse to the onset of

the L10 response ranged from 4 to 15 ms with a mean delay of 6.9 ms and a standard deviation (SD) of 1.3 ms (n = 15 cells) and a coefficient of variation (CV) of 0.19 (Fig. 4.2a). Tectal L10 neurons are a heterogeneous population (Wang et al. 2006). Therefore, only filled L10 neurons with axons originating from the dendrite in the characteristic “shepherd’s crook” shape were included in this analysis. Since L10 neuron dendrites can reach up to L2, the possibility of unwanted direct electrical, rather than synaptic, stimulation of L10 neuron dendritic endings arises. Direct electrical stimulation caused response delays less than 1 ms (data not shown). Synaptic stimulation caused response delays larger than 3 ms (Fig. 4.2a). Thus, cases of direct electrical stimulation were immediately distinguishable from synaptic stimulation and were not included in the data pool. In addition, at the end of a recording session, we evaluated the nature of stimulation by blocking chemical synaptic transmission via the block of Ca-channels by replacing Ca^{2+} in the saline with Mg^{2+}.

We measured signal delays between optic tectum and individual Ipc neurons via retinal ganglion cell (RGC) axon stimulation or L10 neuron dendrite stimulation, with a stimulus electrode placed in tectal L2-4. In the first case, the group of stimulated RGC axons stimulates a population of L10 neurons, which in turn stimulates a large number of Ipc neurons. In the second case, L10 neurons are stimulated directly. This stimulus paradigm provided a high chance of recording from an Ipc neuron that received tectal synaptic inputs. The delays from the beginning of the stimulus pulse to the onset of the Ipc neuron response ranged

from 5 to 19 ms (n = 17 cells) (Fig. 4.2b). As expected from the stimulus paradigm, the distribution of delays is bimodal. We suspect that the first bump (5 to 9 ms range) is dominated by direct L10 dendrite stimulation (mono-synaptic pathway L10-Ipc). The second bump (11 to 19 ms range) is likely to be dominated by RGC axon stimulation, which initiates the bi-synaptic pathway RGC-L10-Ipc. In addition, we can not rule out that the bi-synaptic pathway L10-Imc-Ipc can have contributed to the second bump. From the first bump in the histogram we estimate a mean delay of 6.5 ms and a SD of 1.4 ms (CV = 0.22) for the mono-synaptic pathway L10-Ipc. Since Ipc neuron axons can reach up to L2 (Wang et al. 2006), the possibility of unwanted direct electrical stimulation of Ipc axons arises. At the end of a recording session, we evaluated the nature of stimulation by blocking chemical synaptic transmission via replacing Ca^{2+} in the saline with Mg^{2+} (Fig. 4.1b, inset).

Using a stimulus paradigm similar to the one described above, we measured signal delays between L10 and individual Imc neurons. We placed a stimulus electrode in L2-4 for stimulation of RGC axons or L10 neuron dendrites and recorded from Imc neurons with whole-cell recordings in response to L2-4 stimulation. The signal delays ranged from 4 to 19 ms (n = 17 cells) and the distribution was bimodal (Fig. 4.2c). As described above, the first bump is likely to be dominated by the mono-synaptic pathway (L10-Imc), whereas the second bump is likely to be dominated by the bi-synaptic pathway (RGC-L10-Imc). The first bump in the histogram yielded a mean delay of 5.2 ms and a SD of 0.9 ms

(CV = 0.17). Since Imc axons terminate in tectal layers 10 to 13 (Wang et al. 2004), the possibility of direct Imc axon stimulation via stimulus electrodes in L2-4 does not arise.

The Imc nucleus consists of two cell types, one of which projects to the Ipc nucleus with a broad and dense projection of axonal arbors (Tömböl et al. 1995; Tömböl and Nemeth 1998; Wang et al. 2004). We positioned a stimulus electrode in the Imc nucleus and recorded from Ipc neurons with whole-cell recordings in response to Imc stimulation. The signal delays ranged from 3 to 7 ms with a mean delay of 3.9 ms and a SD of 1.1 ms (CV = 0.28, n = 26 cells, Fig. 4.2d). Care had to be taken about the interpretation of the Imc stimulation experiments. The stimulus electrode in the Imc nucleus stimulates 4 elements: L10 neuron axons, Ipc neuron axons passing through the Imc nucleus, and two populations of Imc neurons; one projecting to tectum and the other projecting to Ipc. To select the Imc to Ipc synaptic connection, we stimulated in an area of the Imc nucleus that did *not* correspond to the topographic location of the recorded Ipc neuron, thus avoiding both antidromic stimulation of the axon from the recorded Ipc neuron as well as avoiding orthodromic stimulation of the L10 axons passing through the Imc nucleus on their way to the same location in the Ipc nucleus. At the end of a recording session, we applied bicuculline to verify that the synaptic inputs to the recorded Ipc neuron were indeed from the stimulated GABAergic Imc neurons. The responses disappeared when 100 µM bicuculline was added to the bath (data not shown) thus (i) indicating that the responses

were of synaptic origin (rather than antidromic Ipc or L10 axon stimulation) and (ii) confirming that GABA is the transmitter as had been suggested by anatomical studies (Wang et al. 2004).

The Ipc nucleus has topographical reciprocal connections with the tectum (Hunt and Künzle 1976; Hunt et al. 1977; Güntürkün and Remy 1990; Hellmann et al. 2001; Wang et al. 2006). The efferents from Ipc have large calibre axons and terminate in a columnar manner ranging from layers 2 to 12 (Ramon y Cajal 1911; Hunt and Künzle 1976; Hunt et al. 1977; Tömböl et al. 1995; Tömböl and Nemeth 1998; Wang et al. 2006). We applied local extracellular electrical stimulation of a group of Ipc neurons with a stimulus electrode placed in the Ipc nucleus. Such extracellular electrical stimulation also stimulates L10 axons antidromically. The fast L10 neuron antidromic responses were distinguishable from the much slower and long-lasting synaptic responses. The additional direct activation of Imc axons in the Ipc nucleus does not interfere with this experiment, since the population of Imc neurons projecting to the Ipc nucleus is different from the population of Imc neurons projecting to the tectum. The yield for finding Ipc to L10 synaptic responses turned out to be very low. For the few cases we found, the delays ranged from 6 to 8 ms (n = 5 cells) (Fig. 4.2e).

The projection from individual Imc neurons to tectal layers 10 to 13 is broad and sparse (Wang et al. 2004). We positioned a stimulus electrode in the Imc nucleus and recorded from L10 neurons with whole-cell recordings in response to Imc

stimulation. The yield for finding Imc to L10 synaptic responses turned out to be very low. For the two connected pairs we found, the signal delays were 3 and 6 ms (n = 2 cells) (Fig. 4.2f). The low yield and the interpretation of these experiments require some explanation. As mentioned above, a stimulus electrode in the Imc nucleus will stimulate 4 elements. To select the Imc to L10 synaptic connection, we stimulated in an area of the Imc nucleus that did not correspond to the topographic location of the recorded L10 neuron, thus avoiding both antidromic stimulation of the axon from the recorded L10 neuron as well as avoiding orthodromic stimulation of the Ipc axons passing through the Imc nucleus on their way to the same location of the tectum. At the end of a recording session, we applied bicuculline to verify that the synaptic inputs to the recorded L10 neuron were indeed from the stimulated GABAergic Imc neurons. For the two neurons, the responses disappeared when 100 μM bicuculline was added to the bath (data not shown) thus indicating that the responses were of synaptic origin; rather than antidromic L10 or orthodromic Ipc axon stimulation.

In summary, these data show that the signal delays between isthmotectal elements are distributed ranging from 3 to 9 ms with the CVs of the distributions ranging from 0.19 to 0.28.

4.4 Distributed delays and the dynamics of neural feedback systems

What is the impact of distributed delays on a mathematically tractable neural model feedback system? To interpret the potential impact of the measured distribution of delays on the dynamics of neural feedback systems, we investigated a model system of two coupled Hopfield neurons (Hopfield 1984; Babcock and Westervelt 1987; Marcus and Westervelt 1989; Brandt et al. 2006a; 2007a), described by the first-order delay differential equations

$$\frac{du_1(t)}{dt} = -u_1(t) + a_1 \tanh[u_2(t-\tau_2)] \tag{1}$$

$$\frac{du_2(t)}{dt} = -u_2(t) + a_2 \tanh[u_1(t-\tau_1)] \tag{2}$$

Here $u_1(t)$ and $u_2(t)$ denote the voltages of the model neurons and τ_1 and τ_2 are the temporal delays, while a_1 and a_2 describe the coupling strength between the two neurons. Furthermore, we assume that the dynamics of both neurons are governed by the same characteristic time constant which we set to one. Time is thus dimensionless in our model, and translation to real time can be achieved by multiplying the dimensionless time variable with the characteristic time constant of the system. The system of delay differential equations has a trivial stationary point at the origin, $u_1 = u_2 = 0$ (Fig. 4.3a). The regulation of neuronal activity in the isthmotectal system involves the transmitters Glutamate and GABA (Wang et al. 2004, 2006). Therefore, excitatory-inhibitory interactions are likely to play an important role in the feedback loop. We are thus especially interested in the case where the coupling strengths a_1 and a_2 are of opposite sign. For $a_1 a_2 \leq -1$, the fixed point at the origin is asymptotically stable as long as the mean of the time

delays $(\tau_1 + \tau_2)/2$ does not exceed a critical value τ_0 (Babcock and Westervelt 1987; Wei and Ruan 1999; Brandt et al. 2006a):

$$\frac{\tau_1 + \tau_2}{2} < \tau_0 = \frac{1}{2\sqrt{|a_1 a_2| - 1}} [\sin^{-1}(-\frac{2\sqrt{|a_1 a_2| - 1}}{a_1 a_2})] \quad (3)$$

The critical value τ_0 is determined by combinations of the product of the couplings alone (Eq. (3)). For couplings of opposite signs (e.g. $a_1 a_2 \leq -1$) and when the delays are increased, the origin becomes unstable and a limit cycle emerges via a supercritical Hopf bifurcation at $(\tau_1 + \tau_2)/2 = \tau_0$ (Fig. 4.3b). The critical value, τ_0 , decreases with decreasing value of the product of the couplings $a_1 a_2$ below –1. In other words, oscillations can be achieved by either increasing the delays or by increasing the absolute value of the coupling strengths of opposite signs.

For a distribution of delays we replace the coupling term in (Eq. (1), (2)) with a weighted sum over similar terms but with different delays

$$\frac{du_1(t)}{dt} = -u_1(t) + a_1 \int_0^\infty d\tau \xi(\tau) \tanh[u_2(t-\tau)] \quad (4)$$

$$\frac{du_2(t)}{dt} = -u_2(t) + a_2 \int_0^\infty d\tau \xi(\tau) \tanh[u_1(t-\tau)] \quad (5)$$

The delay kernel $\xi(\tau)$ is normalized to satisfy $\int_0^\infty d\tau \xi(\tau) = 1$. For simplicity, we chose the delay kernels to be identical for both legs of the loop. We chose the delay kernel to be a gamma distribution,

$$\xi(\tau) = \frac{(T/v)^{T^2/v}}{\Gamma(T^2/v)} \tau^{T^2/v-1} e^{-T\tau/v} \tag{6}$$

where T is the mean delay, v is the variance of the gamma distribution, and the gamma function is defined as $\Gamma(x) = \int_0^\infty t^{x-1} e^{-t} dt$. The gamma distribution was chosen because it has the biologically plausible feature to vanish for delays approaching 0 (Fig. 4.3c). For the coupling strength we chose $a_1 = -2$ and $a_2 = 1$ for all simulations. Other combinations of coupling strengths lead to equivalent results, as long as the product $a_1 a_2$ is smaller than -1.

The parameters to vary are the mean delay, T, and the variance, v, of the gamma distribution. As these parameters are changed, the fixed point at the origin changes from a stable fixed point to an unstable fixed point surrounded by a stable limit cycle and vice-versa (Hopf bifurcation). This transition takes place when the roots, λ, of the characteristic equation for the system (Eq. (4), (5))

$$\lambda^2 + 2\lambda + 1 - a_1 a_2 \left(1 + \frac{\lambda v}{T}\right)^{-\frac{2T^2}{v}} = 0 \tag{7}$$

are purely imaginary. The characteristic equation is obtained by demanding that the solution to Eq. (4) and, (5) behaves as $u_1 = Ae^{\lambda t}$, $u_2 = Be^{\lambda t}$ near the fixed-point. Substituting $\lambda = i\omega$, where ω is real, we have

$$-\omega^2 + 2i\omega + 1 - a_1 a_2 \left(1 + \frac{i\omega v}{T}\right)^{-\frac{2T^2}{v}} = 0 \tag{8}$$

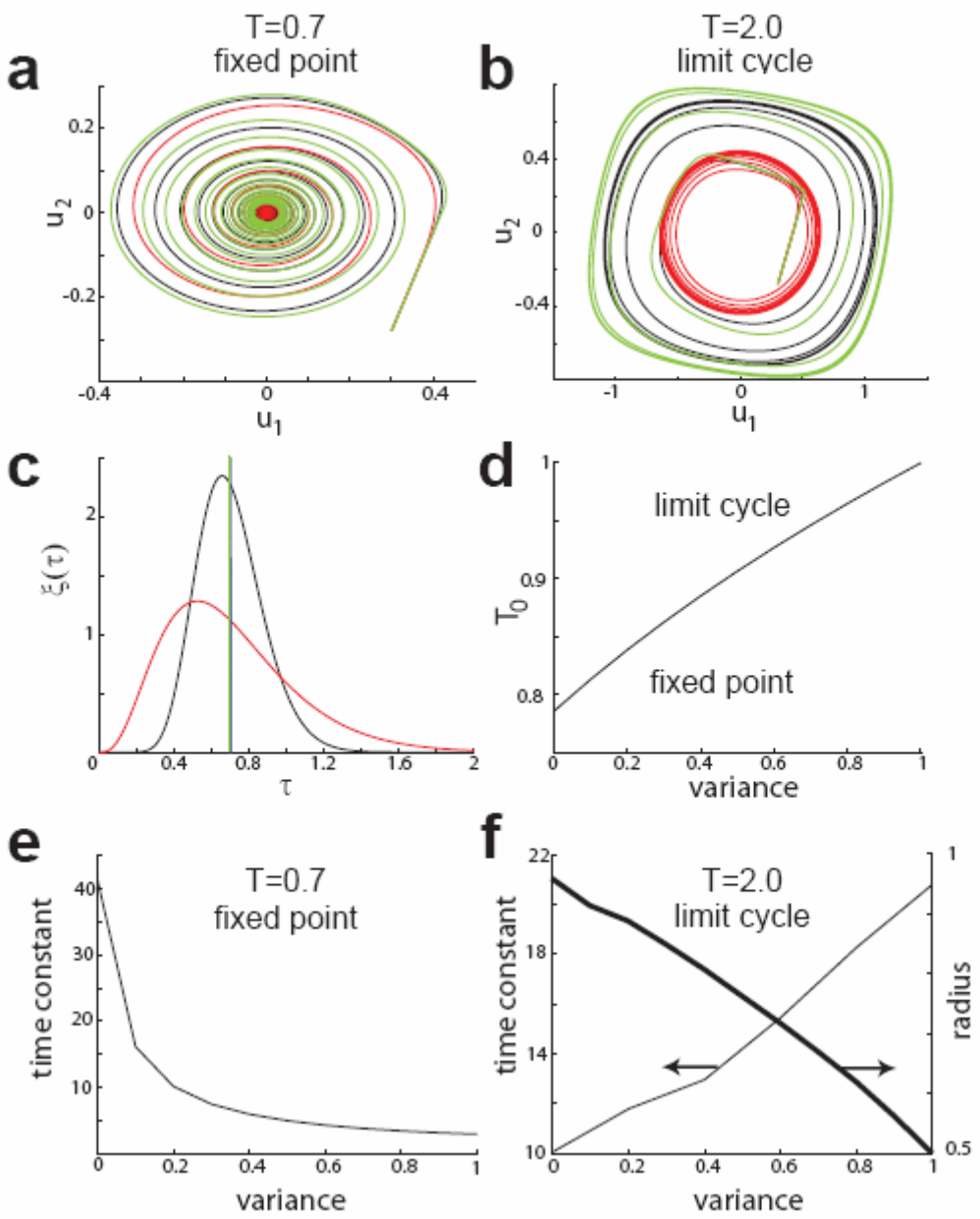

Figure 4.3 Mean delays and attractors. a, b Dynamics of the 2-neuron model system for gamma distributions with mean delay values of $T = 0.7$ (a, fixed point) and $T = 2.0$ (b, limit cycle), respectively. For both cases, the standard deviation is 0 % (green), 25 % (black), and 50 % (red) of the mean delay. The initial condition is $u_1(t) = 0.30$ and $u_2(t) = -0.28$ for $-\tau \le t \le 0$. c

Gamma distribution for a mean delay value of $T = 0.7$ and a standard deviation of 0 % (green), 25 % (black), and 50 % (red) of the mean delay. Note that the CV of the distribution shown in black corresponds approximately to the CV of the physiologically measured delay distributions. d Critical mean delay, T_0, where the Hopf bifurcation takes place, plotted against variance. e Time constant for reaching the fixed point for $T = 0.7$ plotted against the variance of the gamma distribution. f Time constant (thin curve, left axis) for reaching the limit cycle and radius of the limit cycle (thick curve, right axis) for $T = 2.0$ plotted against the variance of the gamma distribution.

Separating real and imaginary parts, we get a system of two equations, which, for a given variance v, we solve in ω and T. The system has multiple solutions, and the solution with the minimum positive mean delay T determines the critical mean delay T_0, for which the fixed point at the origin loses its stability and a stable limit cycle emerges. To find this solution, we apply Newton's method, where we choose the starting values for the algorithms by inspection of the oscillatory system dynamics near the bifurcation. Our analysis shows the introduction of distributed delays (increasing variance) leads to a smaller limit cycle (Fig. 4.3b, f). Furthermore, the critical mean delay T_0 increases with increasing variance (Fig. 4.3d).

To estimate the time constant for reaching an attractor, we calculated the distance, $D_\theta(t) = \sqrt{u_1^2(t) + u_2^2(t)}$, from the origin along a given polar angle, θ, in the $u_1(t)$ and $u_2(t)$ space. Assuming an exponential dependence, a fit of an exponential function to the simulated $D_\theta(t)$ values provided the time constant for that polar angle. We repeated the procedure for 360 polar angles in 1-deg increments and took the final time constant to be the mean of the 360 time constants at given polar angles. This analysis shows that increasing variance makes the convergence to the fixed points faster (Fig. 4.3e) and the convergence to limit cycles slower (Fig. 4.3f).

In summary, distributed delays increase the parameter region with fixed-point behavior and accelerate the convergence to the fixed point.

We also simulated the system for distributions with the same variance but different means (Fig. 4.4a). We find that the convergence to the limit cycle is fastest when the mean of the delay distribution is smallest (Fig. 4.4b). The system dynamics are thus influenced by the mean and variance of the delay distribution. To investigate the importance of the particular shape of the delay distribution for the system dynamics, we simulated the two-neuron system for different distributions with the same mean and variance. We used three different distributions consisting of two superimposed delta distributions each and a gamma distribution (Fig. 4.4c). We find that the system dynamics are almost identical for the four cases despite the very different shapes of these distributions

(Fig. 4.4d). We therefore conclude that the mean and variance of the delay distribution determine the system dynamics almost exclusively, while higher moments of the distributions appear not to be important. Convergence to the fixed point is accelerated when the mean of the distribution is decreased and when its variance is increased.

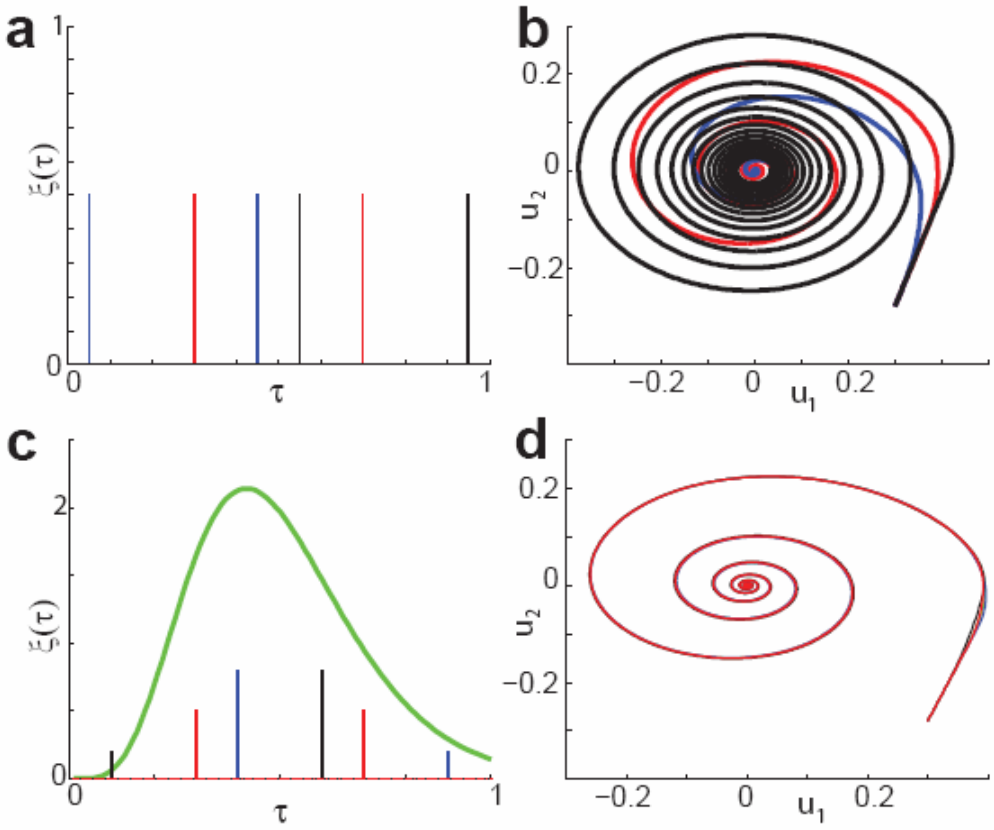

Figure 4.4 System dynamics for different delay distributions. a Delay distributions with same variance and different means. The distributions shown in blue, red, and black consist of two superimposed delta distributions. The weight of each delta distribution is indicated by the height of the peak, the standard deviation of each distribution is 0.2. The mean delay values of the distributions in blue, red, and black are 0.25, 0.5,

and 0.75, respectively. b System dynamics for the delay distributions shown in (a). Line colors indicate the delay distribution in (a) that was used for the simulation. The time constants of approaching the fixed point are 1.72 (blue), 4.57 (red) and 20.71 (black). c Different delay distributions with the same mean and variance. The distributions shown in blue, red, and black consist of two superimposed delta distributions. The weight of each delta distribution is indicated by the height of the peak. The green curve represents a Gamma distribution. All distributions have a mean delay of $T = 0.5$ **and a standard deviation of 40% of the mean. d System dynamics for the delay distributions shown in (c). Line colors indicate the delay distribution in (c) that was used for the simulation. Because of the similarity in dynamics, the 4 curves largely overlap. The time constants of approaching the fixed point are 4.53 (blue), 4.57 (red), 4.62 (black), and 4.55 (green).**

4.5 Discussion

Delays in feedback loops can determine the dynamical behavior of the system (Coleman and Renninger 1976; an der Heiden 1979; Milton 1996; Fisher et al. 2006). In nonlinear systems, the distribution of a system parameter can have unexpected effects on the systems dynamics (Braiman et al. 1995; Brandt et al. 2006b; Chacón and Martínez 2007). Consequently, it is important to investigate the impact of delay distributions on the system dynamics. In this study, we have

quantified the distribution of delays in the avian isthmotectal feedback loop (Fig. 4.2). Furthermore, by investigating a mathematical model of coupled neurons with distributed delays, we have demonstrated that distributed delays enhance the stability of the system by increasing the parameter region with fixed-point behavior (Fig. 4.3d) and by accelerating the convergence to the fixed point (Fig. 4.3e). Further, we have shown that the mean and variance of the delay distribution determine the system dynamics, whereas the shape of the distribution has little impact (Fig. 4.4).

Computational and mathematical analysis of the dynamics in a network model of the isthmotectal feedback loop has shown that the degree to which this circuit can function as a winner-take-all (WTA) network may depend critically on the delays in the system (Brandt and Wessel 2007b). In particular, it has been demonstrated that WTA behavior may arise from the delay dependence of the time constants that govern oscillations and relaxation to the fixed point. Therefore, the physiologically measured distribution of transmission delays in the isthmotectal feedback loop (Fig. 4.2) and the resulting accelerated convergence to the fixed point (Fig. 4.3e) may be important to WTA selection in the system and consequently to its role in mediating selective attention (Marin et al. 2007).

4.6 Experimental methods

White Leghorn chick hatchlings (Gallus gallus) of less than 3 days of age were used in this study. All procedures used in this study were approved by the local authorities and conform to the guidelines of the National Institutes of Health on the Care and Use of Laboratory Animals. Animals were injected with ketamine (40 mg per kg, i.m.). Brain slices of the midbrain were prepared following published protocols (Dye and Karten, 1996; Luksch et al. 1998; 2001; 2004; Khanbabaie et al. 2007). Briefly, preparations were done in 0°C, oxygenated, and sucrose-substituted saline (240 mM sucrose, 3 mM KCl, 5 mM $MgCl_2$, 0.5 mM $CaCl_2$, 1.2 mM NaH_2PO_4, 23 mM $NaHCO_3$, and 11 mM D-glucose). After decapitation, the brains were removed from the skull, and the forebrain, cerebellum, and medulla oblongata were discarded. A midsagittal cut was used to separate the tectal hemispheres. The tectal hemispheres were sectioned at 500 μm on a tissue slicer (Vibroslice, Campden and VF-200, Precisionary Instruments) in either the transverse or the horizontal plane. Slices were collected in oxygenated saline (120 mM NaCl, 3 mM KCl, 1 mM $MgCl_2$, 2 mM $CaCl_2$, 1.2 mM NaH_2PO_4, 23 mM $NaHCO_3$, and 11 mM D-glucose) and kept submerged in a chamber that was bubbled continuously with carbogen (95% oxygen, 5% CO_2) at room temperature. The slice was then transferred to a recording chamber (RC-26G, Warner Instruments) mounted on a fixed stage upright microscope equipped with differential interference contrast optics (BX-51WI, Olympus). The slice was held gently to the bottom of the chamber with an anchor of nylon threads, and the chamber was perfused continuously with oxygenated saline at room temperature. The potential effects of

temperature or age on measured signal delays were not addressed in this study. The cells in L10, Imc, and Ipc are visible with DIC optics.

Local electrostimulation was achieved by inserting bipolar tungsten electrodes under visual control into either the upper tectal retinorecipient layers (2 to 4), layer 5b, or the isthmic nuclei Ipc or Imc with a three-axis micromanipulator (U-31CF, Narishige). Electrodes were custom-built from 50-µm diameter, insulated tungsten wires (California Fine Wire) that were glued together with cyanoacrylate and mounted in glass microcapillaries for stabilization. The wires protruded several hundred µm from the capillaries, and the tips were cut at an angle. Stimulus isolators (Isolated Pulse Stimulator 2100, AM Systems) generated biphasic current pulses (20 – 200 µA, 500 µs).

Whole-cell recordings were obtained with glass micropipettes pulled from borosilicate glass (1.5 mm OD, 0.86 mm ID, AM Systems) on a horizontal puller (P-97, Sutter Instruments and DMZ Universal Puller, Zeitz Instruments) and were filled with a solution containing 100 mM K-Gluconate, 40 mM KCl, 10 mM HEPES, 0,1 mM $CaCl_2$, 2 mM $MgCl_2$, 1.1 mM EGTA, 2 mM Mg-ATP, pH adjusted to 7.2 with KOH. Electrodes were advanced through the tissue under visual guidance with a motorized micromanipulator (MP-285, Sutter Instruments) while constant positive pressure was applied and the electrode resistance was monitored by short current pulses. Once the electrode had attached to a membrane and formed a seal, access to the cytosol was achieved by brief

suction. Whole-cell recordings were performed with the amplifier (Axoclamp 2B, Axon Instruments and SEC-05L, npi-electronic) in the bridge mode (current clamp). The series resistance was estimated by toggling between the bridge and the DCC (discontinuous current clamp) mode. The series resistance was compensated with the bridge balance. Analog data were low-pass filtered (4-pole Butterworth) at 1 kHz, digitized at 5 kHz, stored, and analyzed on a PC equipped with an PCI-MIO-16E-4 and LabView software (both National Instruments).

Labeling of a subset of recorded neurons was carried out as described previously (Luksch et al., 1998, 2001, 2004; Mahani et al. 2006). In brief, whole-cell patch recordings were obtained as described above. Additionally, the electrode solution contained 0.5% Biocytin (w/v) to label the recorded neurons. Individual cells were filled intracellularly with 2 nA of positive current over 3 minutes. After recording and labeling, slices were kept in oxygenated ACSF for an additional 30 minutes and subsequently fixed by immersion in 4% paraformaldehyde in PB for at least 4 hours. Slices were then washed in phosphate buffer (PB, 0.1 M, pH 7.4) for at least 4 hours, immersed in 15% sucrose in PB for at least 4 hours and then immersed in 30% sucrose in PB for 12 hours, and resectioned at 60 µm on a freezing microtome. The sections were collected in PB and the endogenous peroxidase blocked by a 15-minute immersion in 0.6% hydrogen peroxide in methanol. The tissue was washed several times in PB, and then incubated in the avidin-biotin complex solution (ABC *Elite* kit, Vector Labs) and the reaction product visualized with a heavy-metal intensified DAB protocol. Following several

washes in PB, the 60 µm-thick sections were mounted on gelatin-coated slides, dried, dehydrated, and coverslipped. Sections were inspected for labeled neurons, and only data from cells that could unequivocally be classified according to published criteria (Wang et al. 2004, 2006) were taken for further analysis. Cells were reconstructed at medium magnification (10x to 20x) with a camera lucida on a Leica microscope and projected onto the 2D plane.

4.7 References

Atay FM (2003) Distributed delays facilitate amplitude death of coupled oscillators. Phys Rev L 91: 094101.

Babcock KL, Westervelt RM (1987) Dynamics of simple electronic neural networks. Physica D 28: 305-316.

Bernard S, Belair J, Mackey MC (2001) Sufficient conditions for stability of linear differential equations with distributed delay. Discrete and Continuous Dynamical Systems Series B 1: 233-256.

Braiman Y, Lindner JF, Ditto WL (1995) Taming spatiotemporal chaos with disorder. Nature 378, 465 -467.

Brandt SF, Pelster A, Wessel R (2006a) Variational calculation of the limit cycle and its frequency in a two-neuron model with delay. Phys Rev E 74: 036201.

Brandt SF, Dellen BK, Wessel R (2006b) Synchronization from disordered driving forces in arrays of coupled oscillators. Phys Rev Lett 96, 034104.

Brandt SF, Pelster A. Wessel R (2007a) Synchronization in a neuronal feedback loop through asymmetric temporal delays. Europhysics Letters 79: 38001.

Brandt SF, Wessel R (2007b) Winner-take-all selection in a neural system with delayed feedback. Biol Cybern 97: 221-228.

Chacón R, Martínez PJ (2007) Controlling Chaotic Solitons in Frenkel-Kontorova Chains by Disordered Driving Forces. Phys Rev Lett 98, 224102.

Coleman BD, Renninger GH (1976) Periodic Solutions of Certain Nonlinear Integral Equations with a Time Lag. SIAM J Appl Math 31, 111-120.

Cooke KL, Grossman Z (1982) Discrete delay, distributed delay and stability switches. Journal of Mathematical Analysis and Applications 86: 592-627.

Domesick VB, Morest DK (1977) Migration and differentiation of shepherd's crook cells in the optic tectum of the chick embryo. Neuroscience 2: 477-491.

Dye JC, Karten HJ (1996) An *in vitro* study of retinotectal transmission in the chick: role of glutamate and GABA in evoked field potentials. Vis Neurosci 13: 747-758.

Eurich CW, Mackey MC, Schwegler H (2002) Recurrent inhibitory dynamics: The role of state-dependent distributions of conduction delay times. Journal of Theoretical Biology 216: 31-50.

Eurich CW, Thiel A, Fahse L (2005) Distributed delays stabilize ecological feedback systems. Phys Rev Lett 94: 158104.

Fisher I, Vicente R, Buldu JM, Peil M, Mirasso CR, Torrent MC, Garcia-Ojalvo J (2006) Zero-lag long-range synchronization via dynamical relaying. Phys Rev Lett 97: 123902.

Foss J, Longtin A, Mensour B, Milton J (1996) Multistability and delayed recurrent loops. Phys Rev L 76: 708.

Foss J, Moss F, Milton J (1997) Noise, Multistability, and delayed recurrent loops. Phys Rev E 55: 4536.

Foss J, Milton J (2000) Multistability in recurrent loops arising from delay. J Neurophysiol 84: 975-985.

Gopalsamy K, Leung IKC, Liu P (1998) Global Hopf-bifurcation in a neural netlet. Appl Math Comput 94: 171-192.

Gruberg ER, Dudkin EA, Wang Y, Marin G, Salas C, Sentis E, Letelier JC, Mpodozis J, Malpeli J, Cui H, Ma R, Northmore D, Udin S (2006) Influencing and interpreting visual input: The role of a visual feedback system. J Neurosci 26: 10368-10371.

Güntürkün O, Remy M (1990) The topographical projection of the nucleus isthmi pars parvocellularis (Ipc) onto the tectum opticum in the pigeon. Neurosci Lett 111: 18-22.

an der Heiden U (1979) Delays in physiological systems. J Math Biol 8: 345-364.

Hellmann B, Manns M, Güntürkün O (2001) Nucleus isthmi, pars semilunaris as a key component of the tectofugal visual system in pigeons. J Comp Neurol 436: 153-166.

Hopfield JJ (1984) Neurons with graded response have collective computational properties like those of two-state neurons. P Natl Acad of Sci USA 81: 3088-3092.

Hunt SP, Künzle H (1976) Observations on the projections and intrinsic organization of the pigeon optic tectum: an autoradiographic study based on anterograde and retrograde, axonal and dendritic flow. J Comp Neurol 170: 153-172.

Hunt SP, Streit P, Kunzle H, Cuenod M (1977) Characterization of the pigeon isthmotectal pathway by selective uptake and retrograde movement of radioactive compounds and by Golgi-like horseradish peroxidase labeling. Brain Res 129: 197-212.

Khanbabaie R, Mahani A, Wessel R (2007) Contextual interaction of GABAergic circuitry with dynamic synapses. J Neurophysiol 97: 2802-2811.

Koch C, Ullman S (1985) Shifts in selective visual attention: towards the underlying neural circuitry. Hum Neurobiol 4: 219-227.

Laing CR, Longtin A (2003) Dynamics of deterministic and stochastic paired excitatory-inhibitory delayed feedback. Neural Comput 15: 2779-2822.

Liao X, Li S, Chen G (2004) Bifurcation analysis on a two-neuron system with distributed delays in the frequency domain. Neural Networks 17: 545-561.

Luksch H, Cox K, Karten HJ (1998) Bottlebrush dendritic endings and large dendritic fields: motion-detecting neurons in the tectofugal pathway. J Comp Neurol 396: 399-414.

Luksch H, Karten HJ, Kleinfeld D, Wessel R (2001) Chattering and differential signal processing in identified motion sensitive neurons of parallel visual pathways in chick tectum. J Neurosci 21: 6440-6446.

Luksch H (2003) Cytoarchitecture of the avian optic tectum: Neuronal substrate for cellular computation. Rev in the Neurosciences 14: 85-106.

Luksch H, Khanbabaie R, Wessel R (2004) Synaptic dynamics mediate sensitivity to motion independent of stimulus details. Nat Neurosci 7: 380-388.

Mahani AS, Khanbabaie R, Luksch H, Wessel R (2006) Sparse spatial sampling for the computation of motion in multiple stages. Biol Cybern 94: 276-287.

Maczko KA, Knudsen PF, Knudsen EI (2006) Auditory and visual space maps in the cholinergic nucleus isthmi pars parvocellularis in the barn owl. J Neurosci 26: 12799-12806.

Marcus CM, Westervelt RM (1989) Stability of analog neural networks with delay. Phys Rev *A* 39: 347-359.

Marin G, Mpodozis J, Sentis E, Ossandon T, Letelier JC (2005) Oscillatory bursts in the optic tectum of birds represent re-entrant signals from the nucleus isthmi pars parvocellularis. J Neurosci 25: 7081-7089.

Marin G, Salas C, Sentis E, Rojas X, Letelier JC, Mpodozis J (2007) A cholinergic gating mechanism controlled by competitive interactions in the optic tectum of the pigeon. J Neurosci 27: 8112-8121.

Milton J (1996) Dynamics of small neural populations. American Mathematical Society.

Ramón y Cajal S (1911) Le lobe optique des vertébrés inférieurs, toit optique des oiseaux. In: Histologie du système nerveux de l'homme et des vertébrés (Ramón y Cajal S, ed), pp 196-212. Madrid.

Sebesteny T, Davies DC, Zayats N, Nemeth A, Tömböl T (2002) The ramification and connections of retinal fibres in layer 7 of the domestic chick optic tectum: a golgi impregnation, anterograde tracer and GABA-immunogold study. J Anat 200: 169-183.

Sereno MI, Ulinski PS (1987) Caudal topographic nucleus isthmi and the rostral nontopographic nucleus isthmi in the turtle, *Pseudemys scripta*. J Comp Neurology 261: 319-346.

Shepherd GM (2003) The synaptic organization of the brain. Oxford Univ Press, New York.

Thiel A, Schwegler H, Eurich CW (2003) Complex dynamics is abolished in delayed recurrent systems with distributed feedback times. Complexity 8: 102-108.

Tömböl T, Egedi G, Németh A (1995) Some data on connections of neurons of nuclei isthmi of the chicken. J Hirnforsch 36: 501-508.

Tömböl T, Németh A (1998) GABA-immunohistological observations, at the electron-microscopical level, of the neurons of isthmic nuclei in chicken, Gallus domesticus. Cell Tissue Res 291: 255-266.

Wang YC, Frost BJ (1991) Visual response characteristics of neurons in the nucleus isthmi parvocellularis of pigeons. Exp Brain Res 87: 624-633.

Wang SR (2003) The nucleus isthmi and dual modulation of the receptive field of tectal neurons in non-mammals. Brain Res Rev 41: 13-25.

Wang Y, Major DE, Karten HJ (2004) Morphology and connections of nucleus isthmi pars magnocellularis in chicks (Gallus gallus). J Comp Neurol 469: 275-297.

Wang Y, Luksch H, Brecha NC, Karten HJ (2006) Columnar projections from the cholinergic nucleus isthmi to the optic tectum in chicks (*Gallus gallus*): A possible substrate for synchronizing tectal channels. J Comp Neurol 494:7-35.

Woodson W, Reiner A, Anderson K, Karten HJ (1991) Distribution, laminar location, and morphology of tectal neurons projecting to the isthmo-optic nucleus and the nucleus isthmi, pars parvocellularis in the pigeon (Columba livia) and chick (Gallus domesticus): a retrograde labelling study. J Comp Neurol 305: 470-488.

Wei J, Ruan S (1999) Stability and bifurcation in a neural network with two delays. Physica *D* 130: 255-272.

Zhao H (2003) Global stability of neural networks with distributed delays. Physical Review *E* 68: 051909.

Chapter 5

THE REGULATORY ROLE OF GABAERGIC IMC NEURONS IN THE AVIAN ISTHMOTECTAL SYSTEM: TRANSITION FROM EXCITATION TO SUPPRESSION

5.1 Abstract

GABA is the major neurotransmitter that mediates inhibition in the mammalian central nervous system. In general, GABA-mediated synaptic currents hyperpolarize the post-synaptic neurons away from threshold for generating action potentials, thus reducing the excitability of targeted neurons. In the avian isthmotectal circuitry, the nucleus isthmi pars parvocellularis (Ipc) receives inputs from the GABAergic nucleus isthmi pars magnocellularis (Imc). The physiological properties of this projection were explored in a brain slice preparation. We found that extracelluar stimulating Imc neurons evoked EPSPs and action potentials in the Ipc neurons and the responses were blocked by bicuculline, a $GABA_A$ receptor antagonist. We also found that stimulating the Imc nucleus while applying suprathreshold currents to the soma of post-synaptic Ipc neurons suppresses spiking in some Ipc neurons. The suppression period can last for up to a few hundred milliseconds after the stimulus has been turned off. This observation provides insight into the regulatory role of a GABAergic projection in a cholinergic feedback loop.

5.2 Introduction

Gamma amino butyric acid (GABA) is the main inhibitory neurotransmitter in the central nervous system. Its principle action, which is mediated by ubiquitous ionotropic $GABA_A$ (GABA type A) receptors, is to increase membrane permeability to chloride. Therefore, the concentration gradient for chloride across the cell membrane determines the nature of inhibitory effects. If the synaptic reversal potential of $GABA_A$-receptor-mediated current is below the resting membrane potential, it leads to a net inward flow of anions and thus a hyperpolarizing post-synaptic response that drives membrane potential away from spiking threshold. If the synaptic reversal potential is between the resting membrane potential and the threshold for the generation of action potential, GABAergic synapses will have shunting effects (Alger and Nicoll 1979; Andersen et al., 1980; Staley and Mody1992). Besides hyperpolarizing and shunting, if the synaptic reversal potential is above the action potential threshold, GABAergic synapse can be excitatory. Excitatory effects of GABA have been found both in early development and mature neurons (Staley et al., 1995; Taira et al., 1997; Ben-Ari, 2002, Gulledge and Stuart, 2003). In some systems, however, the effects of GABA can not be simply predicted by comparison of synaptic reversal potential and spiking threshold, many other factors need to be taken into account, for example synapse locations (Miles et al., 1996; Gulledge and Stuart, 2003), consequently evoked membrane currents (Monsivais et al., 2000; Monsivais and Rubel, 2001;) and network connection schemes (Buzsaki 1984; Pouille and Scanziani, 2001). Especially in the context of a network when interacting with

excitatory elements in the system, GABA-induced responses may greatly increase the complexity of the firing patterns in the involving neurons (Buzsaki and Chrobak 1995; Salinas and Sejnowski, 2001; Engel et al., 2001; Markram et al., 2004; Watts and Thomson, 2005; Bartos et al., 2007).

The avian isthmotectal system (Fig. 5.1) plays a key role in visual information processing (Cook 2001; Wang 2003; Maczko et al. 2006; Marin et al. 2007). It consists of three key anatomical elements. A subpopulation of tectal layer 10 (L10) neurons receive retinal inputs and project to the ipsilateral nucleus isthmi pars parvocellularis (Ipc) and the nucleus isthmi pars magnocellularis (Imc) in a topographic fashion (Wang et al. 2004, 2006). The cholinergic Ipc neurons form topographic reciprocal connections with the tectum (Wang et al. 2006). The GABAergic Imc neurons consist of two cell types. One type projects upon tectal layers 10 to 13, whereas the other projects broadly to the Ipc (Wang et al. 2004).

The functional features of Imc-to-Ipc projection were explored in a chick brain slice preparation (Fig. 5.1). We conducted whole-cell patch and gramicidin-perforated patch recordings from Ipc neurons while extracellularly stimulating the Imc. Three lines of evidence suggest that GABA-induced response in Ipc neuron depolarize its membrane potential from the resting value towards or even

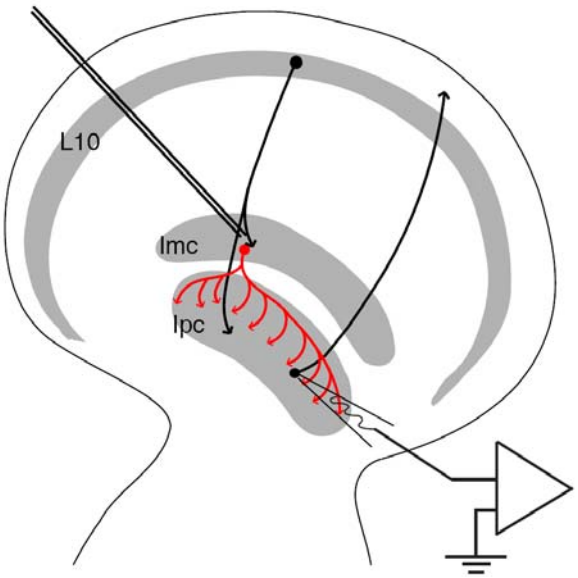

Figure 5.1 Schematic drawing of isthmotectal feedback circuitry and experimental setup. Notice the location of stimulation electrode in Imc and the recording electrode in Ipc. To select the Imc-to-Ipc synaptic connection, we stimulated in an area of the Imc nucleus that did not correspond to the topographic location of the recorded Ipc neuron, thus avoiding both antidromic stimulation of the axon from the recorded Ipc neuron as well as avoiding orthodromic stimulation of the L10 axons passing through the Imc nucleus on their way to the same location in the Ipc nucleus.

exceeding the spiking threshold: 1) All Ipc neurons receive spontaneous GABAergic synaptic currents which induce EPSPs and occasional spikes; 2) Single electrical pulse stimulation in Imc can evoke action potentials in the responding Ipc neuron. 3) Bath applying 0.1 mM GABA depolarized the membrane potential of Ipc neurons. However, further experiments showed that this apparent excitation can switch to spike suppression depending on the

existing activities of Ipc neurons: stimulating Imc while simultaneously applying currents into the soma of post-synaptic Ipc neuron suppressed the action potentials in Ipc neurons, which would otherwise be triggered by suprathreshold somatic current injections. This suppression period can last for to a few hundred milliseconds after the Imc stimulation. Our findings suggested that the GABAergic Imc may play a regulatory role rather than solely inhibition in the isthmotectal feedback loop.

5.3 Methods

5.3.1 Experiments

White leghorn chick hatchlings (Gallus gallus) under three days old (unless otherwise noted, i.e. P8-P10 chickens) were used in this study. All procedures used in this study were approved by the local authorities and conform to the guidelines of the National Institutes of Health on the Care and Use of Laboratory Animals. Animals were anesthetized with ketamine (100 mg/kg) and decapitated, and the brain was quickly removed and immersed in ice-cold, oxygenated, and sucrose-substituted artificial CSF (240 mM sucrose, 3 mM KCl, 3 mM $MgCl_2$, 1.2 mM NaH_2PO_4, 23 mM $NaHCO_3$, and 11 mM D-glucose). The forebrain, cerebellum, and medulla oblongata were discarded, and the remaining tectodiencephalic area was separated by a midsagittal cut. The optic tectum was sectioned at 350-400 μm on a vibratome (VF-200 Microtome, Precisionary Instrument Inc.) in the transverse plane. Slices were collected in oxygenated ACSF (120 mM NaCl, 3 mM KCl, 1 mM $MgCl_2$, 2 mM $CaCl_2$, 1.2 mM NaH_2PO_4,

23 mM $NaHCO_3$, and 11 mM D-glucose), and kept submerged in a chamber that was continuously bubbled with carbogen (95% oxygen and 5% CO_2) at room temperature. Slices were allowed to recover for 1 hour before recording. The slice was then transferred to a custom-built submersion-type chamber mounted on either a mobile-stage or fixed-stage microscope (Olympus, Japan) equipped with long-range working distance optics. The slice was gently held to the bottom mesh of the chamber by a stainless steel anchor with Lycra threads (Warner Instruments, Hamden, CT), and the chamber was continuously perfused with oxygenated ACSF at room temperature. All reagents were mixed with ACSF and then bath applied to the slices. Unless otherwise noted, all reagents were obtained from Sigma (St. Louis, MO).

Whole-cell patch recordings were obtained with glass micropipettes pulled from borosilicate glass (1.5 mm outer diameter; 0.86 mm inner diameter; AM Systems, Carlsborg, WA) on a horizontal puller (Sutter Instruments, San Rafael, CA) and filled with a solution containing 100 mM K-gluconate, 40 mM KCl, 10 mM HEPES, 0.1 mM $CaCl_2$, 2 mM $MgCl_2$, 1.1 mM EGTA, and 2 mM Mg-ATP; pH was adjusted to 7.2 with KOH. Electrodes were advanced through the tissue with a motorized micromanipulator (MP-285, Sutter Instruments, San Rafael, CA) while constant positive pressure was applied. After the electrode had attached to a membrane and formed a seal, access to the cytosol was achieved by brief suction. Whole-cell patch recordings (current clamp) were performed with the amplifier (Axoclamp 2B, Axon Instruments, Foster City, CA) in the bridge mode.

The series resistance was compensated with the bridge balance. Recordings with voltage clamp were performed with the same amplifier in the SEVC (Single Electrode Voltage Clamp) mode. The sample rate was set optimized by monitoring the output on an oscilloscope.

The liquid junction potential (measured in ACSF and calculated by pClamp, Molecular Devices, Sunnyvale, CA) was 11 mV. All data shown in this chapter have been corrected for the liquid junction potential.

Electrodes for gramicidin-perforated-patch recordings are similarly pulled as those of whole cell patching recordings. After filling the pipette tip with a solution containing 150 mM KCl and 10 mM HEPES, the pipette shank was backfilled by a syringe with the same solution additionally containing gramicidin dissolved DMSO at a final concentration of 40 μg/ml. For perforated-patch recording, after giga-ohm seal formation there was no brief suction to rupture the cell membrane. The series resistance measurements then decreased to <100 MΩ within 45 mins, at which time data acquisition began. Recordings were aborted if the perforated patch ruptured, which was easily detected by the reversal of EPSP polarity because of the high concentration of Cl^- in the electrode.

Local electrostimulation was achieved by inserting bipolar tungsten electrodes under visual control into Imc with a three-axis micromanipulator (U-31CF, Narishige). Electrodes were custom-built from 50-μm diameter, insulated

tungsten wires (California Fine Wire) that were glued together with cyanoacrylate and mounted in glass microcapillaries for stabilization. The wires protruded several hundred μm from the capillaries, and the tips were cut at an angle. Stimulus isolators (Isolated Pulse Stimulator 2100, AM Systems) generated biphasic current pulses (20 – 200 μA, 500 μs).

Analog data were stored, and analyzed on a personal computer equipped with a data acquisitition card (PCI-MI0-16E-4) and LabView software (both National Instruments, Austin, TX). Data were analyzed by cumtomized Matlab program (The MathWorks Inc, Natick, MA).

5.3.2 Modeling

Simulations were implemented and run with NEURON (version 6.1). Ipc neuron was simulated as two compartments: soma and dendrite. The geometry parameters of soma (50 μm in diameter, 25 μm in length) and dendrite (4 μm in diameter, 225 μm in length) were estimations according to the anatomy (Wang et al., 2004, 2006). Rest membrane potential was set at – 60 mV. External current was injected into the soma. Equations and parameters for Hodgin-Huxley (HH) channels were adopted from hippocampus neurons (Taube and Miles, 1991). HH potassium channel was implemented onto soma and dendrite and temperature was set at 36 °C. HH sodium channel was only implemented onto dendrite as the segregation of sodium channel away from soma may be necessary for the shunting (Howard and Rubel, 2007). GABAergic synapse was set onto the

dendrite with a reversal potential of – 40 mV. M-current, a slow K+ current activated by depolarization (Yamada et al., 1989), was implemented onto the dendrite to reproduce spike rate adaptation and long lasting suppression seen in the Ipc neuron.

5.4 Results

5.4.1 Excitatory effects of GABA on Ipc neurons

To study the role of GABA in the isthmotectal feedback loop, we first examined the nature of the Imc-to-Ipc synaptic currents. We extracelluarly stimulated at Imc with one brief electrical pulse and recorded the responses in the postsynaptic Ipc neurons. The evoked responses were either an EPSP or an action (Fig 5.2A, n = 36). Only those Ipc neurons, whose responses to the Imc stimulation were blocked by 100 μM bicuculline (Fig. 5.2B), were included in the data set for analysis. All others were excluded because of the possible stimulation of antidromic and orthodromic axons passing through Imc (Fig. 5.1). By recording the evoked synaptic currents at different holding potentials under voltage clamp (n = 4) we were able to determine a reversal potential of - 34.5 ± 4.3 mV (Fig. 5.2C).

Our previous study showed that even in the brain slice preparation Ipc neurons exhibited spontaneous EPSPs and action potentials which were mediated by GABA (Chapter 2). To explore the effects of GABA on Ipc neuron's resting membrane potential and spontaneous activity, we directly added GABA (100 μM)

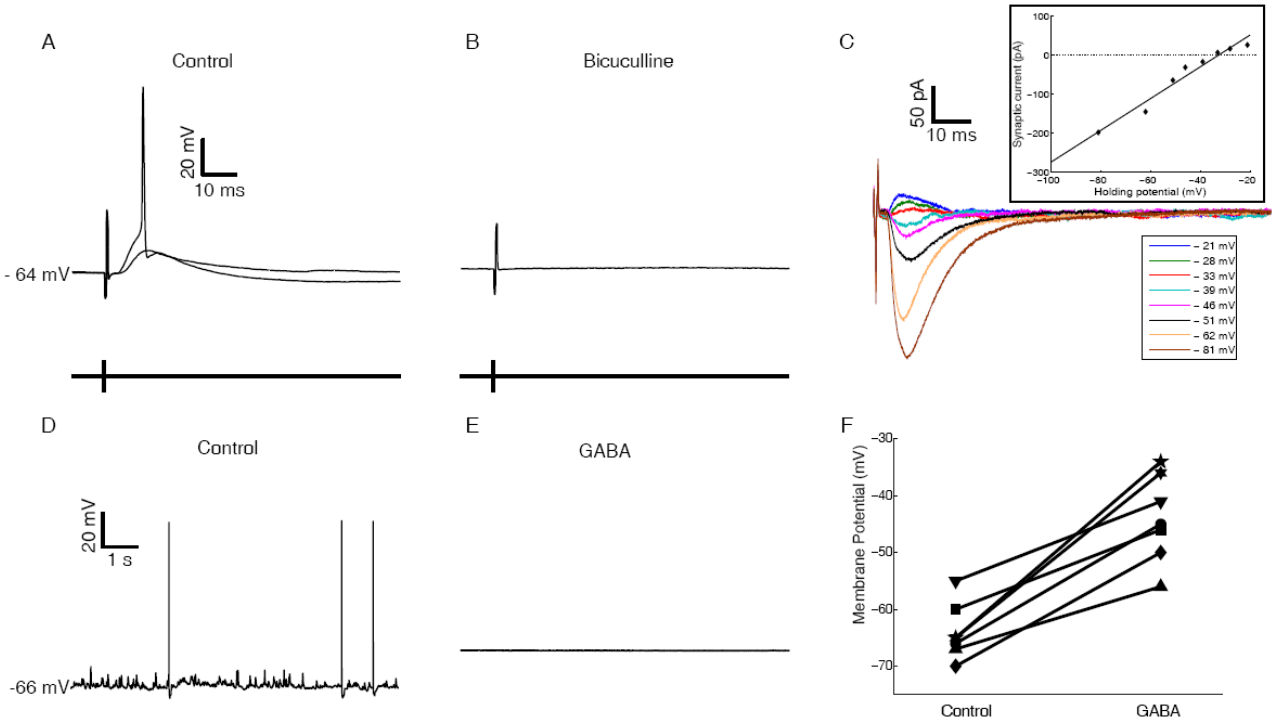

Figure 5.2 Effects of GABA on Ipc neurons. (A) Ipc neuron responded to single pulse extracellular stimulation of GABAergic Imc neurons with an EPSP or an action potential. (B) The response was blocked by 100 μM bicuculline. (C) Recordings of Imc to Ipc synaptic currents (voltage clamp) at different holding potentials. Each trace is an average of 5 trials. Inset, corresponding plot of synaptic currents Vs holding potentials, the black line is a linear fit ($I_{syn}(V_{hold}) = 4.0601 \times V_{hold} + 132.32$; I_{syn} *units in pA,* V_{hold} *units in mV;* $R^2 = 0.9588$). (D) Recording of 10 seconds spontaneous activity in an Ipc neuron; (E) Bath applying 0.1mM GABA depolarized the membrane potential of the Ipc neuron, and no spontaneous activity was found at the depolarized state. (F) Increases of membrane potential in seven Ipc neurons caused by bath applying GABA.

into the ACSF. In the control condition, all recorded Ipc neurons (n= 7) have spontaneous EPSPs and spikes as described in chapter 2 (Fig. 5.2D); the bath application of GABA quickly increased their membrane potentials (Fig. 5.2E) and no spontaneous activity was found in the depolarized state. The resting membrane potentials of the Ipc neurons shifted an average of 20.2 ± 7.7 mV after the application of GABA (Fig. 5.2F).

The reversal potential for GABAergic synaptic currents is mainly determined by the chloride concentration across the neuron membrane. To examine the effects of GABA without bringing artifactual changes to the intracellular chloride concentration, we conducted gramicidin-perforated patch recordings from Ipc neurons (n=5). The recorded spontaneous EPSPs and spikes showed that spontaneous GABAergic inputs to the Ipc neuron were excitatory (Fig. 5.3A). Bath application of 100 μM GABA increased the Ipc neuron's membrane potential from – 70 mV to - 50 mV. No spontaneous spikes or EPSPs were found under the use of GABA (Fig. 5.3B). An EPSP was evoked by briefly stimulating Imc (Fig. 5.3C, D).

Depolarizing action of GABAergic currents usually happens in animal's early development phase. To test if the depolarizing effects of GABA we found from P1-P3 chickens is an indicator for immaturity, we conducted the whole cell patch recordings from P8-P10 chickens (n = 4). Figure 5.3E-H showed the excitatory effects of GABA were the same as recorded from P1-P3 chickens: spontaneous

EPSPs mediated by GABA; GABA depolarized the Ipc neuron's membrane potential and Imc evoked GABAergic currents generated an EPSP in the Ipc neuron.

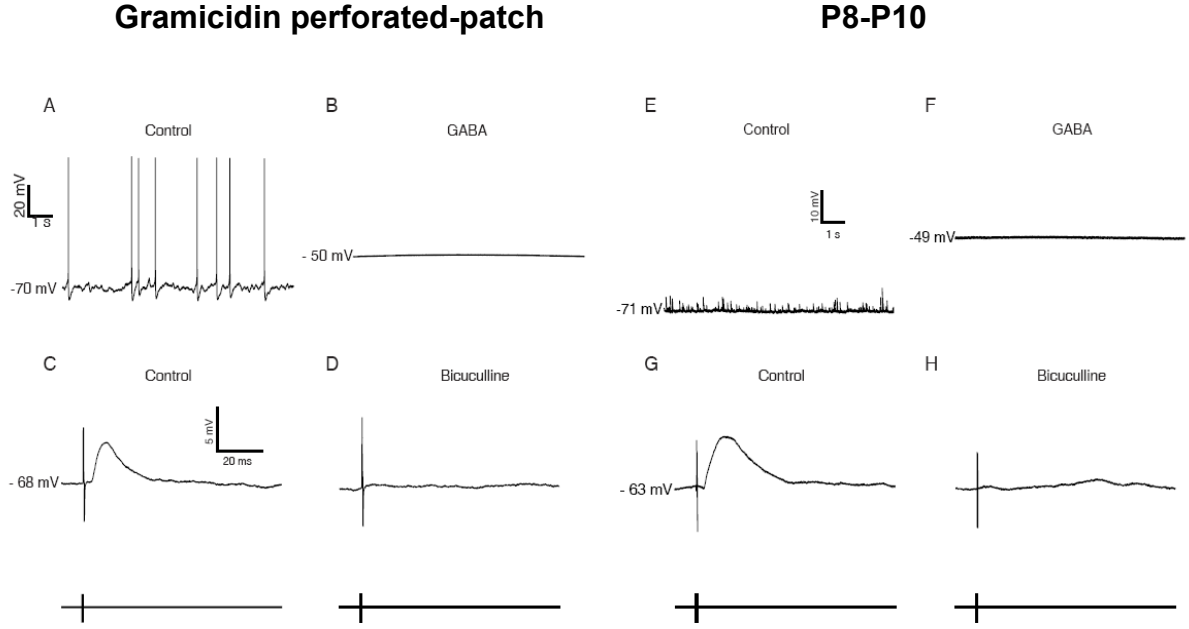

Figure 5.3 Gramicidin perforated-patch recordings (A-D) and recordings from P8-P10 chickens (E-H). (A), (E) Spontaneous activity in the Ipc neuron; (B), (F) Bath applying 0.1mM GABA depolarized the membrane potential of the Ipc neuron, and no spontaneous activity was found at the depolarized state; (C), (G) Ipc neuron responded to the single pulse stimulation at Imc with an EPSP; (D), (H) the response was blocked by 100 μM bicuculline.

To examine the actions of GABA when it was locally applied to the Ipc instead of being bath applied to the whole brain slice, we stimulated at the Imc with a train of pulses so that a relatively large amount of GABA were locally released onto

Ipc neurons via Imc-to-Ipc synapses. Figure 5.4 showed the responses in two Ipc neurons when a train of electrical pulses was given to the Imc at different frequencies. At lower stimulus frequency (10 Hz in Fig. 5.4A; 20 Hz in Fig. 5.4B), the Ipc neurons responded to every pulse with an action potential or an EPSP. When the stimulus frequency increased (100 Hz in Fig. 5.4C; 200 Hz in Fig. 5.4D), Ipc neurons could not respond to every pulse but only with one or two spikes at the beginning, then their membrane potential tended to reach a plateau. High frequency stimulation at Imc may have the similar effect as release large amount of GABA onto the Ipc neuron. It resulted in a continuous depolarization in the Ipc neuron within the stimulation duration.

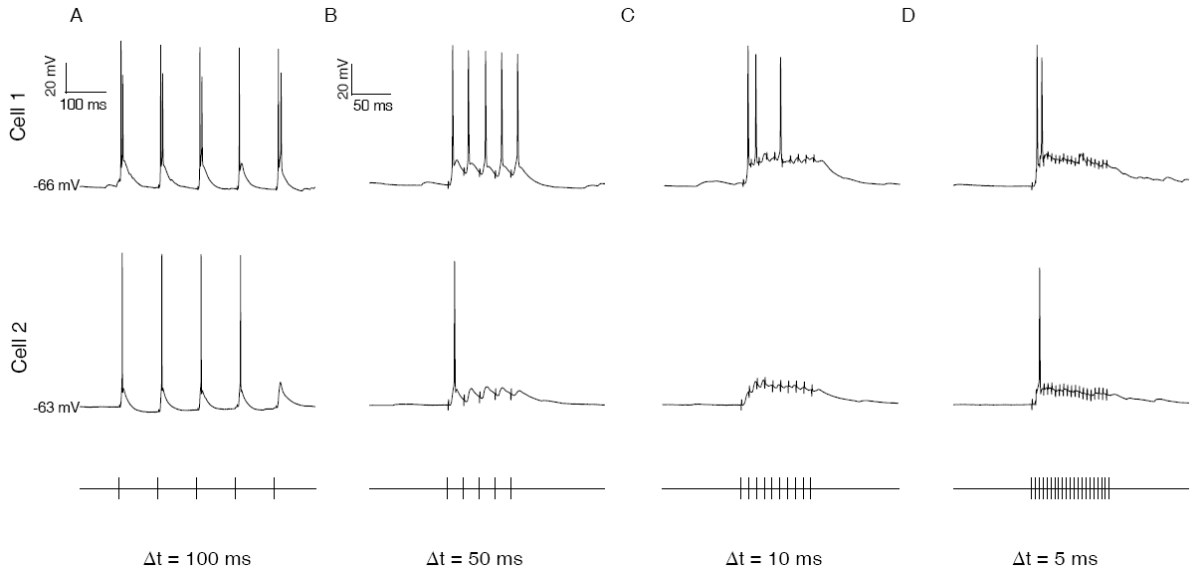

Figure 5.4 Responses in two Ipc neurons to a train of stimuli at Imc. Responses in two Ipc neurons to the stimulation at Imc with a train of 5 pulses at (A) 100 ms interval, (B) 5 pulses at 50 ms interval, (C) 10 pulses at 10 ms interval and (D) 20 pulses at 5 ms interval.

5.4.2 GABA decreased the input resistance of Ipc neuron

The input resistance of Ipc neuron was measured from the averaged voltage deflection during somatic injection of a - 0.1 nA, 500 ms current step (Fig 5.5A, R_{in} = 256 ± 39 MΩ; n = 7). During the application of 100 µM GABA, the measured input resistance was greatly decreased (Fig 5.5B, R_{in} =21 ± 5 MΩ). Also 0.1 nA positive step current which evoked a train of action potentials in the control condition (Fig 5.5A) did not generate any spikes but only a small voltage deflection under the application of GABA. This implies that the activated GABAergic conductance shunts the injected current thus keeping the Ipc neuron from firing action potentials.

To examine if stimulating Imc would also lower the input resistance in Ipc neurons, we measured the input resistance of Ipc neurons during the Imc stimulation (Fig 5.3C; n = 3). Imc was stimulated with a train of 20 pulses at 200 Hz. We estimated the voltage deflections during Imc stimulation by calculating the voltage drop at the end of stimulation period as (V_1-V_2). The voltage deflection under control condition was estimated by calculating (V_3-V_4). The measured input resistance of the Ipc neuron was 212 ± 23 MΩ under control condition and 93 ± 11 MΩ during the Imc stimulation. We assume the Ipc neuron reached equilibrium at state V_1, V_2, V_3 and V_4, and at state V_1 and V_2 the Imc to Ipc synaptic conductance reached its maximum value g_{syn}. Thus we can write four equilibrium state equations: 1) $g_{syn} \times (V_1 - E_{syn}) + g_L \times (V_1 - E_L) = 0$; 2) $g_{syn} \times (V_2 - E_{syn}) + g_L \times (V_2 - E_L) + \Delta I = 0$; 3) $g_L \times (V_3 - E_L) = 0$; 4) $g_L \times (V_4 - E_L) + \Delta I = 0$. Then

we concluded that $g_L = \Delta I / (V_3 - V_4)$ and $(g_L + g_{syn}) = \Delta I / (V_1 - V_2)$. Therefore, the measured decrease in input resistance, or increase in conductance, was due to the opening of GABA-evoked channels.

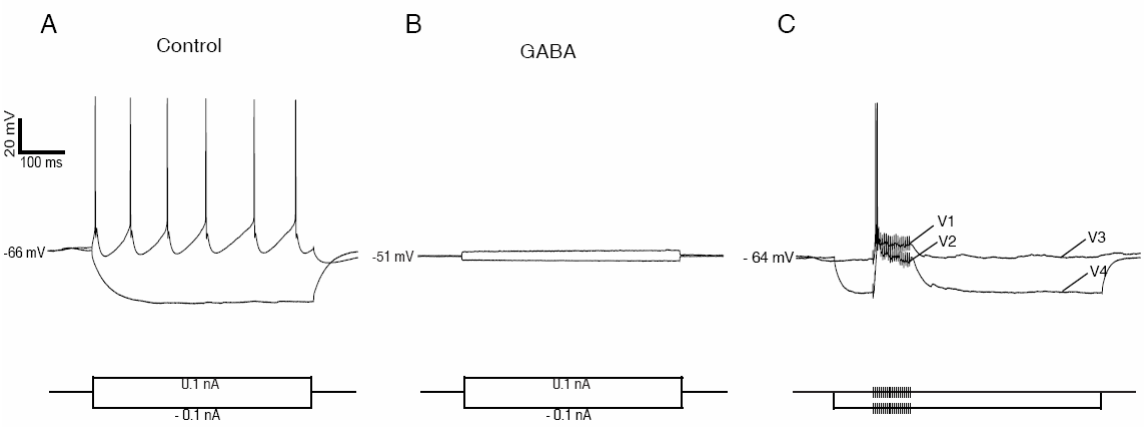

Figure 5.5 GABA decreased the input resistance of lpc neurons. (A) Depolarizing and hyperpolarizing 0.1 nA step current injection into an lpc neuron. (B) Depolarizing and hyperpolarizing 0.1 nA step current injection into an lpc neuron with bath application of 100 μM GABA; (C) High frequency stimulation (200 Hz) at lmc with and without 0.1 nA hyperpolarizing step current injections into lpc neuron.

5.4.3 GABAergic inputs suppressed firing of lpc neuron

GABAergic inputs suppressed action potentials in lpc neurons (n = 13). This effect was demonstrated by stimulating lmc while evoking action potentials in single lpc neuron by intracellular current injection. Under control conditions, one 0.3 nA, 500 ms current step was injected into an lpc neuron. When the neuron was at rest, this current injection reliably evoked a train of action potentials. Then

Imc was stimulated 100 ms after the onset of current injection by a train of 10 shocks at 100 Hz. Spikes in Ipc neuron were suppressed during the stimulation of Imc and continued to be suppressed for approximately 100 ms after the stimulation stopped. The suppression of action potentials during the Imc stimulation could be an outcome of the shunting effect of GABA and a possible concurrent inactivation of sodium channel given the appearance of small amplitude spike during the Imc stimulation (Fig. 5.6A, arrowed). The spike suppression after the stimulation, however, may be mediated by some slow currents triggered by the depolarization during the Imc stimulation. When 100 μM bicuculline was bath applied, current injection evoked a train of action potentials in the Ipc neuron while the stimulation at Imc stimulation had no effect on the firing of the Ipc neuron (Fig. 5.6B).

To examine whether the observed spike suppression was merely caused by further depolarizing current into Ipc neuron, we substituted the stimulation of Imc with a 0.5 nA, 100 ms current pulse (n = 4). As shown in Fig 5.6 C, during the additional current injection, the Ipc neuron fired at a higher frequency. No long lasting suppression was found after the additional current injection terminated, rather a brief gap in spiking of approximate 35 ms duration caused by strong afterhyperpolarization.

In response to Imc stimulation, we observed different durations for the spike suppression in Ipc neurons. The duration of spike suppression is defined as, after

the stimulation at the Imc ended, the time that Ipc neuron takes to resume spiking in response to the current injection. Figure 5.7A shows an example of different durations of suppression in one Ipc neuron evoked by the same stimulation in Imc but with different current injections into the Ipc neuron. Spike

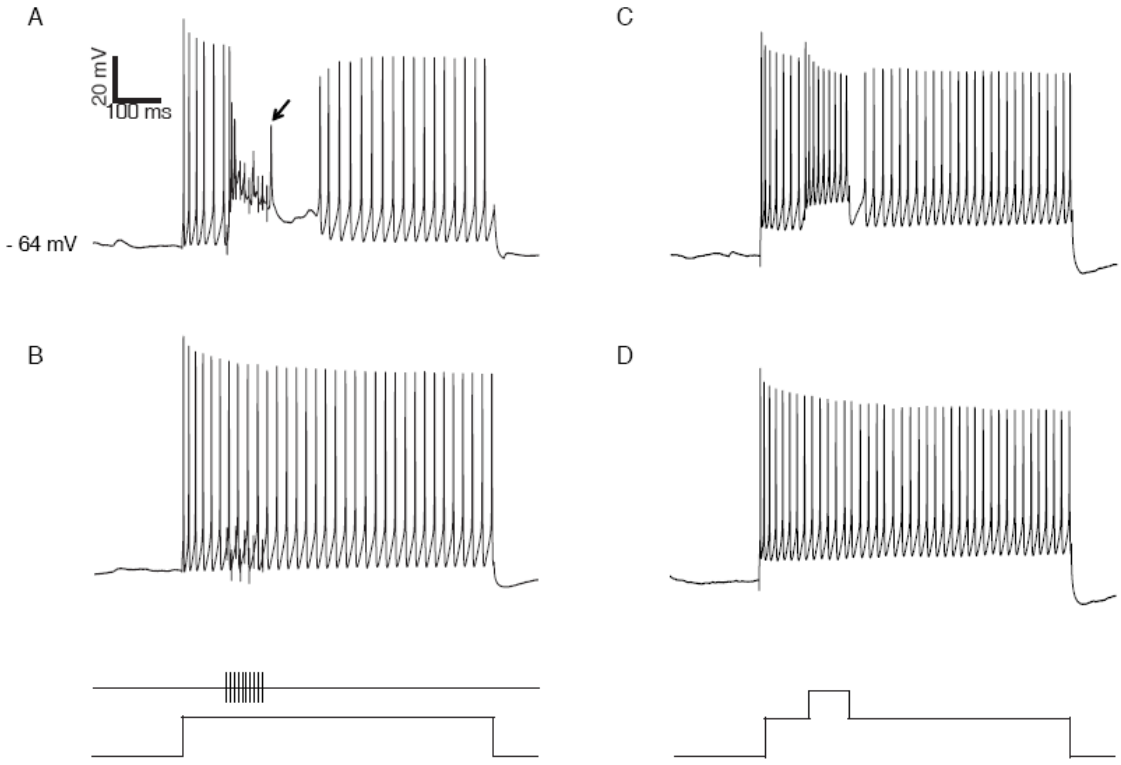

Figure 5.6 Imc stimulation suppressed firing of Ipc neuron. (A) A step current injection into Ipc while stimulating at Imc with a train of 10 pulses at 100 Hz. Stimulation at Imc suppressed the action potentials in Ipc neuron that were evoked by somatic current injection. (B) By bath applying 100 μM bicuculline to the slice, Imc-evoked suppression was blocked. (C) In response to a 100 ms pulse current which was applied to Ipc neuron soma in addition to a 500 ms step current, Ipc neuron fired at a higher frequency compared to (D) Only the 500 ms step current was applied.

suppression extended in duration as the amount of current injection increased. For 0.6 nA current, the duration of suppression outlasted the duration of current injection.

The duration of spike suppression was plotted against the firing rate of Ipc neurons in response to the current injection (Fig. 5.7 B). The population of tested Ipc neurons (n = 13) showed no dependency of the suppression duration to the Ipc firing rate. However, two individual neurons (Fig. 5.7B, solid line) showed opposite dependencies.

5.4.4 Model neuron

To evaluate the mechanism of Imc-evoked spike suppression in Ipc neurons, we built a two compartment model neuron and implemented the currents and synapses (Fig. 5.8A). The above observations suggest that a slow current, activated by Imc stimulation, mediates the long lasting spike suppression in Ipc neurons. We implemented the M-current into our model neuron as a possible candidate for this slow current. M-current is a slow potassium current activated by depolarization and found to be responsible for the adaptation of firing rate and the afterhyperpolarization (AHP) of cortical pyramidal cells (McCormick et al., 1993; Yamada et al., 1989). Simulation was carried out similarly to the protocol of experiments. Current was applied to the soma of the model neuron and during the current injection the GABAergic synapse was activated 10 times at 10 ms intervals. Figure 5.8B shows an example of the simulation results. The model

reproduces the long lasting suppression of spikes in the Ipc neuron after the synaptic stimulation. We further investigated the dependency of the duration of suppression to the conductance of the M-current. We found that increased M-current conductance led to longer suppression in model Ipc neurons (Fig 5.8 C).

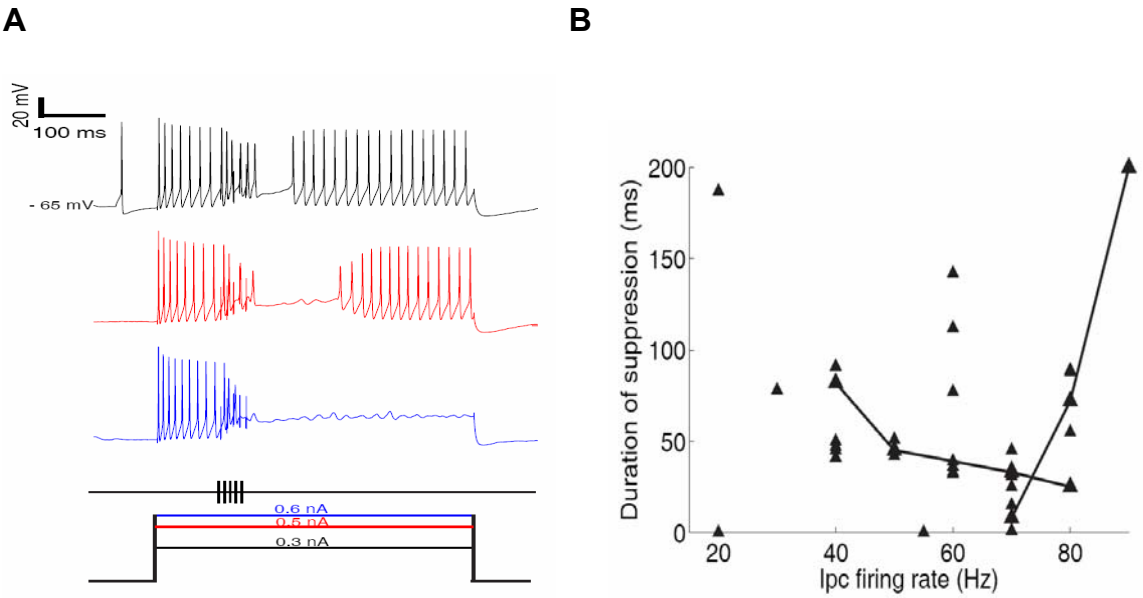

Figure 5.7 Different durations of Imc evoked spike suppression in Ipc neurons. (A) Step current injection into Ipc while stimulating at Imc with a train of 5 pulses at 100 Hz. Black trace, 0.3 nA current step; red trace, 0.5 nA; blue trace, 0.6 nA. (B) Duration of suppression against Ipc firing rate. Solid lines connect data points from one Ipc neurons. Here Ipc firing rate was calculated as 10 times the number of spikes in the first 100 ms of current injection, before Imc stimulation started. That is why the Ipc firing rates appear to be multiples of 10. If Ipc neuron did not recover to spike at all, as shown in (A) blue trace, the duration of suppression was not recorded in (B) .

This confirmed our assumption that a slow hyperpolarizing current, activated by Imc stimulation, was responsible for the long lasting spike suppression in Ipc neuron.

5.5 Discussion

In this study, we first show the excitatory actions of GABA onto Ipc neurons. The GABAergic synaptic currents from Imc to Ipc, with a reversal potential of approximately - 35 mV, can evoke EPSPs and action potentials in Ipc neurons. Bath application of GABA depolarizes Ipc neurons by an average of 20 mV. Using the method of gramicidin-perforated patch recording, we further demonstrated that our observation of excitatory actions of GABA is not an artifact of the whole-cell patch electrode. Moreover, recordings from P8-P10 chickens reveal that depolarizing GABAergic synaptic current to Ipc neurons may not be an indicator of immaturity but rather a part of their mature phenotype.

Our observation of spike suppression in Ipc neuron evoked by Imc stimulation suggests that the GABAergic input from Imc also has an inhibitory role on the activity of Ipc neurons. This spike suppression effect is in part attributed to a large reduction in input resistance caused by the opening of a GABAergic chloride conductance. This large reduction of input resistance increases the amount of current necessary to drive Ipc neurons to spiking threshold. Inactivation of voltage-dependent sodium current is possibly another factor

responsible for the spike suppression during the Imc stimulation in that GABA depolarizes Ipc neuron to a level that sodium channels stay inactivated.

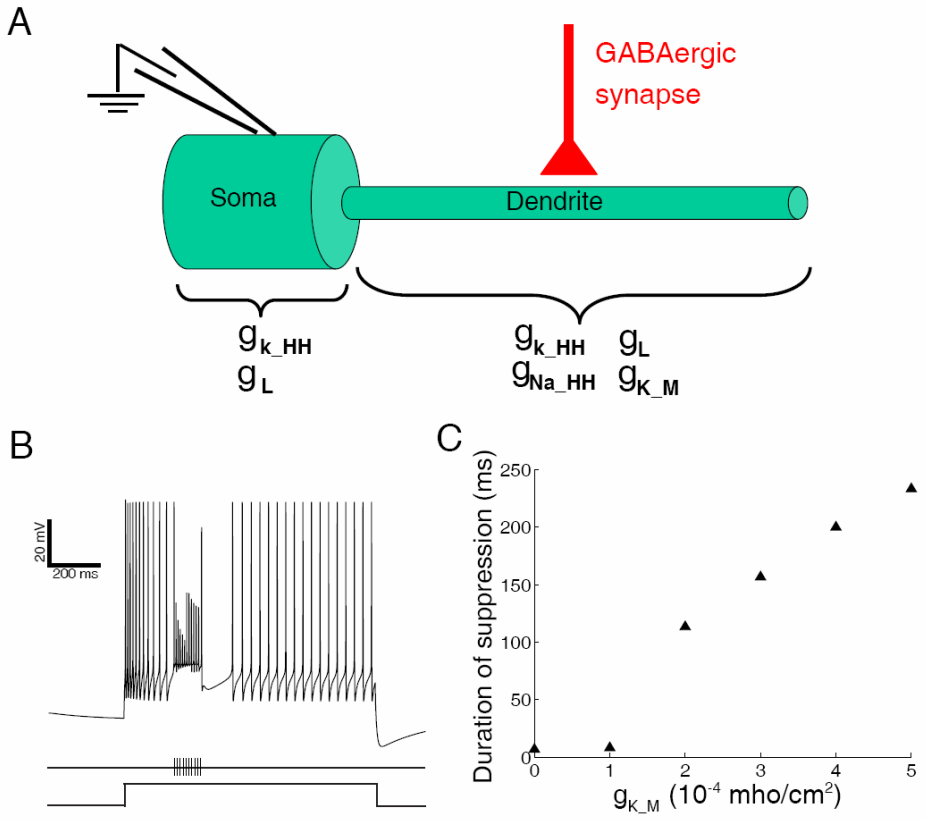

Figure 5.8 Model neuron and simulation results. (A) Schematic drawing of the two-compartment model of Ipc neuron. Ipc neuron was simulated as two cylinders: soma and dendrite. g_{K_HH}, conductance of Hodgin-Huxley potassium channel; g_L, leaky conductance of membrane; g_{Na_HH}, conductance of Hodgin-Huxley sodium channel; g_{K_M}, conductance of M-current ; GABAergic synapse was implemented onto the dendrite with a reversal potential of – 40 mV, which was above spiking threshold for the model neuron; external current was applied into soma; rest membrane potential was set at – 60 mV. (B) Computer simulation of 1000 ms somatic

current injection and activation of GABAergic synapse at 100 Hz. Simulation results qualitatively reproduced the observations from the experiments. (C) Dependency of suppression duration to the conductance of M-current.

Based on the experimental observations and computer simulations, we propose that GABA-mediated depolarization activates a slow hyperpolarizing current, which is responsible for the long lasting spike suppression in Ipc neurons. However, our results also show that merely depolarization in Ipc soma cannot trigger the spike suppression (Fig 5.6 C). This may provide an implication that only GABA-mediated depolarization in the Ipc dendrites can evoke this slow hyperpolarizing current and result in long lasting spike suppressions in Ipc neurons.

The important consideration here is that the functional advantage that may result from the depolarizing GABAergic synaptic currents with spike suppression. As has been suggested previously, one advantage of having a depolarizing GABAergic input is to allow the recruitment of additional conductances that are activated above resting potential (Hyson et al., 1995; Monsivais et al., 2000; Monsivais and Rubel 2001). For example, in the avian auditory brainstem, depolarizing GABAerigc synaptic currents has been reported to evoke a robust low voltage-activated (LVA) potassium conductance and more effectively inhibit

the firing of the postsynaptic neurons than hyperpolarizing synaptic currents (Monsivais et al., 2000; Monsivais and Rubel 2001; Howard and Rubel 2007).

In the isthmotectal feedback loop, Ipc and Imc both receive topographic inputs from the layer 10 neuron in tectum (Wang et al., 2004, 2006). Therefore, Ipc neurons receive the inputs from Imc within a short latency from the inputs from tectum. The regulatory GABAergic inputs may always coupled with excitatory inputs in Ipc neurons and therefore contribute to a more complex dynamics of isthmotectal feedback loop.

5.6 Reference

Alger BE and Nicoll RA (1979) GABA-mediated biphasic inhibitory responses in hippocampus. Nature 281:315-317.

Andersen P, Dingledine R, Gjerstad L, Langmoen IA, Laursen AM (1980) Two different responses of hippocampal pyramidal cells to application of gamma-amino butyric acid. J Physiol 305:279-296.

Bartos M., Vida I., Jonas P. (2007) Synaptic mechanisms of synchronized gamma oscillations in inhibitory interneuron networks. Nat Rev Neurosci 8:45-56.

Ben-Ari Y (2002) Excitatoy actions of GABA during developent: the nature of the nurture. Nat Rev Neurosci 3: 728-739.

Buzsáki G (1984) Feed-forward inhibition in the hippocampal formation. Prog Neurobiol 22:131-153.

Buzsáki G and Chrobak JJ (1995) Temporal structure in spatially organized neuronal ensembles: a role for interneuronal networks. Curr Opin Neurobiol 5:504-510.

Engel AK, Fries P, Singer W (2001) Dynamic predictions: oscillations and synchrony in top-down processing. Nat Rev Neurosci 2:704-716.

Gulledge AT and Stuart GJ (2003) Excitatory actions of GABA in the cortex. Neuron 37:299-309.

Howard MA and Rubel EW (2007) Mechanisms of shunting and accommodation in the avian nucleus magnocellularis. Society of Neuroscience annual meeting abstract: 67.22

Lu T, Trussel LO (2001) Mixed excitatory and inhibitory GABA-mediated transmission in chick cochlear nucleus. J Physiol 535.1: 125-131.

Markram H, Toledo-Rodriguez M, Wang Y, Gupta A, Silberberg G, Wu C (2004) Interneurons of the neocortical inhibitory system. Nat Rev Neurosci. 5:793-807.

McCormick DA, Wang Z and Huguenard J (1993) Neurotransmitter control of neocortical neuronal activity and excitability. Cerebral Cortex 3: 387-398.

Miles R, Toth K, Gulyas AI, Hajos N, Freund TF (1996) Differences between somatic and dendritic inhibition in the hippocampus. Neuron 16:815-823.

Monsivais P, Yang L, Rubel EW (2000) GABAergic Inhibition in Nucleus Magnocellularis: Implications for Binaural Processing in the Avian Brainstem. J Neurosci 20:2954-2963.

Monsivais P and Rubel EW (2001) Accommodation enhances depolarizing inhibition in central neurons. J Neurosci 21:7823-7830.

Pouille F and Scanziani M (2001) Enforcement of temporal fidelity in pyramidal cells by somatic feed-forward inhibition. Science 293:1159-1163.

Salinas E and Sejnowski TJ (2001) Correlated neuronal activity and the flow of neural information. Nat Rev Neurosci 22:539-550.

Staley KJ and Moday I (1992) Shunting of excitatory input to dentate gyrus granule cells by a depolarizing $GABA_A$ receptor-mediated postsynaptic conductance. J Neurophysiol 68: 197-212.

Staley KJ, Soldo BL, Proctor WR (1995) Ionic mechanisms of neuronal excitation by inhibitory $GABA_A$ receptors. Science 269: 977-981.

Taira T, Lamsa K, Kaila K (1997) Posttetanic excitation mediated by $GABA_A$ receptors in rat CA1 pyramidal neurons. J Neurophysiol 77:2213-2218.

Traub RD and Miles R (1991) Neuronal Networks of the Hippocampus, Cambridge Univ press.

Wang Y, Major DE, Karten HJ (2004) Morphology and connections of nucleus isthmi pars magnocellularis in chicks (*gallus gallus*). J Comp Neurol 469: 275-297.

Wang Y, Luksch H, Brecha NC, Karten HJ (2006) Columnar projections from the cholinergic nucleus isthmi to the optic tectum in chicks (*Gallus gallus*): A possible substrate for synchronizing tectal channels. J Comp Neurol 494:7-35.

Yamada WM, Koch C, Adams PR (1989) Multiple channels and calcium dynamics. In: Methods in Neuronal modeling, edited by C. Koch and I. Segev, MIT press: 97-134.

Chapter 6

OPEN QUESTIONS AND FUTURE DIRECTIONS

6.1 Long-lasting responses in the isthmotectal feedback loop

When retinal ganglion cell (RGC) afferents in tectal layer 2-4 were electrically stimulated, neurons in L10 responded with a long-lasting depolarization up to few hundred milliseconds with spikes and EPSPs riding on top it (Fig. 6.1a; Meyer 2008). Similar long-lasting responses were also found in Imc neurons in response to the RGC afferents stimulations (Fig. 6.1b). However, most responses to L2-4 stimulation found in Ipc neurons were single action potentials (Fig. 6.1c). This pattern of long-lasting response is very likely to be regulated by acetylcholine given that bath application of 2 μM mecamylamine hydrochloride known as a nicotinic acetylcholine receptor antagonist (Fig. 6.1a, inset), or surgical removal of the cholinergic Ipc nucleus could alter the long-lasting responses in L10 neurons to single action potential responses.

Long-lasting responses were also found in Ipc neurons (n = 2) when stimulation electrode was put in the Imc nucleus (Fig. 6.2). As mentioned in Chapter 4 when we electrically stimulated Imc to investigate synaptic responses in Ipc neurons, the stimulus electrode in the Imc nucleus could possibly stimulate: 1) L10 neuron axons, 2) Ipc neuron axons passing through the Imc nucleus, and 3) Imc neurons (Fig. 6.2a). Therefore, at the end of a recording session, we applied bicuculline to

verify that the synaptic inputs to the recorded Ipc neuron were indeed from the stimulated GABAergic Imc neurons. If the responses disappeared when 100 µM bicuculline was added to the bath thus (i) indicating that the responses were of

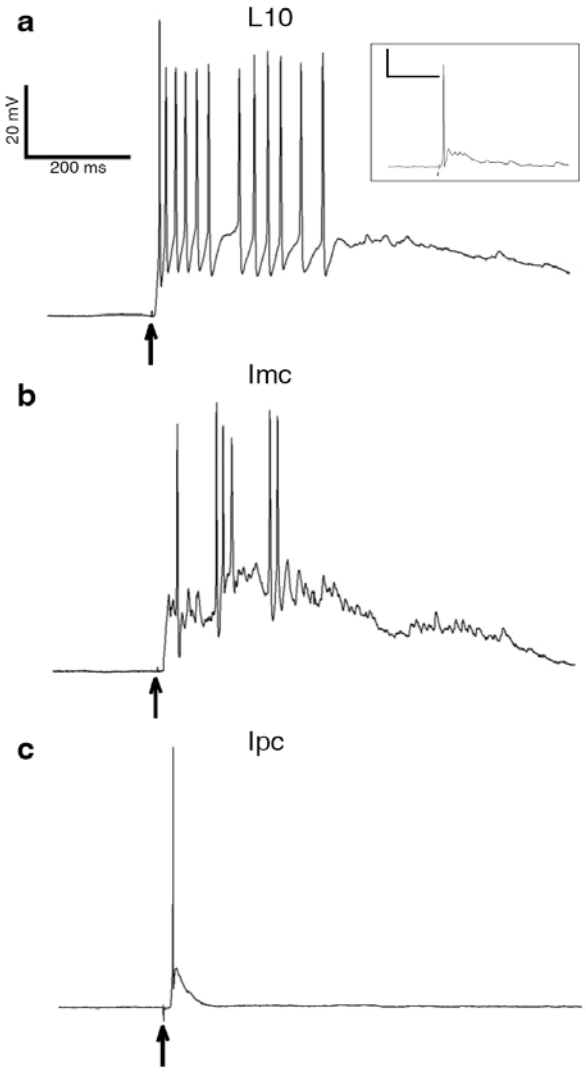

Figure 6.1 Responses to L2-4 RGC afferents stimulations. (a) response of a L10 neuron to tectal L2-L4 stimulation in control conditions and *inset* after addition of 2 µM Mecamylamine., Scale bar in the inset figure: 20 mV, 200 ms; (b) response of an Imc neuron to tectal L2-L4 stimulation; (c) response of an IpcL10 neuron to tectal L2-L4 stimulation. Modified after Meyer 2008.

synaptic origin (rather than antidromic Ipc or L10 axon stimulation) and (ii) confirming that GABA is the transmitter as had been suggested by anatomical studies (Wang et al., 2004). But here we showed an example when the responses in Ipc did NOT abolish in the application of bicuculline, which indicated Ipc and/or L10 axons were excited. The Ipc neuron responded to the single pulse stimulation with an action potential 4 ms after the stimulus (Fig. 6.2b); when two stimulating pulses were given, the Ipc neuron first responded to each pulse with an action potential, and approximately 100 ms after the second stimulation pulse the Ipc neuron had a long-lasting depolarization with fast spikes on top of it and this response lasted about 900 ms (Fig. 6.2c).

This pattern of long-lasting response was never found in Ipc neurons in the absence of bicuculline ($n > 50$), indicating the involvement of GABAergic Imc nucleus in suppressing the long-lasting responses in Ipc neurons. It is still unclear that why the latency of the long-lasting response in the Ipc neuron is almost 100 ms and why a minimum of two pulses stimulation is needed to trigger a long-lasting response (more than two stimulation pulses evoked similar responses as in Fig. 6.2c, data not shown). In addition, given the fact that long-lasting responses in L10 were influenced by the cholinergic Ipc nucleus, it is very likely that the long-lasting response in the isthmotectal feedback loop is a complex network property.

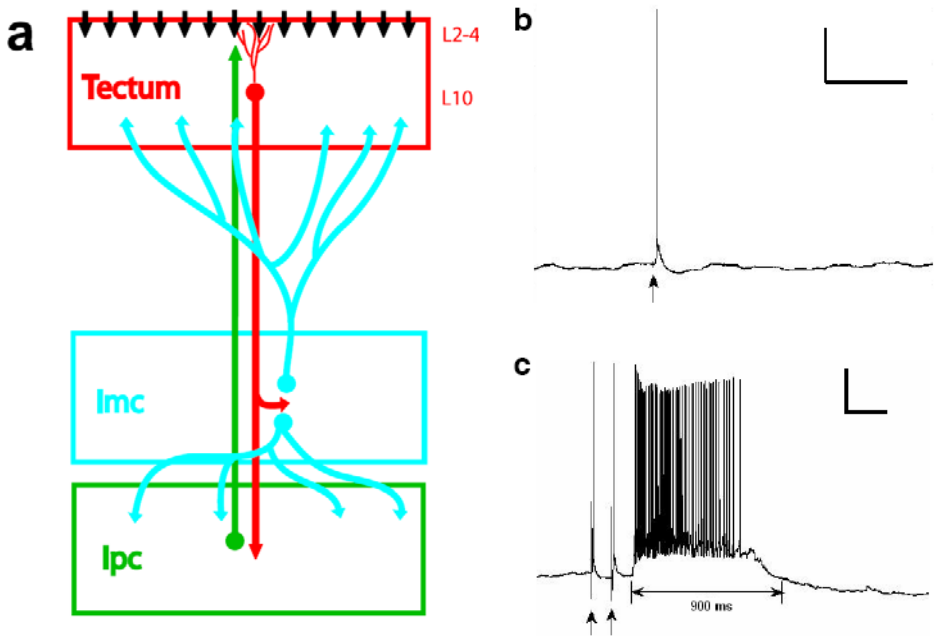

Figure 6.2 Long-lasting responses in Ipc neuron with application of bicuculline. (a) schematic drawing of isthmotectal feedback loop, note that in the Imc there are axons of L10 neurons and axons of Ipc neurons passing through; (b) in the presence of 100 µM bicuculline, an Ipc neuron responded with an action potential to one electrical pulse stimulation in the Imc; (c) same Ipc neuron responded to two pulses stimulation in the Imc with two action potential first and a long-lasting depolarization with fast spikes on top of it. Scale bar in (b) and (c): 20 mV, 200 ms.

6.2 Cholinergic modulation of retino-tectal transmission

Because of its exclusive projection to the tectum (Fig. 6.3b), the functional role of the Ipc activity can only be understood through its action onto tectal neurons. The tectal SGC wide-field neurons (Fig. 6.4a) receive visual inputs and provide the major projection from the tectum to the thalamic nucleus rotundus (Fig. 6.3b)

(Karten et al., 1997; Luksch et al., 1998). Local inactivation of the Ipc nucleus in vivo prevents visual responses in the spatially corresponding ascending RGC-SGC visual pathway to the nucleus rotundus (Fig. 6.3c) (Marin et al., 2007). This observation raises questions concerning the mechanisms of the cholinergic modulation to the RGC-SGC pathway.

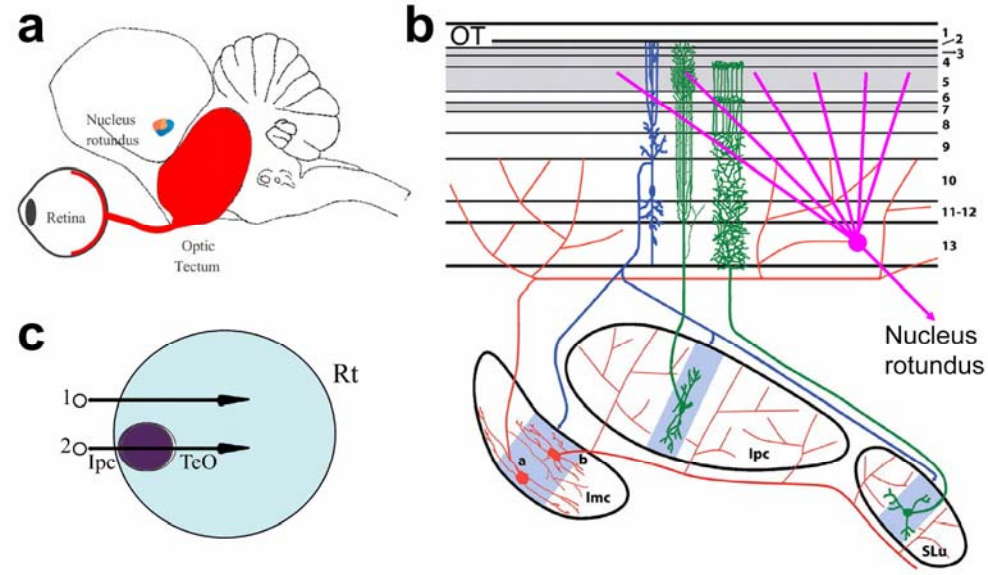

Figure 6.3 The modulation of retino-tecto-rotundal signal transmission by isthmic activity. (a) The tectal SGC wide-field neurons receive visual inputs and project to the thalamic nucleus rotundus. (b) Ipc axon terminals spatially overlap with tectal SGC neurons. A schematic of the SGC-I neuron is shown (pink). Modified after Wang et al., 2006. (c) Schematic representation of the visual stimuli, which were used to investigate the effect of Ipc activity on nucleus rotundus (Rt) visual responses. Modified after Marin et al., 2007.

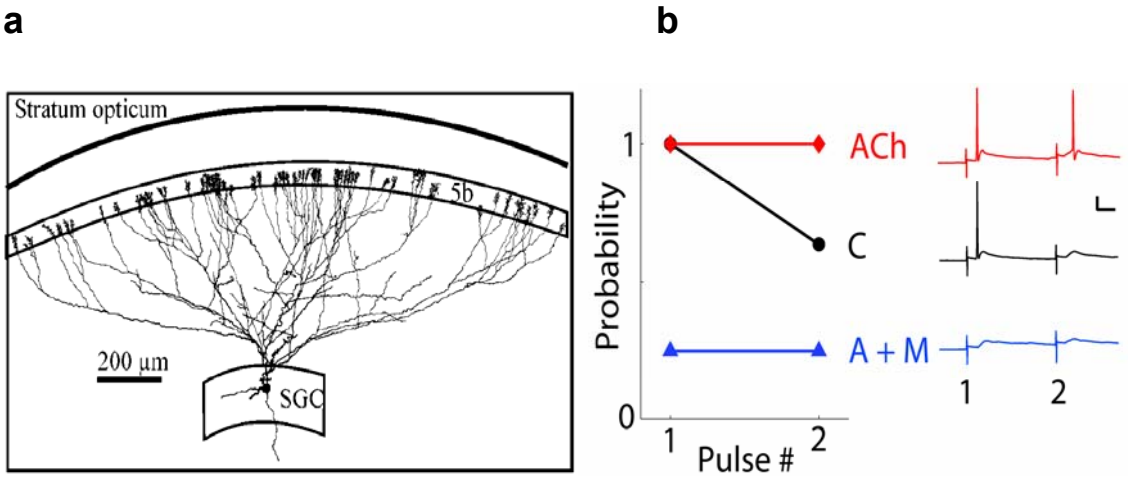

Figure 6.4 Cholinergic modulation of RGC-SGC pathway. (a) The characteristics of the SGC-I cell type include the large dendritic field and the arrangement of the dendritic endings in the retinorecipient layer 5, where they make synaptic contact with axon terminals from retinal ganglion cells (Karten et al., 1997; Khanbabaie et al., 2006). (b)SGC-I responses to RGC axon stimulation with paired pulses with interval of 100 ms. Waiting time between trials was 3 minutes. Response probabilities are shown for the three different conditions: (ACh) brief application of ACh puffs (100 µM Ach was manually puffed into the recording chamber through a syringe and pipette, thus the final Ach concentration in the recording chamber was much lower than 100 µM) during pulse stimulation (red, 8 trials), (C) control (black, 11 trials), and (A+M) 5 µM atropine plus 5 µM mecamylamine bath. Representative responses for each condition are shown to the right. RMP = - 60 mV for all three traces. Scale bars: 20 mV, 20 ms.

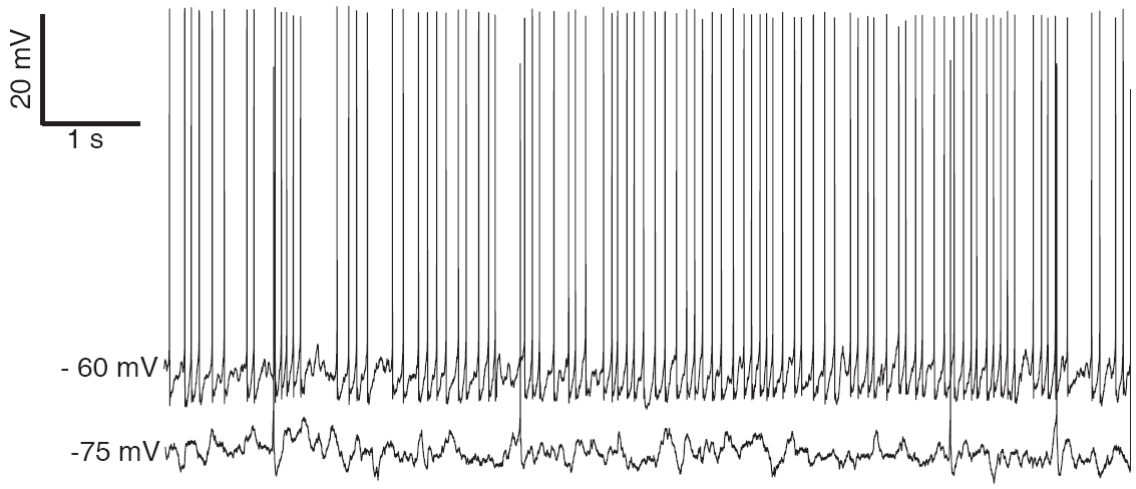

Figure 6.5 Spontaneous activity of SLu neuron. Top trace, spontaneous spikes in one SLu neuron. Bottom trace, spontaneous activity of same neuron under a constant hyperpolarizing current.

6.3 SLu nucleus

Besides Imc and Ipc, there is another isthmic structure accessible in the midbrain slice, nucleus semilunaris (SLu). The SLu is a cholinergic nucleus, reciprocally connected with tectum in a topographic way and receives GABAergic inputs from the Imc (Fig 6.3 b, Wang et al., 2006). SLu neurons have a high rate of spontaneous firing (Fig. 6.5 top trace), but not many spontaneous EPSPs were found even under the hyperpolarization (Fig. 6.5, bottom trace). This suggests that SLu is spontaneous active mostly because of its intrinsic excitability which implies that SLu could be a close analog of the parabigeminal nucleus (PBN) in the rat (Goddard et al., 2007). Thus, the function of PBN and SLu may be similar. Future work will determine the functional similarity of these structures.

6.4 Bipolar dendrites structure of lpc neurons

Bipolar dendrites structure has been found to be the key for detecting interaural time differences (ITD) at coincidence-detector neurons in the auditory brainstem where each neuron receives many narrow-band inputs from both ears and then compares the time of arrival of the inputs to locate the sound (Goldberg and Brown, 1969; Carr and Konishi, 1990; Overholt et al., 1992; Agmon-Snir et al., 1998). A portion of lpc neurons, mostly situate at the center of lpc nucleus (Fig 6.6; Wang et al, 2006), also have the bipolar dendritic structure. What's the functional role of this unique morphology? lpc only receives inputs from the tectum and lmc. Could it be possible that the axons from tectum only terminate on one end of the dendrites and inputs from lmc on the other? Interestingly, lpc neurons in turtle also exhibit bipolar dendrites structure (Kunzle and Schnyder, 1984; Sereno and Ulinski, 1987). Comparative studies on lpc neurons dendritic signal processing in chicks and in turtle will shed light into this mystery.

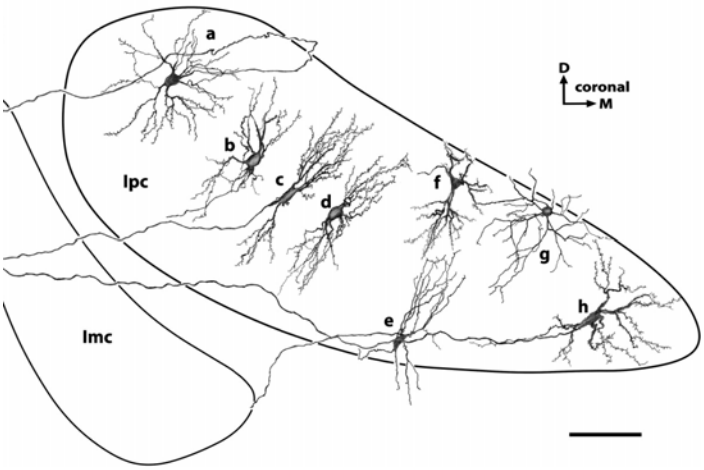

Figure 6.6 A montage drawing illustrates dendritic patterns of lpc neurons and their distribution within the nucleus. Scale bars = 100 μm. Modified after Wang et al., 2006.

6.5 Reference

Agmon-Snir H, Carr CE, Rinzel J (1998) The role of dendrites in auditory coincidence detection. Nature 393: 268-272.

Carr CE and Konishi M (1990) Acircuit for detection of interaural time differences in the brainstem of the barn owl. J Neurosci 10: 3227–3246.

Goddard CA, Knudsen EI, Huguenard JR (2007) Intrinsic excitability of cholinergic neurons in the rat parabigeminal nucleus. J Neurophysiol 98: 3486-3493.

Goldberg JM and Brown PB (1969) Response of binaural neurons of dog superior olivary complex to dichotic tonal stimuli: some physiological mechanisms of sound localization. J Neurophysiol 32: 613–636.

Karten HJ, Cox K, Mpodozis J (1997) Two distinct populations of tectal neurons have unique connections within the retinotectorotundal pathway of the pigeon (Columba livia). J Comp Neurol 387: 449-465.

Khanbabaie R, Mahani A, Wessel R (2007) Contextual interaction of GABAergic circuitry with dynamic synapses. J Neurophysiol 97: 2802-2811.

Kunzle H, Schnyder H (1984) The isthmus-tegmentum complex in the turtle and rat: a comparative analysis of its interconnections with the optic tectum. Exp Brain Res 56: 509-522.

Luksch H, Khanbabaie R, Wessel R (2004) Synaptic dynamics mediate sensitivity to motion independent of stimulus details. Nat Neurosci 7: 380-388.

Marin G, Salas C, Sentic E, Rojas X, Letelier JC, Mpodozis J (2007) A cholinergic gating mechanism controlled by competitive interactions in the optic tectum of the pigeon. J Neurosci 27: 8112-8121.

Meyer U (2008) The tectal-isthmic loop of the chicken (*Gallus gallus*) in a slice preparation: electrophysiology of its elements. PhD dissertation, RWTH Germany: 29-34.

Overholt EM, Rubel EW, Hyson RL (1992) A delay-line circuit for coding interaural time differences in the chick brain stem. J Neurosci 12: 1698–1708.

Sereno MI, Ulinski PS (1987) Caudal topographic nucleus isthmi and the rostral nontopographic nucleus isthmi in the turtle, *Pseudemys scripta*. J Comp Neurology 261: 319-346.

Wang Y, Major DE, Karten HJ (2004) Morphology and connections of nucleus isthmi pars magnocellularis in chicks (Gallus gallus). J Comp Neurol 469: 275-297.

Wang Y, Luksch H, Brecha NC, Karten HJ (2006) Columnar projections from the cholinergic nucleus isthmi to the optic tectum in chicks (*Gallus gallus*): A possible substrate for synchronizing tectal channels. J Comp Neurol 494:7-35.